

A STUDY OF ITG AND KBM TURBULENCE IN
LOW-MAGNETIC-SHEAR, INHERENTLY-THREE-DIMENSIONAL
MAGNETIC EQUILIBRIA

by

IAN J. MCKINNEY

A dissertation submitted in partial fulfillment of
the requirements for the degree of

DOCTOR OF PHILOSOPHY

(NUCLEAR ENGINEERING AND ENGINEERING PHYSICS)

at the

UNIVERSITY OF WISCONSIN-MADISON

2021

Date of final oral examination: 11/17/2021

The dissertation is approved by the following members of the Final Oral Committee:

Chris C. Hegna, Professor, Engineering Physics

Paul W. Terry, Professor, Physics

David T. Anderson, Professor, Electrical and Computer Engineering

Benedikt Geiger, Professor, Engineering Physics

Carl R. Sovinec, Professor, Engineering Physics

M.J. Pueschel, Scientist, Eindhoven University of Technology

Thank you, Ma and Pops.

Acknowledgements

I owe a great debt of gratitude to Chris Hegna, David Anderson, Paul Terry, and M.J. Pueschel. To Chris, thank you for taking me on as a student, for being a good mentor, for answering all of my questions when I would randomly drop by your office, and for being patient with me while I derived the five-field model when you probably could have done it in a week. To Dave, thank you for hiring me as a research assistant in August of 2016, even after I showed up late to your class half of the time. To Paul, thank you for taking the time to give a goofy undergraduate a project in plasma physics in the Fall of 2014 and for your continued guidance and mentorship ever since. To M.J., last but certainly not least, thank you for the numerous weekly, and sometimes more often than that, meetings that helped me stay focused and accountable for steady progress in my research. Thank you for being a fountain of GENE knowledge to draw upon whenever something was not working properly or a simulation result was confounding. Without you, I would likely still be one or two years out from graduation.

I would also like to thank my friends. To Kyle, Amanda, Kat, and Peter, our weekly game nights, especially during lockdown, were a major highlight

of my weeks over the years. Thank you for the Magic: The Gathering tournaments, the numerous hours of DOTA, and for being there for me. To Garrett, thank you for sharing your enthusiasm for board games, for spouting as much gibberish as I do, and for grabbing dinner whenever we both had a free night. I'd also like to say thank you to the Cascave: Justin, Adrian, Ben, Garth, Jason, and Zach (go Gators) for putting up with my fist bumps, for putting up with my poor Smash Bros. skills, for Cascave Group Lunch (CGL), and for making my time in Madison generally more pleasant and meaningful. To the HSX crew, especially Fernando, Paul, Wayne (and Amanda), Dimitri, Alex (and Nicole), double T, and Jarod (and Trista), thank you all for the wonderful Library nights, the psychologist sessions on the couch, the Kwiktrip runs, and for being hands down the best cohort of graduate students in plasma at UW-Madison. You all made coming into work easy and something I legitimately looked forward to during my tenure at HSX. I'd also like to thank Daham and Erin for their wisdom and direction over the years, even if sometimes I refused to listen. Finally, the biggest thank yous go to my goons: Cheech, Ranch (sorry Reed), Mr. House, and Bruce Springstein. Thank you guys for being some of my closest friends and for always being there for me whether it's for a good time or for a deep conversation.

Lastly, I would like to thank my family. There are too many of you to list here, but you know who you are. However, I would like to explicitly thank my mom and dad. Thank you two for everything that you have done for me.

While growing up was not easy at times, it made me the man that I am today, and I would not change anything.

Abstract

Ion-temperature-gradient-driven (ITG) and kinetic-ballooning-mode (KBM) turbulence is studied using the gyrokinetic turbulence code GENE in four magnetic equilibria: the quasi-helically symmetric HSX, the quasi-axisymmetric NCSX, Heliotron-J, and a small- \hat{s} tokamak. The ITG portion of this dissertation focuses on a comparison of HSX and NCSX to determine the relationship between linear ITG behavior and nonlinear heat fluxes. In normalized units, HSX exhibits higher growth rates and quasilinear estimates than NCSX, while heat fluxes in gyro-Bohm units are lower in HSX. The ITG results also show that HSX has a larger number of subdominant modes than NCSX and that eigenmodes are more spatially extended in HSX. The ITG turbulence also consists of many more concurrently excited modes in HSX compared to NCSX, as highlighted by the broadband nonlinear frequency spectra in HSX versus NCSX. The KBM portion of this work focuses on the low-magnetic-shear configurations HSX, Heliotron-J, and a small- \hat{s} tokamak since all three magnetic equilibria exhibit a small critical $\beta(k_y = 0.1) \approx 0.2\%$ at which KBM becomes the dominant instability, dubbed $\beta_{\text{crit}}^{\text{KBM}}$. Additional KBM studies highlight both how $\beta_{\text{crit}}^{\text{KBM}}$ scales with average magnetic shear and ion temperature gradient in HSX and that nonlinear saturation of finite- β turbulence in HSX

requires that the minimum k_y of the system be stable to KBMs. Subsequent analyses highlight the importance of KBM nonlinearly, both in terms of the electrostatic heat flux and the nonlinear energy transfer. A fluid model which will be used to study ITG-KBM turbulence saturation in configurations of interest is also introduced, and some preliminary benchmarks of said reduced model are presented too.

TABLE OF CONTENTS

	Page
Abstract	v
Table of Contents	vii
LIST OF FIGURES	x
1 Introduction to magnetic confinement	1
1.1 Plasma and its application to fusion energy	2
1.2 Plasma particle drifts in magnetic fields	4
1.3 Neoclassical and turbulent transport in stellarators	11
1.4 HSX, NCSX, and Heliotron-J	14
1.5 Thesis Outline	24
2 Drift-wave turbulent transport in quasi-symmetric stellarators	28
2.1 Drift-wave linear instability mechanism	29
2.2 The ion-temperature-gradient (ITG) mode	32
2.3 The kinetic ballooning mode (KBM)	35
2.4 Turbulent transport	38
3 Gyrokinetics	48
3.1 The Vlasov equation	49
3.2 The GENE Code	52
3.2.1 Flux-tube simulation domain	53
4 Electrostatic ITG turbulence in stellarators	59
4.1 Adiabatic-electron turbulence	59
4.1.1 Linear eigenmodes	60
4.1.2 Subdominant mode landscape	63

	Page
4.1.3 Eigenmode structure	66
4.1.4 Quasilinear transport modeling	68
4.1.5 Nonlinear dynamics	70
4.1.6 Heat flux spectra	72
4.1.7 Cross-phases	72
4.1.8 Nonlinear frequency spectra	76
4.2 Kinetic-electron simulations	78
4.2.1 Linear eigenmodes	79
4.2.2 Nonlinear dynamics	81
4.3 Conclusions of this chapter	89
5 Electromagnetic turbulence in stellarators	95
5.1 Linear KBM physics	97
5.1.1 KBMs in HSX	97
5.1.2 Destabilization of multiple branches of KBMs	101
5.1.3 Dependence of KBM on magnetic shear \hat{s}	105
5.1.4 Dependence of the KBM threshold on ω_{Ti}	108
5.1.5 KBMs in Heliotron-J and a small- \hat{s} tokamak	109
5.2 KBM turbulence in HSX	113
5.3 The five-field model	122
5.3.1 Ion continuity equation	127
5.3.2 Ion parallel momentum	130
5.3.3 Ion energy equation	131
5.3.4 Electron continuity equation	132
5.3.5 Electron parallel momentum equation	133
5.3.6 Closing the system	133
5.3.7 Normalized variables	134
5.3.8 Summary of the five-field model	139
5.4 Evaluating the five-field model	140
5.5 Conclusions of this chapter	142
6 Conclusions, summary, and future research	149
6.1 Summary	150

Appendix

	Page
6.1.1 Novel comparison of ITG turbulence between two quasi-symmetric stellarators	150
6.1.2 Novel ITG-KBM turbulence results in the quasi-helically symmetric stellarator HSX	152
6.2 Future work	154
6.2.1 Research items	154

LIST OF FIGURES

Figure	Page
1.1 A toroidal magnetic field configuration known as the tokamak, where electric current is run through coils (shown in red) to produce a strong magnetic field (example magnetic field lines, which together comprise a magnetic flux surface, shown in blue) to confine hot plasma (shown in yellow).	10
1.2 Electron diffusion coefficients as a function of minor radius for the HSX quasi-symmetric stellarator. There are four curves: “Mirror Exp.”, the experimental data for the mirror configuration achievable on HSX, “QHS Exp.”, the experimental data for the quasi-helically symmetric configuration achievable on HSX, “Mirror Neo.”, the numerically-calculated neoclassical transport predictions for the mirror configuration, and “QHS Neo.”, the numerically-calculated neoclassical transport predictions for the quasi-helically symmetric configuration. One of the primary conclusions to be drawn from these data is the significant difference between “QHS Neo.” and “QHS Exp.”, especially in the edge, an indication that anomalous (or turbulent) transport, and not neoclassical transport, is the dominant transport mechanism. [18]	13
1.3 $ \mathbf{B} $ on the outermost flux surface of the quasi-helically symmetric HSX magnetic equilibrium. Note that the lines of relatively constant magnetic field strength form a helix. Red (blue) indicates regions of high (low) magnetic field strength. The axes correspond to spatial Cartesian coordinates.	16

Figure	Page
1.4 $ \mathbf{B} $ on the outermost flux surface of the quasi-axisymmetric NCSX magnetic equilibrium. Note that the high-field side of the flux surface is always the inboard side, like in a tokamak. Red (blue) indicates regions of high (low) magnetic field strength. The axes correspond to spatial Cartesian coordinates.	17
1.5 $ \mathbf{B} $ on the outermost flux surface for the non-quasi-symmetric Heliotron-J magnetic equilibrium. Note that there is no line of constant magnetic field strength that can be drawn over one full toroidal transit. Heliotron-J does not exhibit any form of quasi-symmetry. Red (blue) indicates regions of high (low) magnetic field strength. The axes correspond to spatial Cartesian coordinates.	18
1.6 The Boozer spectrum for the HSX equilibrium. Only four magnetic Fourier modes are included as subsequent modes lie almost directly on top of either the $(4, 2)$ or $(4, 0)$ mode. The fact that the magnitude of the $(4, 1)$ mode is large relative to the non-symmetric components of the Boozer spectrum highlights the quasi-helical symmetry of HSX. The $(0, 0)$ component, which is equal to 1, is omitted for readability.	20
1.7 The Boozer spectrum for the baseline NCSX equilibrium. Only the six magnetic Fourier modes with the largest amplitude are included. The large magnitude of the $(0, 1)$ mode relative to the non-axisymmetric modes highlights the quasi-axisymmetry of NCSX. The $(0, 0)$ component, again equal to 1, is excluded for readability.	21
1.8 The Boozer spectrum for Heliotron-J, where the seven largest-magnitude modes are included. The $(0, 0)$ component, again equal to 1, is omitted for readability. Note that the $(0, 1)$, $(4, 0)$, $(8, 2)$ and $(4, 1)$ modes have comparable magnitude, a confirmation that Heliotron-J is not quasi-symmetric.	23

Appendix	Page
Figure	
2.1 The standard drift wave scenario for toroidal magnetic geometries. Arrows on the bottom of the figure indicate the direction of increasing pressure and $ \mathbf{B} $ on the x -axis. Arrows on the left of the figure indicate the direction of the curvature drift of each particle species on the y -axis. The background magnetic field is directed out of the page in the positive z -direction. The blue sinusoidal variation is a fluctuation of the plasma pressure p with finite k_y . This figure is taken from Grulke and Klinger, (2002) [15].	31
3.1 This figure highlights the gyroaveraging done in gyrokinetic codes such as GENE code where, rather than resolving the gyromotion of charged particles in strong magnetic fields, one can average over the gyrophase and simulate charged rings. This is valid because the characteristic time-scales of plasma turbulence are much slower than the time-scale associated with gyromotion. Source: Noguchi, 2016.	54
3.2 The $s_0 \approx 0.5$ flux surfaces of NCSX (left) and HSX (right). The black lines indicate the $\alpha = \theta - \iota\xi = 0$ flux-tube domains of each configuration, where θ and ξ are the poloidal and toroidal angle in Boozer coordinates, respectively. Figure courtesy of Pavlos Xanthopoulos.	56
4.1 The dominant linear growth rate γ (top) and real frequency ω (bottom) as a function of normalized binormal wavenumber k_y for the NCSX (black triangles) and HSX (blue squares) configurations for the $\alpha = 0$ flux tubes.	62
4.2 A set of 123 and 47 linear eigenmodes in HSX (blue hollow diamonds) and NCSX (black filled diamonds), respectively, at binormal wavenumber $k_y\rho_s = 0.3$ for computations with adiabatic electrons, as determined by GENE's iterative eigenvalue solver. Note the substantial number of subdominant modes in HSX relative to the few in NCSX.	64

Appendix	Page
Figure	
4.3 Eigenmode amplitude as a function of parallel coordinate along the field line for binormal wavenumber $k_y \rho_s = 0.2$ for the baseline NCSX configuration (black) and the HSX geometry (blue) for computations with adiabatic electrons. Note the extended nature of the HSX eigenmode relative to NCSX.	67
4.4 Normalized heat flux time traces for HSX (blue solid line) and NCSX (black dotted line) with adiabatic electrons. The heat flux is approximately 17 and 6 in gyro-Bohm units for NCSX and HSX, respectively, averaged over the quasi-stationary state.	71
4.5 The heat flux spectra for HSX (blue squares) and NCSX (black triangles) from nonlinear simulations with adiabatic electrons. . .	73
4.6 The probability distribution function for the nonlinear cross-phase α between Φ and T_i^{tot} for the NCSX (top) and HSX (bottom) configurations from simulations with adiabatic electrons. Cross-phases of the dominant linear eigenmode (black dashed curve) are included for comparison.	75
4.7 The nonlinear frequency spectra for the NCSX (top) and HSX (bottom) configurations from simulations with adiabatic electrons. The color scale, which denotes Fourier mode amplitude, has arbitrary units and is linear and normalized at each k_y separately. It is also important to note that there is an amplitude weighting at each separate k_y so that modes with larger amplitude contribute more significantly.	77
4.8 Linear growth rate γ (top) and real frequency ω (bottom) as functions of normalized binormal wavenumber k_y for HSX (blue squares) and NCSX (black triangles) from simulations with kinetic electrons. Note that, again, linear ITG growth rates for HSX in the transport-relevant k_y regime are higher than NCSX, by as much as a factor of two or three, depending on the k_y in question. . . .	80

Appendix	Page
Figure	
4.9 Heat flux time traces for the HSX (blue solid line) and NCSX (black dashed line) configurations from simulations with kinetic electrons. The electrostatic ion heat flux for HSX remains lower than NCSX even for kinetic electrons.	83
4.10 Heat flux spectra for HSX (blue squares) and NCSX (black triangles) with kinetic electrons. Two important things to note: the HSX spectrum peaks at lower k_y , a finding that is consistent with adiabatic-electron results and a downshift in peaks is observed relative to the linear growth rate spectra for HSX and NCSX, another finding that is consistent with the adiabatic-electron results.	84
4.11 The probability distribution function for the nonlinear cross-phase between Φ and T_i^{tot} for simulations of NCSX (top) and HSX (bottom) with kinetic electrons. Linear cross-phases of the dominant eigenmode are overlaid (black dashed curve) for comparison. The nonlinear cross-phase color scale is linear. It is important to note the prominent low- k_y feature present in both configurations, a result which suggests that the transport mechanism is more efficient relative to the adiabatic-electron case. This is consistent with the increase in fluxes.	85
4.12 Nonlinear frequency spectra of NCSX (top) and HSX (bottom) from simulations with kinetic electrons. The color scale is linear and normalized at each k_y separately, and its units are arbitrary. Note the broadband nature of the turbulence in the HSX case relative to the narrow spectrum for NCSX.	88
5.1 γ and ω as functions of k_y with $\beta = 0.48\%$, roughly half of the MHD ballooning threshold $\beta \approx 1.1\%$. Note the discontinuity in real frequency near $k_y \rho_s \approx 0.1$, an indication of a change in mode branch from ITG to KBM. Also note that at high $k_y \rho_s > 1.8$, the growth rate begins to increase again, but that there is no discontinuity in the real frequency.	99

Appendix	Page
Figure	
5.2 γ and ω as functions of β for $k_y \rho_s = 0.6$. Observe the discontinuity in real frequency near $\beta_{\text{crit}}^{\text{KBM}} \approx 2.3\%$, an indication of a change in mode branch from ITG to KBM.	100
5.3 γ and ω as functions of β for $k_y = 0.1$. Observe the low value of $\beta_{\text{crit}}^{\text{KBM}}$ ($\approx 0.07\%$), compared with the ideal ballooning threshold of $\beta_{\text{crit}}^{\text{MHD}} \approx 1.1\%$ in HSX. This aspect of the KBM dynamics in HSX makes it difficult to achieve saturation in nonlinear simulations of HSX above $\beta_{\text{crit}}^{\text{KBM}}$	102
5.4 $\beta_{\text{crit}}^{\text{KBM}}$ as a function of k_y for both the HSX (blue squares) and NCSX (black triangles) configurations. $\beta_{\text{crit}}^{\text{MHD}}$ is included for comparison, as calculated by an MHD ballooning code [14]. For HSX, in the range of k_y between 0.1 and 0.2, KBMs are destabilized at very low values of β	103
5.5 The subdominant spectrum (a) for HSX with $k_y = 0.2$ and $\beta = 0.5\%$ consisting of KBMs (diamonds) and ITG modes (triangles), and the associated electrostatic potential Φ eigenmode structures (denoted by the same color as the associated diamond) (b) for various KBMs. Note the two distinct families of KBMs: one with Φ symmetric about $\theta_p = 0$ and one with off-center peaking. For each mode of the latter family, there is a sibling mode that is mirrored across the $\theta_p = 0$ axis with identical γ and ω ; hence they are indistinguishable in (a). Also note that some of the centered KBMs (blue, green) have tearing parity, i.e. are odd functions of ballooning angle.	106
5.6 $\beta_{\text{crit}}^{\text{KBM}}$ at $k_y \rho_s = 0.1$ as a function of the average magnetic shear \hat{s} along the flux tube. The dashed vertical red line indicates the value of the nominal magnetic shear of HSX. Note the increase in $\beta_{\text{crit}}^{\text{KBM}}$ as $ \hat{s} $ increases, regardless of sign.	107

Appendix

Figure

Page

- 5.7 $\beta_{\text{crit}}^{\text{KBM}}$ as a function of k_y for the case where the ion temperature gradient is removed but the sum of the gradients $\omega_{Ti} + \omega_{Te} + 2\omega_n$ is kept constant. Unlike the data presented in Fig. 5.4, $\beta_{\text{crit}}^{\text{KBM}}$ does not dip to values much smaller than the MHD threshold at low k_y 110
- 5.8 Heliotron-J, another low-magnetic-shear, three-dimensional magnetic equilibrium, also displays HSX-like KBM behavior at low k_y , as shown here in the plot of γ vs. β . Note that at this k_y , the $\beta_{\text{crit}}^{\text{KBM}}$ is roughly 0.14%. 111
- 5.9 The $\beta_{\text{crit}}^{\text{KBM}}$ spectrum (a) and the subdominant-mode spectrum at $k_y = 0.2$ and $\beta = 0.8\%$ (b) for an $\hat{s} = -0.052$ circular tokamak s - α geometry in (a), there are two curves: one for the case when $\alpha_{\text{MHD}} = 0$ (red squares), where the equilibrium and dynamical β are not self-consistent; and a second for the case when α_{MHD} is such that both the equilibrium and GENE β are the same (black triangles). (b) The two distinct subdominant ITG (crosses) and KBM (diamonds) clouds are also present in the circular tokamak case. However, there is only a single KBM branch in this case versus the two that were present in HSX. 112
- 5.10 Time traces of electrostatic ion heat flux (black), electrostatic particle flux (red), and electromagnetic electron heat flux in gyro-Bohm units for HSX with $k_y^{\text{min}} = 0.025$ and $\beta = 0.48\%$. Note that there is significant stabilization relative to the nearly-electrostatic case in Fig. 4.9, where $Q_i^{\text{es}} \approx 23$ for HSX. The small electromagnetic heat flux is due to the small electron temperature gradient, implying that electron flutter transport is small. 115
- 5.11 Heat flux spectra associated with the $\beta = 0.48\%$ nonlinear simulation (black) and an analogous $\beta = 0.24\%$ nonlinear simulation (blue). The shaded region corresponds to the k_y -range in which KBM is the dominant linear instability. Note that the overwhelming majority of the heat flux is due to fluctuations in the KBM-dominant k_y regime, even for $\beta = 0.24\% \approx \beta_{\text{crit}}^{\text{KBM}}(k_y = 0.1)$ 116

Appendix	Page
Figure	
5.12 The nonlinear Φ spectrum for HSX with $k_y^{\min} = 0.025$ and $\beta = 0.48\%$. The spectrum is truncated at $k_y \rho_s = 0.5$ since $ \Phi ^2$ amplitudes are negligible above this threshold. Note that the zonal component is much weaker than the integrated non-zonal amplitudes, and also weaker than the peak amplitude.	118
5.13 The nonlinear frequency spectrum for HSX with $k_y^{\min} = 0.025$ and $\beta = 0.48\%$. The color scale has arbitrary units and is linear and normalized at each k_y separately. Linear frequencies of the most unstable (gold crosses), maximal-frequency (green triangles), minimal-frequency (red squares), and most unstable outboard-centered (black-white dashed diamonds) KBMs are also included for comparison. The dominant linear outboard-centered KBM frequencies match the nonlinear signal very well.	119
5.14 Nonlinear energy transfer functions indicate locations which give (blue) and receive (red) energy to and from $(k_x = 0.06, k_y = 0.1)$, denoted by the tip of the black arrow. There is significant zonal transfer from $(k_x = 0.06, k_y = 0.1)$ to the blue clouds near $k'_y = 0$ and $k'_y = 0.1$. Significant non-zonal energy transfer is also observed at $k'_y = -0.025$ and $k'_y = 0.125$	121
5.15 The sum (over $k_x \neq 0$) of the root-mean-squares (over coupled k'_x) of time-averaged nonlinear energy transfer functions for zonal ($k_y = 0$) modes as a function of k'_y . The data is normalized to the value of the point at $k'_y = 0.125$ so that the maximal value is one for ease of comparison. Note that the peak is in the KBM-dominated k'_y -range, evidence that KBMs play an important role in zonal dynamics.	123

Appendix	
Figure	Page
5.16	The sum (over $k_x \neq 0$) of the root-mean-squares (over coupled k'_x, k'_y) of time-averaged nonlinear energy transfer functions, which are normalized by the value of the same quantity at $k_y = 0.1$ for ease of comparison. The primary conclusion to be derived from this figure is that KBMs likely play an equal or greater role than the zonal modes in nonlinear energy transfer. Additional analysis of specific triplet interactions is necessary to tease out the precise ratio of the respective contributions of KBMs and zonal modes. 124
5.17	Normalized ion heat flux Q_i^{es} (black diamonds) and particle flux Γ^{es} (red squares) as a function of β . Observe the significant reduction of transport for $\beta \gtrsim 0.2\%$ relative to $\beta \approx 0.05\%$ until β approaches the $\beta_{\text{crit}}^{\text{KBM}} \approx 0.6\%$ threshold for $k_y = 0.025$. Above $\beta = 0.6\%$, simulations no longer achieve a saturated state. A vertical dashed black line indicates $\beta_{\text{crit}}^{\text{KBM}} = 0.6\%$ at $k_y = 0.025$ and a vertical dotted black line indicates the $\beta_{\text{crit}}^{\text{KBM}} = 0.18\%$ at $k_y = 0.1$. The electron electromagnetic heat flux is negligible (normalized $Q_e^{\text{em}} \approx -0.2$ for $\beta = 0.48\%$) and therefore not included. 125
5.18	A comparison of subdominant modes corresponding to the ITG branch for CBC parameters. Three-field model modes are denoted by black diamonds while five-field model (with $\beta \rightarrow 0$) modes are denoted by red triangles. The two models coincide well, with some differences due to grid-scale modes, but, overall, this is evidence that the five-field model is behaving correctly when β is small. . . 141

Chapter 1

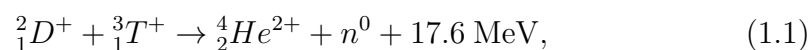
Introduction to magnetic confinement

The purpose of this chapter is twofold: first, this chapter (along with Chapters 2 and 3) provides background information which is necessary to understand the plasma turbulence results presented in Chapters 4 and 5. Second, this chapter motivates the study of plasma turbulence within the context of magnetic confinement fusion in a systematic way. These two chapter objectives are accomplished by introducing the notions of plasma and fusion energy before discussing how fusion-relevant plasma can be confined on Earth. Next, fundamental physics related to plasma particle drifts will be introduced and followed by the role that plasma turbulence plays in plasma confinement degradation within the context of neoclassical transport. Finally, four magnetic field configurations, the primary subjects of the present work, will be discussed: the Helically Symmetric eXperiment (HSX), the National Compact Stellarator eXperiment (NCSX), Heliotron-J (H-J), and a small- \hat{s} tokamak.

1.1 Plasma and its application to fusion energy

Plasma is a collection of free positively and negatively charged particles that exhibit collective electromagnetic effects. Everyday examples of plasma include lightning, neon signs, fluorescent lights, auroras in the night sky, welding arcs, and the sun. Plasma has a number of applications, one of which is fusion energy. Fusion is the process of combining two or more atomic nuclei, ideally in an exothermic nuclear reaction, to produce energy that is equal to the difference in the binding energy of the reactants and the products. Fusion is appealing because the fuel is relatively abundant on Earth and the materials involved exhibit radioactive half-lives on the order of at most tens of years rather than the many millions of years for fission energy. This process takes place in the sun, where hot plasma is confined by strong gravitational forces. Here on Earth, more clever methods must be employed to confine fusion-relevant plasmas, as requisite temperatures ($T_{\text{plasma}} \approx 10,000,000 \text{ }^\circ\text{C}$) are so high that containment mechanisms used for solids, liquids, and gases are inadequate. The goal underlying fusion energy is to economically confine a sufficiently dense plasma for a sufficiently long period of time at a sufficiently high temperature to produce more energy from fusion reactions and the resulting steam cycle than is required to operate the reactor. In fusion-energy-relevant applications, a plasma generally consists of positively charged isotopes of hydrogen, such as Deuterium (one proton and one neutron) and Tritium (one proton and two neutrons), and electrons with sufficient energy

such that they are not recaptured by the ions, although numerous plasma experiments are conducted using other gases as a means of exploring interesting plasma physics. A fusion reaction with Deuterium (D) and Tritium (T) as reactants is shown below in Eq. 1.1,



where He and n are Helium and a neutron, respectively, and where MeV denotes a unit of energy known as the Megaelectron-volt ($10^6 eV$), where an eV corresponds to the amount of kinetic energy gained by a single electron passing through a one volt electric potential difference.

It is not feasible to confine hot plasma with conventional methods used to confine solids, liquids, or gases. Fortunately, strong magnetic fields (approximately 20,000 times stronger than the magnetic field of Earth) can be used to confine fusion-energy-relevant plasmas. It is because of the natural helical orbits of charged particles in the presence of a strong homogeneous magnetic field that confinement is possible, where the gyration frequency Ω_g of the helical trajectory can be shown to be $\Omega_g = |q|B/m$, where q , B , and m are the charge of the particle, the magnetic field strength, and the mass of the particle, respectively. This is due to the Lorentz force shown in Eq. 1.2:

$$\mathbf{F} = q(\mathbf{E} + \mathbf{v} \times \mathbf{B}), \quad (1.2)$$

where \mathbf{E} and \mathbf{v} are the electric field and particle velocity, respectively. Since charged particles would be lost to parallel streaming in finite cylindrically-shaped magnetic field structures, one must instead construct magnetic field configurations with fundamentally different shapes which can more successfully confine plasma for fusion-energy-relevant purposes. One alternative configuration is a toroidal, or donut-like, magnetic field geometry, which is a primary focus of the present work. As will be discussed in the next section, non-spatially-homogenous magnetic fields, as would be present in a toroidal magnetic field structure, give rise to a number of *plasma particle drifts* which can severely reduce the quality of the plasma confinement. To motivate the necessity of precisely constructed magnetic field geometries, the next section will discuss how these plasma particle drifts arise and what can be done to mitigate their adverse effects on plasma confinement.

1.2 Plasma particle drifts in magnetic fields

Three plasma particle drifts that are of particular importance with respect to plasma confinement dynamics in magnetic fields are the $\mathbf{E} \times \mathbf{B}$, ∇B , and curvature κ drifts. As the names suggest, these plasma particle drifts arise due to the presence of an electric field \mathbf{E} , a gradient in $|\mathbf{B}|$, and spatially-inhomogeneous magnetic field lines for the $\mathbf{E} \times \mathbf{B}$, ∇B , and κ drifts, respectively. To derive the form of these particle drifts, one must examine the Lorentz force, shown again in Eq. 1.3 below,

$$\mathbf{F} = q(\mathbf{E} + \mathbf{v} \times \mathbf{B}). \quad (1.3)$$

Disregarding gyromotion for the moment and examining the drift of the gyrocenter (the center of the helical orbit of a gyrating particle), one can solve for the velocity of a particle in the force-free case, i.e. when $\mathbf{F} = q(\mathbf{E} + \mathbf{v} \times \mathbf{B}) = 0$, which simplifies to the following in Eq. 1.4:

$$-\mathbf{E} = \mathbf{v}_{\mathbf{E} \times \mathbf{B}} \times \mathbf{B}, \quad (1.4)$$

which, if one solves for $\mathbf{v}_{\mathbf{E} \times \mathbf{B}}$ after applying $\mathbf{B} \times$ to both sides, one arrives at the following expression for the $\mathbf{E} \times \mathbf{B}$ drift $\mathbf{v}_{\mathbf{E} \times \mathbf{B}}$:

$$\mathbf{v}_{\mathbf{E} \times \mathbf{B}} = \frac{\mathbf{E} \times \mathbf{B}}{B^2}. \quad (1.5)$$

Since Eq. 1.5 is independent of particle charge and mass, both an ion and an electron, regardless of mass or charge, in the presence of both a magnetic and an electric field, will experience the same $\mathbf{E} \times \mathbf{B}$ drift. This drift moves charged particles away from their original field line, a potential problem if one is trying to confine a hot plasma.

The second plasma particle drift that will be discussed here is the ∇B drift. This drift affects charged particles in the presence of a magnetic field which exhibits the quality of having a spatially-varying $|\mathbf{B}|$. Using a similar strategy for deriving the ∇B drift as was used for the $\mathbf{E} \times \mathbf{B}$ drift, we begin with the Lorentz force:

$$\mathbf{F} = q(\mathbf{E} + \mathbf{v} \times \mathbf{B}), \quad (1.6)$$

where we take the velocity of our particle as the sum of a constant drift velocity and the velocity associated with the gyromotion, $\mathbf{v} = \mathbf{v}_D + \mathbf{v}_g$, and the magnetic field as the sum of a background field and a spatially-varying part, $\mathbf{B} = \mathbf{B}_0 + \mathbf{r} \cdot \nabla \mathbf{B}$. Substituting these expressions for \mathbf{v} and \mathbf{B} into Eq. 1.6 and taking $\mathbf{E} = 0$, we arrive at the following:

$$m \frac{d\mathbf{v}_g}{dt} = q(\mathbf{v}_g \times \mathbf{B}_0 + \mathbf{v}_g \times \mathbf{r} \cdot \nabla \mathbf{B} + \mathbf{v}_D \times \mathbf{B}_0 + \mathbf{v}_D \times \mathbf{r} \cdot \nabla \mathbf{B}), \quad (1.7)$$

where $m d\mathbf{v}_g/dt = q\mathbf{v}_g \times \mathbf{B}_0$ satisfies the lowest order Lorentz force balance and $\mathbf{v}_D \times \mathbf{r} \cdot \nabla \mathbf{B}$ is of second order, so it can be neglected, which simplifies Eq. 1.7 to

$$0 = \mathbf{v}_g \times \mathbf{r} \cdot \nabla \mathbf{B} + \mathbf{v}_D \times \mathbf{B}_0. \quad (1.8)$$

To proceed, a time average $\langle \rangle_t$ over the gyromotion is applied to Eq. 1.8. Note that $\langle \mathbf{v}_D \times \mathbf{B}_0 \rangle_t = \mathbf{v}_D \times \mathbf{B}_0$ because both \mathbf{v}_D and \mathbf{B}_0 are constant. Next, the \mathbf{r} vector must be decomposed into a gyrating part and a non-gyrating part, $\mathbf{r} = \mathbf{r}_0 + \mathbf{r}_g$, such that Eq. 1.8 can be written as:

$$0 = \langle \mathbf{v}_g \times \mathbf{r}_0 \cdot \nabla \mathbf{B} \rangle_t + \langle \mathbf{v}_g \times \mathbf{r}_g \cdot \nabla \mathbf{B} \rangle_t + \mathbf{v}_D \times \mathbf{B}_0. \quad (1.9)$$

Note that the first term in Eq. 1.9 will time-average to zero since $\langle \mathbf{v}_g \rangle_t = 0$ and \mathbf{r}_0 and $\nabla \mathbf{B}$ are temporally constant. This gives the following:

$$0 = \langle \mathbf{v}_g \times \mathbf{r}_g \cdot \nabla \mathbf{B} \rangle_t + \mathbf{v}_D \times \mathbf{B}_0, \quad (1.10)$$

where the first term can be computed if $\mathbf{r}_g = (\sin(\Omega_g t), q/|q| \cos(\Omega_g t))v_\perp/\Omega_g$ and $\mathbf{v}_g = (\cos(\Omega_g t), -q/|q| \cos(\Omega_g t))v_\perp$. Making these substitutions and carrying out the time average simplifies Eq. 1.10 to:

$$0 = \frac{qv_\perp^2}{2|q|\Omega_g} \nabla B + \mathbf{v}_D \times \mathbf{B}_0, \quad (1.11)$$

which implies that \mathbf{v}_D , which will now be denoted by the ∇B drift velocity $\mathbf{v}_{\nabla B}$, is equal to:

$$\mathbf{v}_{\nabla B} = \frac{mv_\perp^2}{2qB} \frac{\mathbf{B} \times \nabla B}{B^2}. \quad (1.12)$$

Unlike the $\mathbf{E} \times \mathbf{B}$ drift, the ∇B drift is not the same for particles of differing mass and charge, which complicates the matter of particle confinement. The derivation of the κ drift is similar to the derivation of the $\mathbf{E} \times \mathbf{B}$ drift, but rather than \mathbf{E} being present in the Lorentz force, \mathbf{E} is replaced with the centrifugal force per unit charge of a streaming particle $mv_\parallel^2 \mathbf{R}_c / (qR_c^2)$, where \mathbf{R}_c is the radius of curvature vector of a bending magnetic field line. Therefore, the equation to derive the κ drift reads:

$$\mathbf{F} = q \left(\frac{mv_\parallel^2 \mathbf{R}_c}{qR_c^2} + \mathbf{v}_\kappa \times \mathbf{B} \right) = 0, \quad (1.13)$$

and if one takes $\mathbf{B} \times$ of both sides and rearranges, one arrives at the following for the curvature drift:

$$\mathbf{v}_\kappa = \frac{mv_\parallel^2}{qB^2} \mathbf{B} \times \vec{\kappa}, \quad (1.14)$$

where $\vec{\kappa} = \hat{b} \cdot \nabla \hat{b}$. It should be noted that the existence of the ∇B and $\vec{\kappa}$ plasma particle drifts relies on the following assumption. The gyroradius of the drifting charged particle must be small with respect to the length scale associated with the spatial inhomogeneity of the magnetic field. If the gyroradius and the length scale in question are on the same order, then the trajectory of the charged particle is chaotic, where no straightforward expression for either drift exists. One brief aside that will be useful in the latter subsections of Ch. 5 is that ∇B and $\vec{\kappa}$ are equal when the normalized plasma pressure β is small.

As mentioned previously, these plasma particle drifts become especially problematic in toroidal confinement systems with spatially-inhomogeneous magnetic fields. This is because charged plasma particles will experience the various plasma particle drifts, in addition to collisions, during their trajectories of motion and potentially leave the confinement region. The various plasma drifts cause particles to drift off of their native flux surface. If, during the excursion from its native flux surface, a particle experiences a collision, this changes the native flux surface of said plasma particle. On average, this transport is radially outward, so problematic within the context of magnetic confinement fusion. This type of plasma particle loss is known as neoclassical transport. In unoptimized configurations, neoclassical transport is a problem for all classes of charged plasma particles; but, in devices designed to minimize

neoclassical transport, this is primarily a problem for a class of plasma particles known as “trapped particles”. Trapped particles have insufficient parallel energy to sample all parts of the magnetic field structure, and therefore only sample a subset of the magnetic field; this is due to the conservation of both energy and the magnetic moment $\mu = mv_{\perp}^2/(2B)$. In the absence of an electric field, the total energy E of a plasma particle is $E = mv_{\parallel}^2/2 + \mu B(z)$, where z denotes a coordinate parallel to the magnetic field. If a plasma particle has sufficiently small v_{\parallel} , then at some $z = z_{\text{turningpoint}}$, $\mu B(z_{\text{turningpoint}}) = E$, which implies that the particle will pause parallel motion momentarily before beginning to move in the antiparallel direction, thereby being trapped.

A non-negligible fraction of trapped plasma particles will leave the system and no longer be confined. Neoclassical transport of trapped particles is present in all types of three-dimensional toroidal magnetic confinement systems to some degree. In order to minimize particle losses due to neoclassical transport, one must construct toroidal magnetic systems so as to ensure that a maximal number of particles remain on their native magnetic flux surface.

In tokamaks, an example of which is shown in Fig. 1.1, perfect axisymmetry enforces a constraint on collisionless particle trajectories in the system such that, on average, they stay on their native flux surface. However, this work focuses on configurations which do not exhibit axisymmetry, and must therefore achieve reduced neoclassical transport by some other means, which will be discussed in the subsequent subsection.

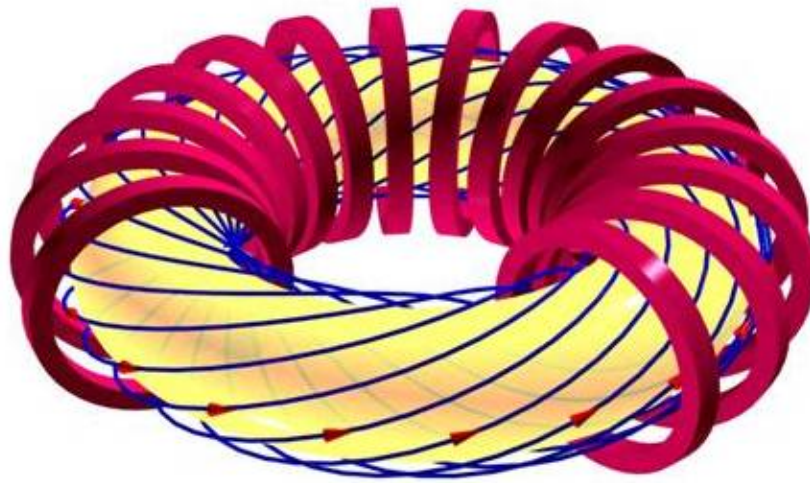


Figure 1.1: A toroidal magnetic field configuration known as the tokamak, where electric current is run through coils (shown in red) to produce a strong magnetic field (example magnetic field lines, which together comprise a magnetic flux surface, shown in blue) to confine hot plasma (shown in yellow).

1.3 Neoclassical and turbulent transport in stellarators

Inherently-three-dimensional toroidal magnetic field configurations are appealing as potential fusion reactor concepts since large plasma currents are not required to generate the confining poloidal magnetic field and therefore such configurations can avoid disruptions and operate in steady-state [1]. However, unoptimized three-dimensional systems, e.g. the classical stellarator or general three-dimensional magnetic fields, display poor neoclassical transport properties at low collisionality, a by-product of poorly-confined trapped-particle orbits. Neoclassical-transport-optimized stellarator configurations have addressed this issue by forcing the bounce-averaged particle excursion from a flux surface during a banana orbit to near zero [2,3].

One specific subset of neoclassical-transport-optimized configurations is that of quasi-symmetric (QS) stellarators, including quasi-axisymmetry (e.g. the National Compact Stellarator eXperiment [4]) and quasi-helical symmetry (e.g. the Helically Symmetric eXperiment [5]), which are two of the primary subjects of this work. Quasi-symmetric configurations achieve minimized neoclassical transport by enforcing a symmetry in the magnitude of the magnetic field such that $|\mathbf{B}|$ is a function of only a single variable on a given flux surface. The symmetry in QS systems implies a conserved canonical momentum p_ϕ for particles confined by the magnetic field. This conserved canonical momentum is approximately equal to $qA_\phi R$ [6], which is constant on a flux surface, where A_ϕ and R are the ϕ component of the magnetic vector potential and the major

radius of the system, respectively, and ϕ is the angle associated with the symmetry direction (whether toroidal, poloidal, or helical) of the system. Hence, particles are confined to surfaces of constant $A_\phi R$, which are flux surfaces. Heliotron-J, another subject of this work, is not a quasi-symmetric stellarator, but rather a heliotron.

In neoclassical-transport-optimized stellarators, the radially-outward transport is no longer necessarily dominated by neoclassical transport, but rather it can be dominated by anomalous transport, which is primarily thought to be drift-wave turbulence, as will be discussed in Ch. 2. One caveat to this statement is the possibility of turbulent-transport optimized stellarators, where turbulent transport could be minimized to neoclassical levels or lower. An example of a neoclassical-transport-optimized stellarator is HSX, as evidenced by data shown in Fig. 1.2 [18]. In the edge region ($r/a > 0.5$) of the plasma, where pressure gradients are higher, the difference between the predicted neoclassical transport and the experimentally-inferred electron diffusion coefficients is large, suggesting that turbulence significantly dominates relative to neoclassical transport. This constitutes a strong motivation for the study and minimization of turbulent transport in neoclassical-transport-optimized configurations like NCSX and HSX.

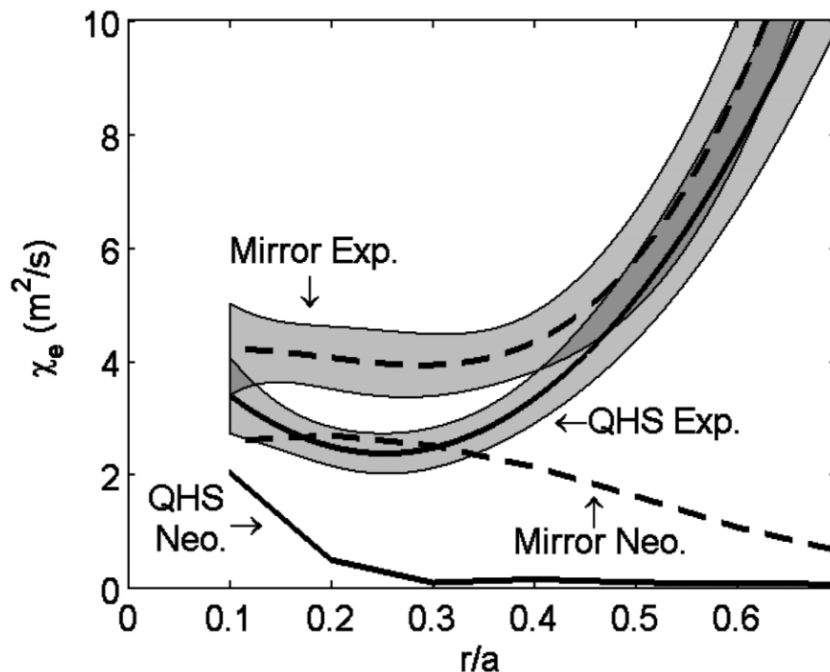


Figure 1.2: Electron diffusion coefficients as a function of minor radius for the HSX quasi-symmetric stellarator. There are four curves: “Mirror Exp.”, the experimental data for the mirror configuration achievable on HSX, “QHS Exp.”, the experimental data for the quasi-helically symmetric configuration achievable on HSX, “Mirror Neo.”, the numerically-calculated neoclassical transport predictions for the mirror configuration, and “QHS Neo.”, the numerically-calculated neoclassical transport predictions for the quasi-helically symmetric configuration. One of the primary conclusions to be drawn from these data is the significant difference between “QHS Neo.” and “QHS Exp.”, especially in the edge, an indication that anomalous (or turbulent) transport, and not neoclassical transport, is the dominant transport mechanism. [18]

1.4 HSX, NCSX, and Heliotron-J

In this work, the HSX, NCSX, and Heliotron-J magnetic equilibria are generated using the VMEC code [7], a 3D magnetohydrodynamics (MHD) code that assumes the existence of flux surfaces in which the user specifies a boundary shape (or the coil currents) using Eqs. (1.15) and (1.16), the toroidal magnetic flux, the shape of the magnetic axis, the number of field periods, the desired resolutions, the numerical tolerances, etc., and then a steepest-descent moment method minimization algorithm is carried out to generate a magnetic geometry which sits in a local minimum of total plasma energy $W = \int_{\Omega_p} (B^2/2\mu_0 + p)dV$ and also satisfies $\nabla \cdot \mathbf{B} = 0$ and $(\nabla \times \mathbf{B}) \times \mathbf{B} = \nabla p$, where p is the total plasma pressure, Ω_p is the plasma boundary, V is the plasma volume, and μ_0 is the magnetic permeability of free space.

$$R(\theta, \phi) = \sum_{n,m} \left[R_{n,m}^c \cos(n\phi - m\theta) + R_{n,m}^s \sin(n\phi - m\theta) \right], \quad (1.15)$$

$$Z(\theta, \phi) = \sum_{n,m} \left[Z_{n,m}^c \cos(n\phi - m\theta) + Z_{n,m}^s \sin(n\phi - m\theta) \right], \quad (1.16)$$

where R and Z are the usual cylindrical coordinates and, in general, $Z_{n,m}^c = R_{n,m}^s = 0$ due to stellarator symmetry. Note that quasi-symmetry is distinct from stellarator symmetry. Quasi-symmetry is defined above as a property of a magnetic configuration where $|\mathbf{B}|$ approximately depends on only a single variable within a flux surface and stellarator symmetry is the property of

a given magnetic equilibrium in which $f(R, \phi, Z) = f(R, -\phi, -Z)$ for any function f , where R , ϕ , and z are the usual cylindrical coordinates. A set of $R_{n,m}^c$ and $Z_{n,m}^s$ at a number of (n,m) values defines the boundary shape of the magnetic equilibrium.

Once the configuration has been generated using VMEC, one can view $|\mathbf{B}|$ on a flux surface to visualize the shape of the equilibrium and the structure of the magnetic field. Examples of $|\mathbf{B}|$ on the outermost flux surface for HSX, NCSX, and Heliotron-J are included in Figs. 1.3, 1.4, and 1.5, respectively. A more detailed, quantitative examination of the magnetic field can also be carried out. In general, as a result of stellarator symmetry, the magnetic field strength $|\mathbf{B}|$ can be written in the following manner,

$$|\mathbf{B}| = B_{00}(r_{\text{eff}}/a) \left[1 + \sum_{m,n} \epsilon_{m,n}(r_{\text{eff}}/a) \cos(n\xi - m\theta) \right], \quad (1.17)$$

where ξ and θ are the toroidal and poloidal angles as written in Boozer coordinates [2,8], $B_{00}(r_{\text{eff}}/a)$ is the $(n = 0, m = 0)$ component of the magnetic field, and $\epsilon_{m,n}(r_{\text{eff}}/a)$ denotes the relative strength of the (n,m) modes, where r_{eff} and a are an effective radial coordinate implicitly defined by the normalized toroidal magnetic flux $s_0 = (r_{\text{eff}}/a)^2$ and the minor radius, respectively. One can plot a Boozer spectrum $\epsilon_{m,n}(r_{\text{eff}}/a)$ as a function of r_{eff}/a to examine a magnetic equilibrium more quantitatively. In quasi-symmetric stellarators, one Fourier mode $\epsilon_{m,n}(r_{\text{eff}}/a)$ dominates other components over a majority of the

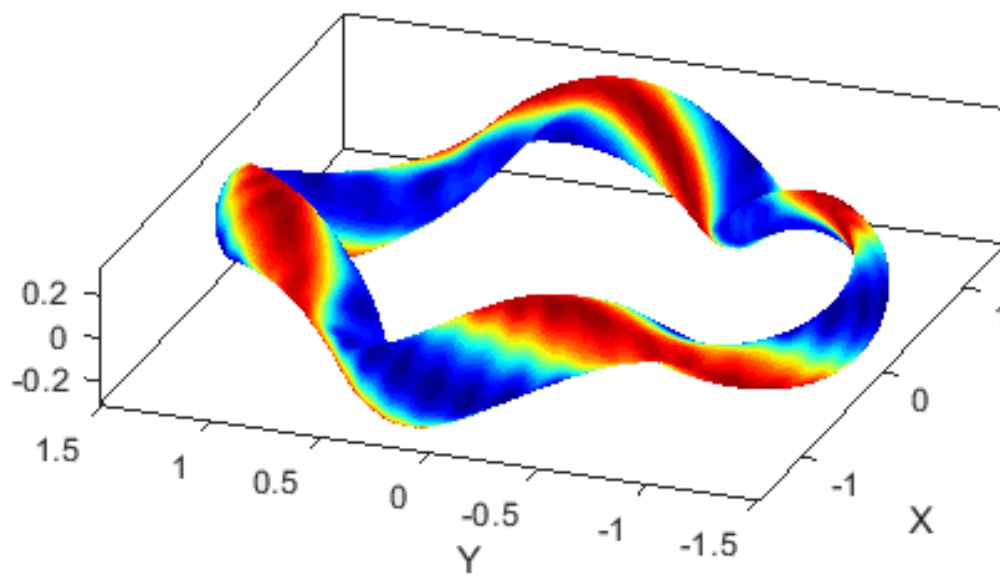


Figure 1.3: $|\mathbf{B}|$ on the outermost flux surface of the quasi-helically symmetric HSX magnetic equilibrium. Note that the lines of relatively constant magnetic field strength form a helix. Red (blue) indicates regions of high (low) magnetic field strength. The axes correspond to spatial Cartesian coordinates.

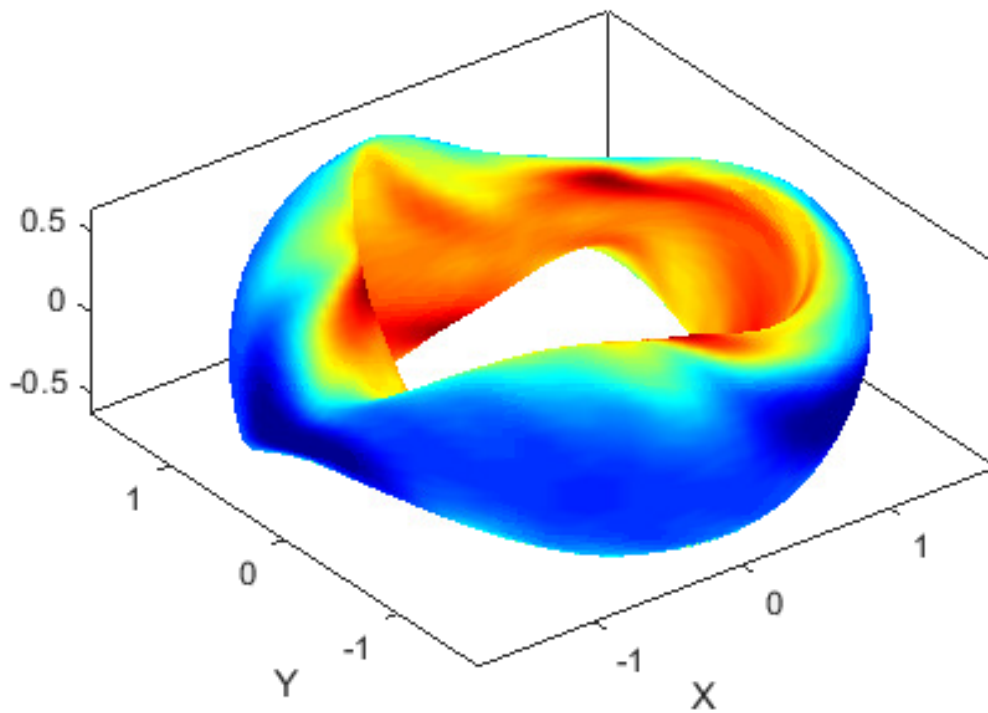


Figure 1.4: $|\mathbf{B}|$ on the outermost flux surface of the quasi-axisymmetric NCSX magnetic equilibrium. Note that the high-field side of the flux surface is always the inboard side, like in a tokamak. Red (blue) indicates regions of high (low) magnetic field strength. The axes correspond to spatial Cartesian coordinates.

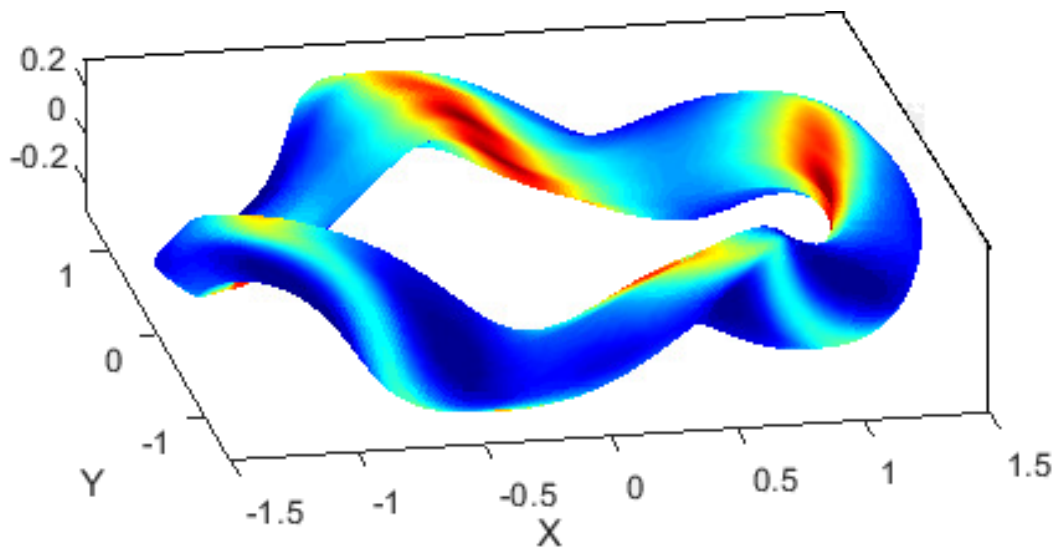


Figure 1.5: $|\mathbf{B}|$ on the outermost flux surface for the non-quasi-symmetric Heliotron-J magnetic equilibrium. Note that there is no line of constant magnetic field strength that can be drawn over one full toroidal transit. Heliotron-J does not exhibit any form of quasi-symmetry. Red (blue) indicates regions of high (low) magnetic field strength. The axes correspond to spatial Cartesian coordinates.

minor radius. Boozer spectra for HSX, NCSX, and Heliotron-J are given in Figs. 1.6, 1.7, and 1.8, respectively.

The HSX equilibrium is a four-field-period configuration, where the number of field periods is defined as the number of times the equilibrium repeats itself per one toroidal transit, with aspect ratio $A = R/a \approx 10$, mean magnetic field $\langle B \rangle \approx 1$ T, and low magnetic shear $\hat{s} = (r_{\text{eff}}/q) dq/dr_{\text{eff}} = -(r_{\text{eff}}/\iota) d\iota/dr_{\text{eff}} \approx -0.05$, where q and ι are the safety factor and rotational transform, respectively, at $s_0 = (r_{\text{eff}}/a)^2 \approx 0.5$. The major (minor) radius of HSX is approximately 1.2 m (0.12 m). It should also be noted that HSX is not optimized for a specific normalized plasma pressure $\beta = 2\mu_0 p/B^2$. Therefore, the HSX equilibrium used throughout has $\beta = 0$. This is also a typical operating β experimentally for HSX.

The baseline NCSX equilibrium has total normalized plasma pressure $\beta \approx 4\%$, three field periods, aspect ratio $A \approx 4.5$, mean magnetic field $\langle B \rangle \approx 1.6$ T, and sizable average magnetic shear $\hat{s} \approx -0.5$ at $s_0 \approx 0.5$. The major (minor) radius of NCSX is 1.4 m (0.33 m). The use of the finite- β NCSX equilibrium is motivated by the fact that the configuration was optimized for finite- β experiments.

It should be noted that average and local magnetic shear are distinct quantities. The average magnetic shear is defined above and is the flux-tube average of the local shear. The local magnetic shear $\hat{s}_{\text{loc}} = (\hat{\mathbf{b}} \times \hat{\mathbf{n}}) \cdot \nabla \times (\hat{\mathbf{b}} \times \hat{\mathbf{n}})$ [9,10], where $\hat{\mathbf{b}}$ and $\hat{\mathbf{n}}$ are unit vectors in the directions parallel to the magnetic field

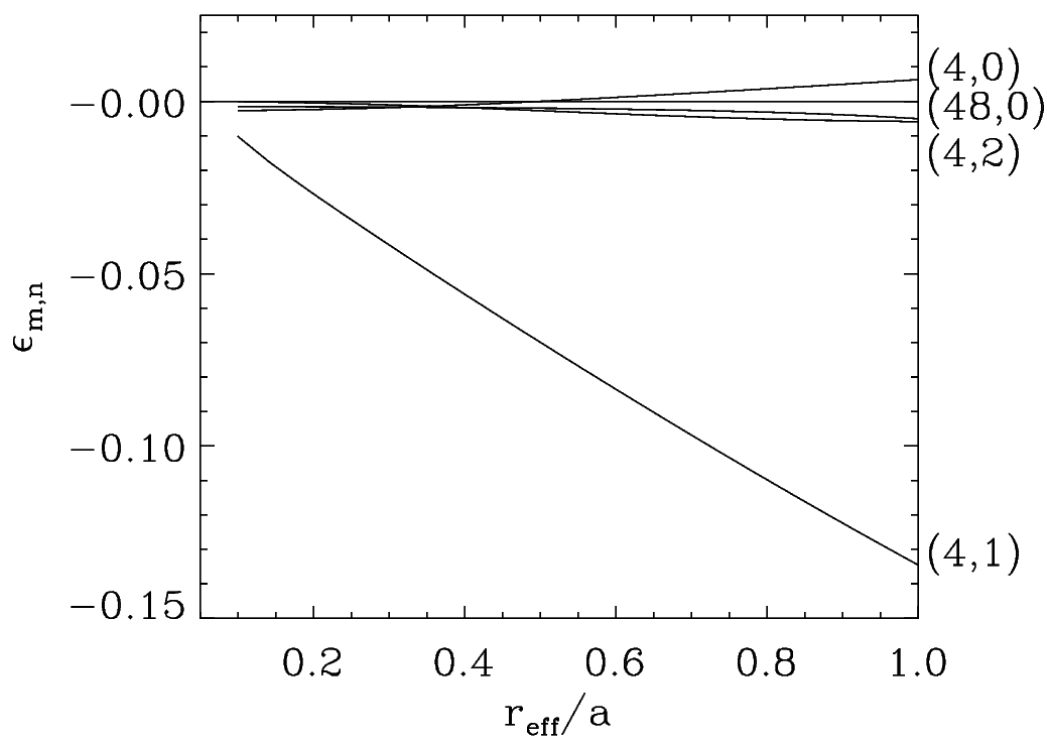


Figure 1.6: The Boozer spectrum for the HSX equilibrium. Only four magnetic Fourier modes are included as subsequent modes lie almost directly on top of either the $(4, 2)$ or $(4, 0)$ mode. The fact that the magnitude of the $(4, 1)$ mode is large relative to the non-symmetric components of the Boozer spectrum highlights the quasi-helical symmetry of HSX. The $(0, 0)$ component, which is equal to 1, is omitted for readability.

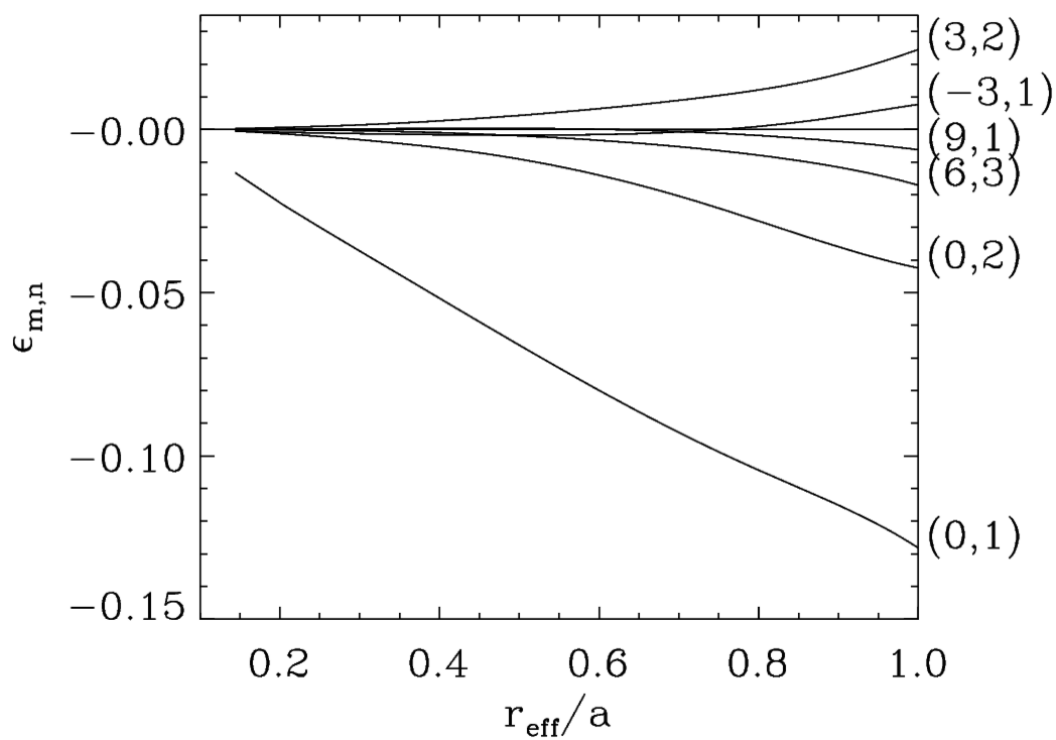


Figure 1.7: The Boozer spectrum for the baseline NCSX equilibrium. Only the six magnetic Fourier modes with the largest amplitude are included. The large magnitude of the $(0, 1)$ mode relative to the non-axisymmetric modes highlights the quasi-axisymmetry of NCSX. The $(0, 0)$ component, again equal to 1, is excluded for readability.

and locally normal to the flux surface, respectively, can vary significantly with field-line label and along the field line. This distinction will be important when discussing qualitative differences in eigenmode structure between various types of QS stellarator equilibria.

The Heliotron-J configuration has total normalized plasma pressure $\beta \approx 0.03\%$, four field periods, aspect ratio $A \approx 7.3$, mean magnetic field $\langle B \rangle \approx 1.35$ T, and average magnetic shear $\hat{s} \approx 0.028$ at $s_0 \approx 0.5$, which is comparable to the magnetic shear of HSX. The major (minor) radius of Heliotron-J is 1.18 m (0.162 m). As noted previously, Heliotron-J is not quasi-symmetric.

After using the MHD equilibrium solver VMEC [7] to generate the HSX, NCSX, and Heliotron-J geometries, the GIST code [11] then calculates the necessary magnetic geometry data for the desired flux tube at the specified normalized toroidal magnetic flux s_0 .

One additional topic that is relevant to the motivation of this work is turbulence-optimized and neoclassically-optimized stellarators. Presently, turbulence contributes significantly to many of the cutting-edge stellarator experiments worldwide. However, this is not something that must be true for future experiments or reactors. One of the primary motivations for this work is developing a deeper understanding of plasma turbulence so that said knowledge can be leveraged to develop magnetic confinement systems which exhibit greatly

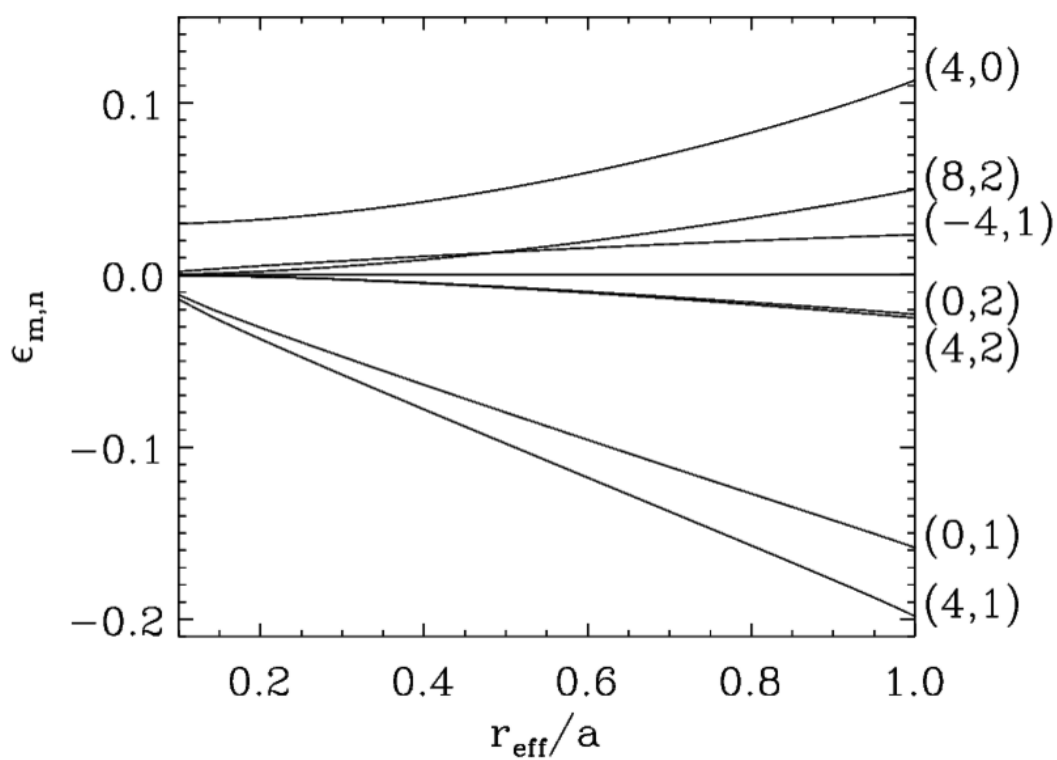


Figure 1.8: The Boozer spectrum for Heliotron-J, where the seven largest-magnitude modes are included. The $(0,0)$ component, again equal to 1, is omitted for readability. Note that the $(0,1)$, $(4,0)$, $(8,2)$ and $(4,1)$ modes have comparable magnitude, a confirmation that Heliotron-J is not quasi-symmetric.

reduced turbulent transport. This would be a significant step toward an economical fusion reactor, as high turbulent transport and the resulting high heat fluxes are major unsolved problems in the field of fusion energy.

1.5 Thesis Outline

This dissertation is organized as follows. Chapter 2 discusses turbulent transport in greater detail, specifically outlining the drift-wave instability mechanism as well as the two instabilities discussed in this dissertation: ion temperature gradient (ITG) and kinetic ballooning modes (KBMs). Following Ch. 2, Chapter 3 introduces the numerical scheme known as gyrokinetics and the specific gyrokinetic code `GENE` that is used in this work. Chapter 4 consists of a comparison of both linear and nonlinear ITG dynamics between HSX and NCSX, highlighting the importance of nonlinear physics relative to linear physics when analyzing the turbulence properties of a given quasi-symmetric stellarator. Chapter 5 transitions from the ITG portion of the dissertation to the KBM results, where again the linear predictions are insufficient and full nonlinear analysis is necessary. Lastly, Chapter 6 summarizes the main results of this dissertation and puts forth a number of avenues for future work.

Citations

[1] Gates, D.A., Anderson, D.T., Anderson, F.S.B., Zarnstorff, M., Spong, D.A., Weitzner, H., Neilson, G.H., Ruzic, D.N., Andruczyk, D., Harris, J.H. *et al.* 2018 Stellarator research opportunities: a report of the National Stellarator Coordinating Committee. *J. Fusion Energy* **38** (1), 51-94.

[2] Boozer, A. H. 1983 Transport and isomorphic equilibria. *Phys. Fluids* **26** (2), 496-499.

[3] Mynick, H.E. 2006 Transport optimization in stellarators. *Phys. Plasmas* **13** (5), 058102.

[4] Neilson, G.H., Zarnstorff, M.C., Lyon, J.F., & The NCSX Team 2002 Quasi-symmetry in stellarator research 5. Status of physics design of quasi-symmetry stellarators 5.1 Physics design of the National Compact Stellarator Experiment. *J. Plasma Fusion Res.* **78** (3), 214-219.

[5] Talmadge, J.N., Anderson, F.S.B., Anderson, D.T., Deng, C., Guttenfelder, W., Likin, K.M., Lore, J., Schmitt, J.C., & Zhai, K. 2008 Experimental tests of quasisymmetry in HSX. *Plasma Fusion Res.* **3**, S1002.

- [6] Landreman, M., Lecture Notes - Quasisymmetry: A hidden symmetry of magnetic fields, (2019).
- [7] Hirshman, S.P., Van Rij, W.I., & Merkel, P. 1986 Three-dimensional free boundary calculations using a spectral Green's function method. *Comput. Phys. Commun.* **43** (1), 143-155.
- [8] Boozer, A.H. 1981 Plasma equilibrium with rotational magnetic surfaces. *Phys. Fluids* **24** (11), 1999.
- [9] Greene, J.M. & Johnson, J.L. 1968 Interchange instabilities in ideal hydromagnetic theory. *Plasma Phys.* **10**, 729-745.
- [10] Hegna, C.C. 2000 Local three-dimensional magnetostatic equilibria. *Phys. Plasmas* **7** (10), 3921.
- [11] Xanthopoulos, P., Cooper, W.A., Jenko, F., Turkin, Y., Runov, A., & Geiger, J. 2009 A geometry interface for gyrokinetic microturbulence investigations in toroidal configurations. *Phys. Plasmas* **16** (8), 082303.
- [12] Brizard, A.J. & Hahm, T.S. 2007 Foundations of nonlinear gyrokinetic theory. *Rev. Mod. Phys.* **79** (2), 421-468.

- [13] For more information, see www.genecode.org.
- [14] G. Lapenta et al., presentation at 47th annual APS-DPP, Denver, CO, <http://meetings.aps.org/link/BAPS.2005.DPP.GI2b.1>, 2005.
- [15] F. Merz, PhD Thesis, (2008).
- [16] Monreal, P., Sánchez, E., Calvo, I., Bustos, A., Parra, F.I., Mishchenko, A., Könies, A., & Kleiber, R. 2017 Semianalytical calculation of the zonal-flow oscillation frequency in stellarators. *Plasma Phys. Control. Fusion* **59** (6), 065005.
- [17] Faber, B.J., Pueschel, M.J., Terry, P.W., Hegna, C.C., & Roman, J.E. 2018 Stellarator microinstabilities and turbulence at low magnetic shear. *J. Plasma Phys.* **84** (5), 905840503.
- [18] Canik, J.M., Anderson, D.T., Anderson, F.S.B., Clark, C., Likin, K.M., Talmadge, J.N., & Zhai, K. 2007 Reduced particle and heat transport with quasisymmetry in the helically symmetric experiment. *Phys. Plasmas* **14** (5), 056107.

Chapter 2

Drift-wave turbulent transport in quasi-symmetric stellarators

The purpose of this chapter is to extend the introduction of radial plasma transport in magnetic confinement systems from Ch. 1 to include an introductory discussion of drift-wave turbulent transport. As previously mentioned, even with the reduction in transport due to neoclassical optimization, there is still an additional significant component to the radial transport that is likely due to turbulence [1-3]. Turbulence in toroidal systems can be driven as a result of *drift-wave* instabilities such as ion-temperature-gradient [4-8], trapped-electron [2,9-11], and kinetic ballooning modes [12-14]. Similar to turbulence in everyday life, plasma turbulence arises due to inhomogeneity, or gradients, in various quantities. In the case of magnetic confinement, this inhomogeneity can consist of the large temperature and density gradients required for fusion-relevant plasma confinement. These temperature and density gradients are unstable and the system equilibrates these gradients via turbulence. Investigation of ITG and KBM turbulence in HSX, NCSX, and Heliotron-J is the focus of this research.

2.1 Drift-wave linear instability mechanism

Drift waves are plasma waves which arise due to both the plasma particle drifts discussed in Ch. 1 and other crucial physics that differentiates a drift wave from, for example, an interchange mode. An instability, within the context of drift waves, is a self-reinforcing perturbation. The fluctuation is able to access free energy in e.g. a pressure gradient to increase its amplitude. An intuitive example of an unstable system is a sphere at the top of a frictionless hill. Any arbitrarily small perturbation to the position of the ball away from the unstable equilibrium allows the ball to access free energy in the gradient of the gravitational potential to move down the hill, reinforcing the initial perturbation. In fusion-relevant plasmas, the physical mechanism behind drift wave instabilities is not as intuitive.

The standard picture of drift-wave instability evolution in toroidal magnetic confinement systems is outlined below in Fig. 2.1. The physical setup in which drift waves arise is as follows. Given a strong background magnetic field in the positive z -direction, pressure and $|\mathbf{B}|$ gradients in the negative x -direction, and a pressure $p \propto p_0 \exp(ik_y y - i\omega t)$ fluctuation with finite k_y , the normal curvature drift (which is in nearly the same direction as $\nabla_{\perp}|\mathbf{B}|$ for small values of β) that the electrons and ions experience are in opposite directions due to the opposite charge of ions and electrons. This causes a locally-varying electric field which induces an $\mathbf{E} \times \mathbf{B}$ drift that reinforces the initial pressure perturbation. This reinforcement of the initial perturbation

is what constitutes an instability. As one can see in Fig. 2.1, the spatially-varying $\mathbf{E} \times \mathbf{B}$ drift advects plasma of higher (lower) pressure toward the right (left) in regions where the initial perturbation is already transporting plasma of higher (lower) pressure to the right (left); this means that the amplitude of the fluctuation will increase in time, so long as the pressure gradient is present.

Note that if the $|\mathbf{B}|$ gradient were oppositely directed, in the positive x -direction, the electric field induced by the charge separation due to the differing curvature drift directions for ions and electrons would be such that the initial pressure fluctuation is not self-reinforcing, and is instead stable. When both the pressure gradient and curvature are in the same direction, this is called a region of “bad curvature”. Both the ITG and KBM instability mechanisms are driven by bad curvature. The bad curvature region is generally at the outboard midplane of a given magnetic geometry. This concept will be important when discussing linear instability dynamics for ITG and KBM. However, the notion of bad curvature alone is insufficient to describe the entirety of the drift-wave instability mechanism, as things are more complex than this relatively simple picture. There must be a physical mechanism present which creates a phase shift between the ion temperature and the electrostatic potential Φ , in the case of ITG for example, to drive a drift wave. Generally, this phase shift is caused by non-adiabatic contributions to either the electron or ion physics derived from physical mechanisms such as collisions, parallel dynamics, or

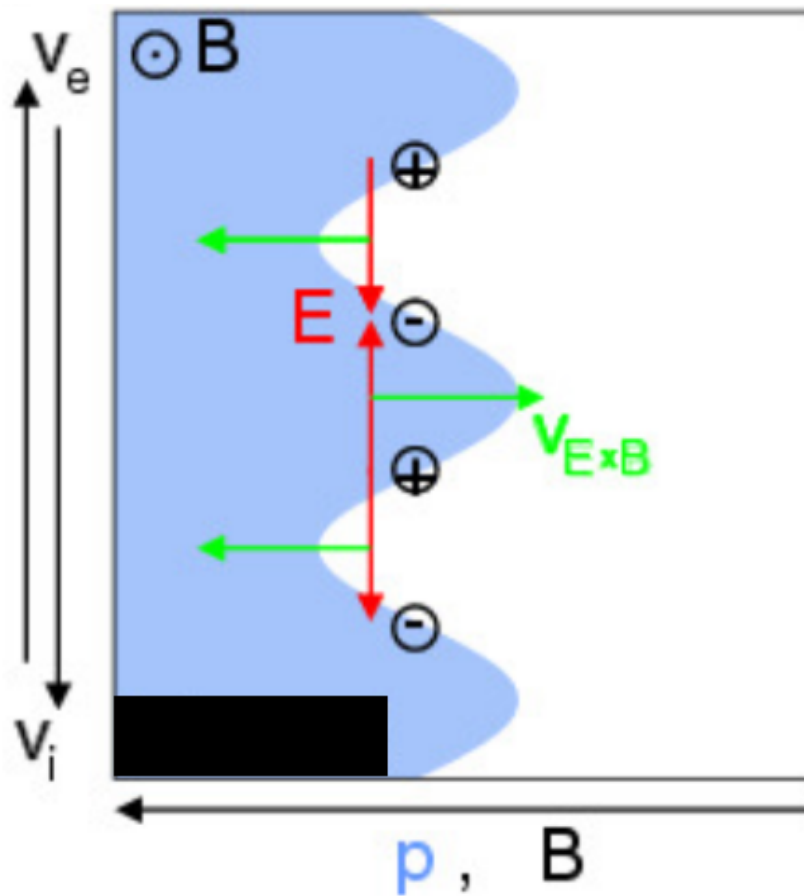


Figure 2.1: The standard drift wave scenario for toroidal magnetic geometries. Arrows on the bottom of the figure indicate the direction of increasing pressure and $|\mathbf{B}|$ on the x -axis. Arrows on the left of the figure indicate the direction of the curvature drift of each particle species on the y -axis. The background magnetic field is directed out of the page in the positive z -direction. The blue sinusoidal variation is a fluctuation of the plasma pressure p with finite k_y . This figure is taken from Grulke and Klinger, (2002) [15].

magnetic drifts. Depending on which physical mechanism is contributing to the non-adiabatic physics, different types of drift waves arise.

One important facet of the ITG mode is the difference between toroidal- and slab-like ITG. In the above example of a drift wave, a toroidal geometry is assumed, as there is a gradient in \mathbf{B} . However, it is possible for drift waves to be unstable without the presence of the \mathbf{B} gradient; this is called a slab geometry. Dynamics parallel to the magnetic field provide the physical mechanism for the ITG instability in this case [15]. The fact that certain magnetic confinement configurations can favor one flavor of ITG over another will have important consequences for the turbulent dynamics, as will be seen in Ch. 4.

As previously mentioned, this dissertation focuses on two drift-wave instabilities and the resulting turbulence: the ITG and KBM. The two subsequent subsections will describe these two drift-waves instabilities.

2.2 The ion-temperature-gradient (ITG) mode

As the name suggests, the ion-temperature-gradient mode is destabilized by strong gradients in the ion temperature. The physical mechanism underlying the ITG mode is coupling between a drift wave and an ion acoustic wave, enabling energy transfer from thermal ions to the drift wave [16,17]. While the ITG mode is a drift-wave, it has a fluid-like character, as it can be crudely derived using fluid equations, where fluid equations are derived by taking velocity-space moments of the Vlasov equation given in Eq. 2.13.

The ITG mode is also stabilized by increasing density gradient. This can be seen in the dispersion relation of the ITG mode, where a dispersion relation is an equation which describes the growth rate and real frequency of a given instability as a function of the wavenumber and other plasma parameters.

A simple, straightforward derivation of an ITG mode dispersion relation can begin with the ion continuity, ion parallel momentum, and ion energy equation given by Eqs. (2.1)-(2.3). It is worth noting that this set of equations will be relevant again during the discussion of the three- and five-field models in Ch. 5.

$$\frac{\partial n_i}{\partial t} + \nabla n_i \cdot \mathbf{v}_{\mathbf{E} \times \mathbf{B}} + n_i (\nabla_{\perp} \cdot \mathbf{v}_{\mathbf{E} \times \mathbf{B}} + \nabla_{\parallel} v_{\parallel}) = 0 \quad (2.1)$$

$$m_i n_i \left(\frac{\partial v_{\parallel}}{\partial t} + \mathbf{v} \cdot \nabla v_{\parallel} \right) + \nabla_{\parallel} (p_i + n_i e \Phi) = 0 \quad (2.2)$$

$$\frac{1}{T_i} \frac{\partial T_i}{\partial t} - \frac{2}{3} \frac{1}{n_i} \frac{\partial n_i}{\partial t} - \frac{i k_y \Phi}{B} \left(\frac{1}{T_i} \frac{dT_i}{dx} - \frac{2}{3} \frac{1}{n_i} \frac{dn_i}{dx} \right) = 0, \quad (2.3)$$

where n_i , v_{\parallel} , T_i , e , k_y and Φ are the ion density, ion parallel velocity, ion temperature, elementary charge, binormal wavenumber, and electrostatic potential, respectively. After linearizing, taking fluctuating quantities to evolve as $\exp(i(k_y y + k_z z - \omega t))$, and a little massaging, Eqs. (2.6), (2.7), and (2.8) simplify to the following, where a \tilde{A} denotes a linearized quantity:

$$-i\omega \frac{\tilde{n}}{n_i} - \frac{k_y}{Bn_i} \frac{dn_i}{dx} \tilde{\Phi} + ik_z \tilde{v}_{\parallel} = 0 \quad (2.4)$$

$$-i\omega m_i n_i \tilde{v}_{\parallel} + ik_z (\tilde{p}_i + n_i e \tilde{\Phi}) = 0 \quad (2.5)$$

$$-i\omega \frac{1}{T_i} \tilde{T}_i + i \frac{2\omega}{3n_i} \tilde{n}_i - \frac{ik_y \tilde{\Phi}}{B} \left(\frac{1}{T_i} \frac{dT_i}{dx} - \frac{2}{3} \frac{1}{n_i} \frac{dn_i}{dx} \right) = 0. \quad (2.6)$$

Given that the above set of equations consists of three equations in three unknowns, they can be algebraically combined to determine the dispersion relation of the system, which gives the following equation:

$$1 + \frac{k_y T_e}{\omega e B n_i} \frac{dn_i}{dx} - \frac{k_z^2 T_i}{\omega^2 m_i} \left(\frac{5}{3} + \frac{T_e}{T_i} - \frac{k_y T_e}{\omega e B n_i} \frac{dn_i}{dx} \left(\eta_i - \frac{2}{3} \right) \right) = 0, \quad (2.7)$$

where $\omega = \omega_r + i\gamma$, ω_r , γ , η_i , k_z , and T_e are the frequency, real frequency, growth rate, the ratio of the ion temperature gradient to the density gradient, parallel wavenumber, and the electron temperature, respectively. Note that because a fluid treatment of the ion species was used here, this dispersion relation is not exactly correct, but it will give a reasonable intuition for how the system will behave. For example, when $\omega \gg \omega_{*e} = \frac{k_y T_e}{e B n_i} \frac{dn_i}{dx}$, the system exhibits ion acoustic waves, as the dispersion relation reduces to the familiar form for ion acoustic waves; but, when $\omega \ll \omega_{*e}$, then there can be instability, and a major determining factor for instability is whether η_i is less than 2/3 or greater, a threshold for ITG instability in this fluid derivation. It should also be noted that this formulation assumes that the wavelength of a given mode is shorter than the density gradient scale ($L_n^{-1} < k$), which is an approximation

of weak inhomogeneity, as L_n is essentially taken to be a constant. If this assumption does not hold for a given system, this derivation is inaccurate.

2.3 The kinetic ballooning mode (KBM)

The kinetic ballooning mode is characteristically different than the ITG mode in a number of ways. First, the ITG mode is electrostatic, having substantial growth rates at $\beta \rightarrow 0$, while the KBM is an electromagnetic mode, meaning that finite \mathbf{B} (and therefore finite β) fluctuations are required for instability. It is also important to note that ITG modes are stabilized by increasing β , whereas KBMs are destabilized by increasing β . Typically, the onset of KBM-driven turbulent transport is associated with breaching the ideal MHD ballooning stability boundary [18-21]. However, it has been shown that ion magnetic drifts can introduce an additional physical effect not present in simple MHD modeling in the small-perpendicular-wavelength limit [22,23]. Specifically, coupling between the KBM and thermal ions provides additional free energy to the mode. This resonant effect arises from non-adiabatic contributions to the ion density fluctuations in a kinetic treatment of the governing equations [24,25]. This effect can be qualitatively captured in a two-fluid treatment of the system, suggesting that the mode is somewhat fluid-like since the kinetic treatment is unnecessary for qualitative purposes [24].

Here, the focus lies on the $\beta_{\text{crit}}^{\text{KBM}}$ value at which KBM becomes the most unstable microinstability; for a discussion of different threshold definitions,

see [19]. An analysis of various Wendelstein 7-X (W7-X) equilibria [26], an optimized quasi-omnigenous stellarator, with respect to KBMs suggests both that, for sufficiently large β , peak KBM growth rates occur as $k_y \rightarrow 0$ for a number of physically-relevant parameter regimes and that the critical β at which KBMs become unstable is on the order of $\beta_{\text{crit}}^{\text{KBM}} \approx 1\%$, depending on the specific equilibrium. It is also shown in the same analysis that, in low-average-magnetic-shear W7-X configurations, KBMs can be destabilized before the ideal MHD limit $\beta_{\text{crit}}^{\text{MHD}}$. As will be shown here, the KBM threshold can be much lower than the MHD threshold $\beta_{\text{crit}}^{\text{MHD}}$, with $\beta_{\text{crit}}^{\text{KBM}} \approx 0.2\%$ in HSX over a range of wavelengths, raising the possibility that such configurations exhibit poor KBM turbulence and confinement properties. However, it is shown in this dissertation that the saturated nonlinear heat flux is greatly reduced relative to the electrostatic ITG case when $\beta > \beta_{\text{crit}}^{\text{KBM}}$. This implies that expectations based on linearly-calculated $\beta_{\text{crit}}^{\text{KBM}}$ values, e.g., that nonlinear heat fluxes tend to increase for $\beta > \beta_{\text{crit}}^{\text{KBM}}$, do not accurately account for critical nonlinear dynamics. Rather than presenting a full derivation of a KBM dispersion relation, the final result will instead be given as the derivation is more involved than in the ITG case:

$$\frac{k_z k_{\perp}^2 k_z}{k_{De}^2} = -\frac{(\omega - \omega_{*e})}{1 + \tau(1 - I_i)} + (\omega - \omega_{*e})(\omega - \omega_{De}) + \eta_e \omega_{*e} \omega_{De}, \quad (2.8)$$

where

$$k_z = -\frac{i}{qR} \frac{\partial}{\partial \theta} \quad (2.9)$$

$$k_\perp = k_y^2 (1 + (s\theta - \alpha \sin(\theta))^2) \quad (2.10)$$

$$\omega_{Dj} = \frac{T_j}{eBR} k_y (\cos(\theta) + \sin(\theta)(s\theta - \alpha \sin(\theta))) \quad (2.11)$$

$$I_i = \int \frac{\omega + \hat{\omega}_{*i}(v^2)}{\omega + \hat{\omega}_{Di}(v)} J_0^2(\Lambda_i) f_{Mi} d\mathbf{v}, \quad (2.12)$$

where τ , I_i , θ , α , s , R , J_0 , and f_{Mi} are the temperature ratio, the non-adiabatic contribution to the ion density fluctuations, a poloidal-like coordinate, a parameter correlated to the normalized plasma pressure β , the average magnetic shear, the major radius, a zeroth order Bessel function, and a Maxwellian distribution for the ions, respectively [24,25]. It should be noted that these equations are tokamak-specific and do not account for complicated geometrical effects that are present in stellarator configurations. For more information on this dispersion relation, please see references 24 and 25 by Hirose *et al.*. Eq. 2.8 has been studied extensively and does indeed exhibit KBMs, even in parameter regimes not predicted by previous theory such as negative shear tokamaks. While it is difficult to intuit much at first glance from Eq. (2.8), it is important to note the resonance condition in the non-adiabatic contribution to the perturbed ion density I_i , where if $\omega + \hat{\omega}_{Di} \approx 0$, then I_i has a resonant contribution and can fundamentally change the nature of Eq. (2.8) and the otherwise expected behavior. This resonance is the ion magnetic drift resonance previously mentioned that may be playing an important role in the peculiar $\beta_{\text{crit}}^{\text{KBM}}$ behavior observed in low- \hat{s} magnetic equilibria. Note that this

treatment is inherently kinetic, and not fluid as was the case for ITG. This is why the derivation is more complicated.

2.4 Turbulent transport

Within the context of fusion energy, turbulent transport is one of the major barriers to a successful fusion reactor. Plasma turbulence is a difficult subject to study for a number of reasons. One reason is inherently tied to the physics of plasma turbulence, and that is the disparity in time- and length-scales of the important dynamics of the system. For example, regarding the separation of scales in time, one of the faster time-scales is the gyromotion of the electron, which can be on the order of nanoseconds. This is contrasted with the time-scale over which the plasma density and temperature profiles change, which can be on the order of seconds. This implies a disparity in time-scales on the order of 10^9 or higher. Similarly, for the separation of length-scales, where the disparity can be on the order of 10^6 or higher, where one of the smaller scales is the gyroradius of electrons (millimeters) and one of the larger scales is the mean free path of charged particles streaming along a magnetic field line (kilometers). This difference in scales makes plasma turbulence simulation especially difficult, as will be further discussed in Ch. 3.

Another reason why plasma turbulence is so difficult to understand is the structure of the set of equations that must be solved to ascertain the turbulent dynamics. Generally, the Vlasov equation and Maxwell's equations,

shown below, can be solved iteratively in time and space to determine how the electromagnetic fields and the plasma distribution function(s) evolve in time and space.

$$\frac{\partial f_j}{\partial t} + \mathbf{v} \cdot \frac{\partial f_j}{\partial \mathbf{x}} + \frac{\mathbf{F}_j}{m_j} \cdot \frac{\partial f_j}{\partial \mathbf{v}} = 0 \quad (2.13)$$

$$\nabla \cdot \mathbf{E} = \frac{\rho}{\epsilon_0} \quad (2.14)$$

$$\nabla \cdot \mathbf{B} = 0 \quad (2.15)$$

$$\nabla \times \mathbf{E} = -\frac{\partial \mathbf{B}}{\partial t} \quad (2.16)$$

$$\nabla \times \mathbf{B} = \mu_0 \left(\mathbf{J} + \epsilon_0 \frac{\partial \mathbf{E}}{\partial t} \right). \quad (2.17)$$

This is a nonlinear system of partial differential equations where a number of assumptions and simplifying ordering schemes must be applied before it can be solved numerically in a reasonable amount of time. In order to further convey the difficulty of solving the above system of equations, one can examine one of the nonlinearities of the system. The $\mathbf{E} \times \mathbf{B}$ nonlinearity, denoted by N , which pops out of the Vlasov equation after some substitutions and massaging, can take the following form:

$$N[g] = \sum_{\mathbf{k}'_{\perp}} (k'_x k_y - k_x k'_y) \chi(\mathbf{k}'_{\perp}) g_j(\mathbf{k}_{\perp} - \mathbf{k}'_{\perp}), \quad (2.18)$$

where χ and g_j are a combined electromagnetic potential and a modified plasma distribution function, respectively. The $\mathbf{E} \times \mathbf{B}$ nonlinearity may look simple enough, it can be written on a single line after all. However, looking

more closely, Eq. (2.18) implies that for each \mathbf{k}_\perp at which one would like to evaluate N , one must compute χ , g_j , and $(k'_x k_y - k_x)$ at wavenumbers different than \mathbf{k}_\perp . This is computationally expensive considering that generally nonlinear simulations have somewhere between 50 and 100 k_y modes. The computational expense of solving the full system only gets larger as you increase the difference between the largest and smallest wavelengths in your nonlinear simulation or increase the resolution in the perpendicular direction, which must be done to conduct the necessary convergence tests to ensure that your results are physical. As will be discussed in Ch. 3, there are clever ways to solve Eqs. (2.13)-(2.18) such that interesting physics can be ascertained from nonlinear simulations.

Fortunately, it is also possible to solve the Vlasov-Maxwell system of equations without the $\mathbf{E} \times \mathbf{B}$ nonlinearity as a means of studying the important linear physics. Generally, in a nonlinear simulation, all fluctuating quantities are initiated with small amplitudes and then grow exponentially for some period of time. Linear simulations allow one to probe this linear regime, i.e. allowing one to investigate the type of modes present in the system, how many unstable modes exist at a given k_y (using eigenvalue calculations), the growth rates of unstable modes, the eigenmode structures (the structure of the mode(s) along the field line), etc. Eventually, the fluctuating quantities will have sufficient amplitude that the nonlinear terms are no longer small relative to the linear terms. When this happens, linear growth ceases and the various fluctuating

quantities enter a quasi-stationary state, which will be shown in subsequent chapters. Mathematically, it is straightforward to see why the structure of the equations change as fluctuating quantities increase in amplitude and saturate. However, understanding the physical mechanism by which this process happens is not a straightforward task.

In hydrodynamic turbulence, as would be present in a turbulent river or the stirring of coffee, where the fluid is comprised of non-charged particles, one physical mechanism by which the system saturates is via a cascade of energy to smaller and smaller scales, where eventually small-scale dissipation like viscosity can dissipate the energy. This can be more easily understood through an example: the stirring of a large pot of water. The person mixing the water is injecting kinetic energy into the system, causing the water to swirl in a circular motion around the pot. When the stirring stops, the rate of rotation of the water in the pot will decrease, but, and this is where the transfer of energy to smaller scales happens, one will also see smaller circular structures known as eddies begin to form, and then even smaller eddies will form, and so on, until the water returns to rest. This is what is meant by a cascade of energy to smaller scales. The kinetic energy of the water at the beginning is in the largest length-scale of the system, namely whatever the diameter of the pot is, but over time, smaller eddies will continually form and slow down. The injected kinetic energy is cascading to eddies of smaller and smaller characteristic size until eventually friction or the little viscosity that

the water loses dissipates that energy. Now, in the case where the person never stops stirring, a balance will be struck between the energy injection rate and the energy dissipation rate, and the turbulent system will exist in saturated state.

However, this saturation mechanism is not always the whole story. There are a number of different mechanisms by which turbulence can saturate and dissipate energy. One mechanism that is particularly important for the present work is energy transfer to stable modes. Remembering the discussion of the drift-wave instability mechanism earlier in this chapter, that was a discussion of an unstable perturbation, or an unstable mode. In more complicated magnetic geometries, it is possible for both unstable and stable modes to coexist at similar wavenumbers. When this is the case, the nonlinearity of the system can preferentially move energy from an unstable mode to a stable mode at a similar wavenumber via three-wave coupling. This reduces the magnitude of the unstable mode amplitude while increasing the magnitude of the stable mode amplitude. By definition, the amplitude of a stable mode will decrease in time, as it puts energy back into the background gradients, again via the same drift-wave mechanism discussed earlier. Multiple saturation mechanisms coexist in most real-world turbulent systems, but as will be shown here, saturation via energy transfer to stable modes plays a significant role in both ITG and KBM turbulence in quasi-symmetric stellarator configurations. The next

chapter will discuss both the numerical methods and the GENE code used to study ITG and KBM turbulence in this work.

Citations

- [1] G.M. Weir, PhD Thesis, (2014).

- [2] Faber, B.J., Pueschel, M.J., Proll, J.H.E., Xanthopoulos, P., Terry, P.W., Hegna, C.C., Weir, G.M., Likin, K.M., & Talmadge, J.N. 2015 Gyrokinetic studies of trapped electron mode turbulence in the Helically Symmetric experiment stellarator. *Phys. Plasmas* **22** (7), 072305.

- [3] Guttenfelder, W., Anderson, D.T., Anderson, F.S.B., Canik, J.M., Likin, K.M., & Talmadge, J.N. 2009 Edge turbulence measurements in electron-heated Helically Symmetric Experiment plasmas. *Phys. Plasmas* **16** (8), 082508.

- [4] Mynick, H.E., Pomphrey, N., & Xanthopoulos, P. 2010 Optimizing stellarators for turbulent transport. *Phys. Rev. Lett.* **105** (9), 095004.

- [5] Xanthopoulos, P. & Jenko, F. 2007 Gyrokinetic analysis of linear microinstabilities for the stellarator Wendelstein 7-X. *Phys. Plasmas* **14** (4), 042501.

- [6] Xanthopoulos, P., Mynick, H.E., Helander, P., Turkin, Y., Plunk, G.G., Jenko, F., Görler, T., Told, D., Bird, T., & Proll, J.H.E. 2014 Controlling turbulence in present and future stellarators. *Phys. Rev. Lett.* **113** (15), 155011.
- [7] Horton, W. Jr, Choi, D.-I., & Tang, W.M. 1981 Toroidal drift modes driven by ion pressure gradients. *Phys. Fluids* **24** (6), 1077.
- [8] Rudakov, L.I. & Sagdeev, R.Z. 1961 On the instability of a nonuniform rarefied plasma in a strong magnetic field. *Dokl. Akad. Nauk SSR* **138** (3), 581-583.
- [9] Coppi, B. 1965 'Universal' instabilities for plasma moment equations. *Phys. Lett.* **14** (3), 172-174.
- [10] Coppi, B., Rosenbluth, M.N., & Sagdeev, R.Z. 1967 Instabilities due to temperature gradients in complex magnetic field configurations. *Phys. Fluids* **10** (3), 582.
- [11] Kadomtsev, B.B. & Pogutse, O.P. 1971 Trapped particles in toroidal magnetic systems. *Nucl. Fusion* **11**, 67-92.

- [12] Ishizawa, A., Imadera, K., Nakamura, Y., & Kishimoto, Y. 2019 Global gyrokinetic simulation of turbulence driven by kinetic ballooning mode. *Phys. Plasmas* **26**, 082301.
- [13] Dong, J.Q., Guzdar, P.N., & Lee, Y.C. 1987 Finite beta effects on ion temperature gradient driven modes. *Phys. Fluids* **30**, 2694-2702.
- [14] Aleynikova, K., Zocco, A., Xanthopoulos, P., Helander, P., & Nührenberg, C. 2018 Kinetic ballooning modes in tokamaks and stellarators. *J. Plasma Phys.* **84**, 745840602.
- [15] Grulke, O. & Klinger, T. 2002 Large-scale fluctuation structures in plasma turbulence. *New J. Phys.* **4**, 67.1-67.23.
- [16] Mahmood, M.A., Rafiq, T., & Persson, M. 2006 Unstable ion-temperature-gradient modes in an advanced tokamak plasma. *Plasma Phys. Control. Fusion* **48**, 1019.
- [17] Horton, W. 1999 Drift waves and transport. *Rev. Mod. Phys.* **71**, 735.
- [18] Pueschel, M.J. and Jenko, F. 2010 Transport properties of finite- β microturbulence. *Phys. Plasmas* **17**, 062307.

- [19] Pueschel, M.J., Kammerer, M., and Jenko, F. 2008 Gyrokinetic turbulence simulations at high plasma beta. *Phys. Plasmas* **15**, 102310.
- [20] Snyder, P.B. 1999 Gyrofluid Theory and Simulation of Electromagnetic Turbulence and Transport in Tokamak Plasmas. PhD Thesis.
- [21] Snyder P.B., Hammett G.W., Beer M.A., and Dorland, W. 1999 Simulations of Electromagnetic Turbulence and Transport in Tokamak Plasmas. *Proc. 26th EPS Conf. on Contr. Fusion and Plasmas Physics*, ECA 23J, 1685.
- [22] Aleynikova, K. and Zocco, A. 2017 Quantitative study of kinetic ballooning mode theory in simple geometry. *Phys. Plasmas* **24**, 092106.
- [23] Kotschenreuther, M. 1986 Compressibility effects on ideal and kinetic ballooning modes and elimination of finite Larmor radius stabilization. *Phys. Fluids* **29** (9), 2898-2913.
- [24] Hirose, A. and Elia, M. 1996 Kinetic Ballooning Mode with Negative Shear. *Phys. Rev. Lett* **76** (4), 628.

[25] Hirose, A., Zhang, L., and Elia, M. 1995 Ion temperature gradient-driven ballooning mode in tokamaks. *Phys. Plasmas* **2**, 859.

[26] Aleynikova, K., Zocco, A., Xanthopoulos, P., Helander, P., and Nührenberg, C. 2018 Kinetic ballooning modes in tokamaks and stellarators. *J. Plasma Phys.* **84**, 745840602.

Chapter 3

Gyrokinetics

The purpose of this chapter is to introduce both gyrokinetics and the GENE code used to conduct the numerical studies presented in this dissertation. The previous chapter introduced some of the challenges underlying developing a comprehensive understanding of plasma turbulence, and this chapter discusses some of the clever methods used to approach the problem of plasma turbulence in a pragmatic way, especially within the context of current supercomputing technology. The basic strategy for developing practical tools to understand plasma turbulence, most of the time, is to determine what pieces of physics are ignorable and what must be kept in order to accurately study the physics of interest. For example, if one is interested in strictly ITG turbulence, it may be possible to make certain assumptions about the electron dynamics, reducing the complexity of the system, and thereby making your problem more tractable.

3.1 The Vlasov equation

In an ideal world, where there is infinite computing power, one could simulate the trajectories of motion of every single plasma particle in your system and determine the electromagnetic fields for all points in space at all times. The system of equations for this case look like the following. First, one would begin with a plasma particle density function describing the distribution of plasma particles, shown in Eq. 3.1.

$$N(\mathbf{x}, \mathbf{v}, t) = \sum_{i=1}^{N_{0,s}} \delta(\mathbf{x} - \mathbf{x}_i(t)) \delta(\mathbf{v} - \mathbf{v}_i(t)), \quad (3.1)$$

where \mathbf{x}_i , \mathbf{v}_i , $N_{0,s}$, and $\delta(x)$ denote the position of a plasma particle, the velocity of a plasma particle, the number of particles of a given species, and a Dirac delta function, respectively. As a brief aside, the Dirac delta function has the quality of being equal to zero except when its argument is zero. When its argument is zero, the Dirac delta function takes on an infinite value such that $\int f(x) \delta(x - a) dx = f(a)$. Next, each plasma particle moves in $6D$ phase space (where the six coordinates are the familiar Cartesian coordinates and their corresponding velocities: (x, y, z, v_x, v_y, v_z)) according to the Lorentz force discussed in Ch. 1, shown again here in Eq. 3.2.

$$m_s \frac{\partial \mathbf{v}_i(t)}{\partial t} = q_s \left(\mathbf{E}(\mathbf{x}_i(t), t) + \mathbf{v}_i(t) \times \mathbf{B}(\mathbf{x}_i(t), t) \right), \quad (3.2)$$

where the location and velocity of each plasma particle i have been substituted for the general spatial and velocity-space coordinates. Next, the electric

and magnetic fields change as the particles move in phase space according to Maxwell's equations, shown again below.

$$\nabla \cdot \mathbf{E}(\mathbf{x}, t) = \frac{\rho(\mathbf{x}, t)}{\epsilon_0} \quad (3.3)$$

$$\nabla \cdot \mathbf{B}(\mathbf{x}, t) = 0 \quad (3.4)$$

$$\nabla \times \mathbf{E}(\mathbf{x}, t) = -\frac{\partial \mathbf{B}(\mathbf{x}, t)}{\partial t} \quad (3.5)$$

$$\nabla \times \mathbf{B}(\mathbf{x}, t) = \mu_0 \left(\mathbf{J}(\mathbf{x}, t) + \epsilon_0 \frac{\partial \mathbf{E}(\mathbf{x}, t)}{\partial t} \right), \quad (3.6)$$

where the current density and charge density are defined relative to the plasma particle density function in the following way:

$$\begin{aligned} \rho(\mathbf{x}, t) &= \sum_s^{N_{\text{species}}} q_s \int d^3v \sum_{i=1}^{N_{0,s}} \delta(\mathbf{x} - \mathbf{x}_i(t)) \delta(\mathbf{v} - \mathbf{v}_i(t)) = \sum_s^{N_{\text{species}}} q_s \int d^3v N \\ \mathbf{J}(\mathbf{x}, t) &= \sum_s^{N_{\text{species}}} q_s \int d^3v \mathbf{v} \sum_{i=1}^{N_{0,s}} \delta(\mathbf{x} - \mathbf{x}_i(t)) \delta(\mathbf{v} - \mathbf{v}_i(t)) = \sum_s^{N_{\text{species}}} q_s \int d^3v \mathbf{v} N. \end{aligned}$$

One can then determine the time evolution of the plasma particles by evaluating Eq. 3.7 below:

$$\frac{\partial N}{\partial t} = \frac{\partial}{\partial t} \sum_{i=1}^{N_{0,s}} \delta(\mathbf{x} - \mathbf{x}_i(t)) \delta(\mathbf{v} - \mathbf{v}_i(t)) = 0, \quad (3.7)$$

which, after making use of a number of Dirac delta function properties gives the following equation of motion, Eq. 3.8:

$$\frac{\partial N}{\partial t} + \mathbf{v} \cdot \nabla N + \frac{q_s}{m_s} (\mathbf{E}(\mathbf{x}, t) + \mathbf{v} \times \mathbf{B}(\mathbf{x}, t)) \cdot \nabla_{\mathbf{v}} N = 0. \quad (3.8)$$

Eq. 3.8 is known as the Klimontovich equation and it is well known in plasma kinetic theory. However, in the present form, it is not useful for plasma turbulence simulations. This is because nominal fusion-energy-relevant plasmas contain on the order of $N_{\text{tot}} = 10^{22}$ - 10^{23} plasma particles. Therefore, at each time step, one would need to calculate the electric and magnetic fields at each $(\mathbf{x}_i, \mathbf{v}_i)$ as the superposition of the contributions to \mathbf{E} and \mathbf{B} from all other plasma particles at positions $(\mathbf{x}_j, \mathbf{v}_j)$, where $i \neq j$. Based on this fact, it would require at least on the order of N_{tot}^2 calculations at each time step, and this is simply not feasible given current supercomputing technology. However, not all is lost because the Klimontovich equation is a starting point for the derivation of the Vlasov equation, first introduced in the previous chapter, which can be used for practically-relevant plasma turbulence calculations.

Beginning with the ensemble average of Eq. 3.8 and taking $f(\mathbf{x}, \mathbf{v}, t)$, $\mathbf{E}^*(\mathbf{x}, \mathbf{v}, t)$, and $\mathbf{B}^*(\mathbf{x}, t)$ to be the ensemble averages of N , $\mathbf{E}(\mathbf{x}, t)$, and $\mathbf{B}(\mathbf{x}, t)$, respectively, with $\langle \rangle$ denoting the ensemble average, one arrives at:

$$\left\langle \frac{\partial N}{\partial t} + \mathbf{v} \cdot \nabla N + \frac{q_s}{m_s} (\mathbf{E}(\mathbf{x}, t) + \mathbf{v} \times \mathbf{B}(\mathbf{x}, t)) \cdot \nabla_{\mathbf{v}} N \right\rangle = 0, \quad (3.9)$$

$$\frac{\partial \langle N \rangle}{\partial t} + \mathbf{v} \cdot \nabla \langle N \rangle + \left\langle \frac{q_s}{m_s} (\mathbf{E}(\mathbf{x}, t) + \mathbf{v} \times \mathbf{B}(\mathbf{x}, t)) \cdot \nabla_{\mathbf{v}} N \right\rangle = 0, \quad (3.10)$$

which finally simplifies to the Vlasov equation:

$$\frac{\partial f}{\partial t} + \mathbf{v} \cdot \nabla f + \frac{q_s}{m_s} (\mathbf{E}^*(\mathbf{x}, t) + \mathbf{v} \times \mathbf{B}^*(\mathbf{x}, t)) \cdot \nabla_{\mathbf{v}} f = 0, \quad (3.11)$$

where higher-order correlations between \mathbf{E} , \mathbf{B} , and N that would be present due to the third term in Eq. 3.10 are ignored because the turbulence results presented in this work are in the collisionless regime, and so the Vlasov equation is used rather than the Boltzmann equation. A similar ensemble averaging is done for Maxwell's equations. It is this set of Maxwell's equations, coupled with the Vlasov equation, that is used in the GENE code, and therefore for the turbulence calculations presented in this dissertation.

3.2 The Gene Code

In this work, the gyrokinetic turbulence code GENE [1] is used to study ITG and KBM turbulence via flux-tube simulations of the NCSX, HSX, H-J, and small- \hat{s} circular tokamak magnetic equilibria outlined in Ch. 1. Relative to fully kinetic simulations, where the full particle trajectories are resolved, gyrokinetics reduces computational expense by averaging over the gyrophase of the trajectories of charged particles in the presence of a strong magnetic guide field [2], thereby simulating rings of charge, as is shown in Fig. 3.1. This provides two major advantages which make numerical simulation of plasma turbulence feasible with current supercomputing technology. The first advantage is that the fast time-scale associated with the gyromotion of charged particles does not need to be resolved, and this is acceptable because the physics of interest occurs on time-scales that are much slower than the gyromotion (generally by at least three orders of magnitude). The second advantage is

that the dimensionality of the phase space of the system is reduced from six to five, that is, gyrokinetics reduces the $6D$ phase space (x, y, z, v_x, v_y, v_z) to a $5D$ phase space (x, y, z, v_\perp, v_z) . This reduces the number of degrees of freedom in the system, thereby reducing the necessary computing resources. GENE solves a system of coupled equations that consists of the Vlasov equation, the Poisson equation, and Ampere's law (in simulations with finite β). Further details regarding the equations solved by GENE can be found in Pueschel et al., 2011 [3].

Using the MHD magnetic equilibrium solver VMEC [4] to generate the HSX, NCSX, H-J, and small- \hat{s} tokamak geometries, the GIST code [5] then calculates the necessary magnetic geometry data for the desired flux tube at the specified normalized toroidal magnetic flux $s_0 = \Psi/\Psi(a) = (r_{\text{eff}}/a)^2$, where $\Psi(a)$ is the toroidal flux at the plasma boundary and r_{eff} is an effective radial coordinate implicitly defined by the toroidal magnetic flux.

3.2.1 Flux-tube simulation domain

Due to the computational expense of full-volume and full-flux-surface simulations [6], flux-tube simulations are exclusively employed in this work. The characteristic perpendicular length scales of the turbulence in magnetic confinement systems are sufficiently small that flux-tube simulations with reduced radial extent will accurately capture the dynamics of the turbulence. In the localized flux-tube simulation domain, periodic and quasi-periodic boundary conditions are used in the radial/binormal and parallel directions, respectively.

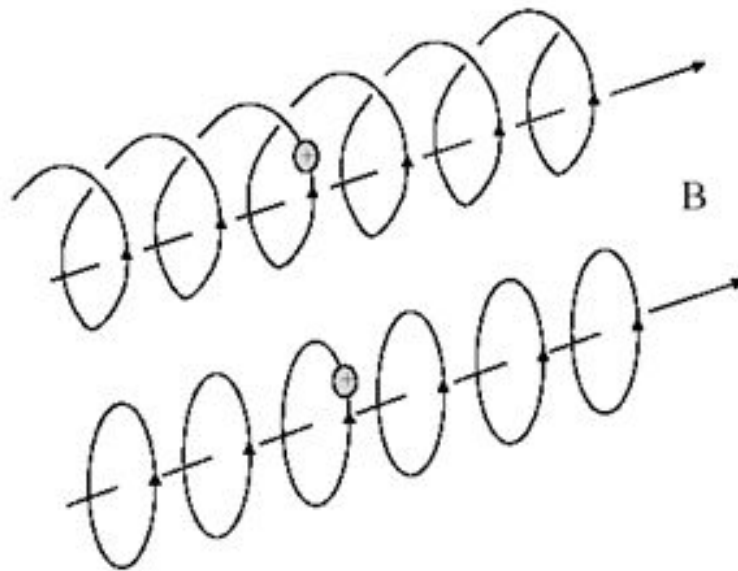


Figure 3.1: This figure highlights the gyroaveraging done in gyrokinetic codes such as `GENE` code where, rather than resolving the gyromotion of charged particles in strong magnetic fields, one can average over the gyrophase and simulate charged rings. This is valid because the characteristic time-scales of plasma turbulence are much slower than the time-scale associated with gyromotion. Source: Noguchi, 2016.

A flux tube follows a single magnetic field line around the equilibrium with sufficient radial extent to encompass multiple perpendicular turbulent correlation lengths. This requirement prevents artificial self-connection of turbulent fluctuations via the periodic radial boundary condition. Care must be taken to ensure that the flux tube extent along the field line is sufficient so that any given eigenmode is localized and accurately described [6]. In Figure 3.2, examples of $n_{\text{pol}} = 2$ flux-tube domains for HSX and NCSX are shown, where n_{pol} indicates the number of poloidal transits of the flux tube. The low average magnetic shear in HSX, which affects how extended eigenmodes can be in the parallel direction, impacts the convergence characteristics as measured by n_{pol} . Prior gyrokinetic studies of HSX flux tubes indicate $n_{\text{pol}} = 4$ is required for proper convergence [7].

The coordinate system used in GENE is the following. The direction parallel to the background magnetic field is the \hat{z} direction. The radial direction \hat{x} is perpendicular to both \hat{z} and the magnetic flux surface on which the turbulence simulations are carried out. The final spatial coordinate is the \hat{y} direction, which is called the binormal direction because it is a second vector (in addition to \hat{x}) which is perpendicular to the magnetic field line. In general, \hat{x} and \hat{y} are *not* perpendicular in complex three-dimensional magnetic geometries, which makes the math more complicated than would be the case in orthogonal coordinate systems. GENE is spectral in both the \hat{x} and \hat{y} directions while using real-space coordinates for \hat{z} .

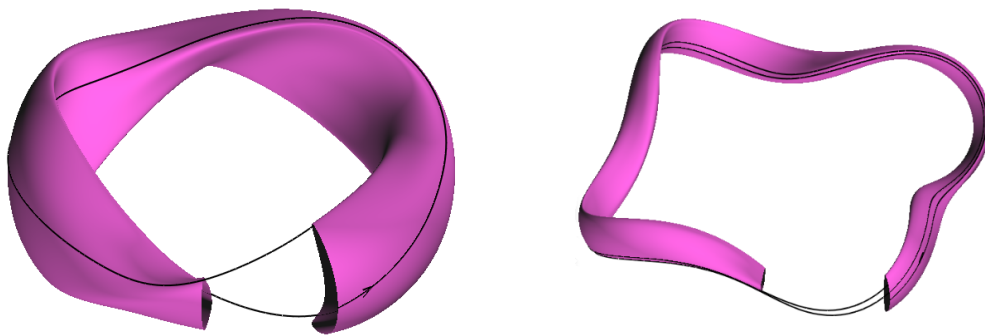


Figure 3.2: The $s_0 \approx 0.5$ flux surfaces of NCSX (left) and HSX (right). The black lines indicate the $\alpha = \theta - t\xi = 0$ flux-tube domains of each configuration, where θ and ξ are the poloidal and toroidal angle in Boozer coordinates, respectively. Figure courtesy of Pavlos Xanthopoulos.

In the HSX geometry, the value of the rotational transform $\iota = d\Phi_p/d\Psi = 1/q \approx 1.062$ at $s_0 \approx 0.5$ is near unity, where Φ_p and q are the poloidal magnetic flux and the safety factor, respectively. Contrastingly, NCSX has $\iota \approx 0.559$ at $s_0 = 0.5$. As a result of the near unity value of ι in the HSX geometry, a flux tube in the HSX configuration will require greater n_{pol} to sample more unique portions of the flux surface geometry relative to a flux tube in the NCSX configuration. The following chapters will present the major ITG and KBM turbulence results that comprise the bulk of this work.

Citations

- [1] Jenko, F. 2000 Massively parallel Vlasov simulation of electromagnetic drift-wave turbulence. *Comput. Phys. Commun.* **125**, 196-209.
- [2] Brizard, A.J. & Hahm, T.S. 2007 Foundations of nonlinear gyrokinetic theory. *Rev. Mod. Phys.* **79** (2), 421-468.
- [3] Pueschel, M.J., Jenko, F., Told, D., & Buchner, J. 2011 Gyrokinetic simulations of magnetic reconnection. *Phys. Plasmas* **18** (11), 112102.
- [4] Xanthopoulos, P., Cooper, W.A., Jenko, F., Turkin, Y., Runov, A., & Geiger, J. 2009 A geometry interface for gyrokinetic microturbulence investigations in toroidal configurations. *Phys. Plasmas* **16** (8), 082303.

- [5] Hirshman, S.P., Van Rij, W.I., & Merkel, P. 1986 Three-dimensional free boundary calculations using a spectral Green's function method. *Comput. Phys. commun.* **43** (1), 143–155.
- [6] Monreal, P., Sánchez, E., Calvo, I., Bustos, A., Parra, F. I., Mishchenko, A., Konies, A., & Kleiber, R. 2017 Semianalytical calculation of the zonal-flow oscillation frequency in stellarators. *Plasma Phys. Control. Fusion* **59** (6), 065005.
- [7] Faber, B.J., Pueschel, M.J., Terry, P.W., Hegna, C.C., & Roman, J.E. 2018 Stellarator microinstabilities and turbulence at low magnetic shear. *J. Plasma Phys.* **84** (5), 905840503.

Chapter 4

Electrostatic ITG turbulence in stellarators

In this chapter, a comparison of as-calculated-by-GENE ITG turbulence properties of both HSX and NCSX in the electrostatic limit (both adiabatic and kinetic electrons) will be presented. These results have been published [1], and this chapter serves to cover the contents of that publication. This chapter also serves to introduce the reader to a variety of methods such as eigenvalue calculations, quasilinear modeling, fluctuation cross-phases, and nonlinear frequency analysis techniques used in gyrokinetics to diagnose both linear and nonlinear dynamics. The primary takeaway of this chapter is that purely linear dynamics such as growth rates or quasilinear estimates fail to capture some important aspects of turbulent transport across quasi-symmetric stellarator equilibria, an indication that an understanding of nonlinear physics is necessary.

4.1 Adiabatic-electron turbulence

The first ITG turbulence comparison in this chapter is based on adiabatic electrons, where electrons are assumed to have an immediate response to a

fluctuating electrostatic potential Φ ($e\Phi/T_{e0} = n_e/n_{e0}$), where e , T_{e0} , n_e , and n_{e0} are the elementary charge, equilibrium electron temperature, fluctuating electron density, and equilibrium electron density, respectively. The rationale for this is twofold. First, past work on stellarator turbulence has focused on the adiabatic-electron limit [2-5], owing to the lower computational costs. Second, by first analyzing the adiabatic-electron limit, it is possible to determine whether certain aspects of the ITG dynamics persist when simulating with kinetic electrons or not. Results pertaining to linear computations in the adiabatic-electron limit will be presented next, followed by nonlinear results.

4.1.1 Linear eigenmodes

The linearized versions of Vlasov equation, Poisson equation, and Ampère's Law, see Eqs. (2.13)-(2.17), are solved using a normal eigenmode ansatz such that fluctuating quantities are assumed to evolve as $\Phi, n \propto \exp[i(\mathbf{k}_\perp \cdot \mathbf{x} - \omega t)]$, where $\omega = i\gamma - \omega_r$ such that a positive real frequency indicates a mode propagating in the ion diamagnetic direction.

Linear initial-value computations determine the most unstable eigenmode of the system. Figure 4.1 shows the dominant growth rate γ at each wavenumber k_y , normalized to the inverse ion sound gyroradius $\rho_s = c_s m_i / (eB)$, where k_x and k_y are the radial and binormal wavenumbers, respectively. In Fig. 4.1, the transport-relevant regime is the low- k_y region, as it is the large-wavelength structures that dominate the heat flux, as will be shown in Sec. 4.1.6. Note the continuity in the real frequency ω spectrum, an indication that only a

single ITG branch is dominant. However, as will be shown, subdominant modes exist in both HSX and NCSX. The normalized gradient values used for all simulations with adiabatic electrons are $a/L_n = 0$ and $a/L_{Ti} = 3$, where $L_{n,T}^{-1} \equiv -[1/(n_0, T_0)] d(n_0, T_0)/dr$.

As previously mentioned, this chapter contrasts both linear and nonlinear ITG physics between NCSX and HSX. One of the primary conclusions of this chapter is the following: the NCSX configuration exhibits lower growth rates in the low- k_y regime, suggesting that NCSX should display more favorable behavior with respect to ITG turbulent transport, i.e., a lower electrostatic ion heat flux Q_i^{es} in nonlinear simulations. However, as will be shown, HSX exhibits smaller Q_i^{es} relative to NCSX. The fact that HSX exhibits larger growth rates is intuitive after one examines the magnetic shear and curvature. First, the local magnetic shear, a stabilization mechanism for drift waves, is an order of magnitude smaller on average in magnitude in HSX compared to NCSX. Second, the curvature at the outboard midplane, where modes tend to be localized, is worse in HSX than NCSX. It should be noted that $a \approx 0.33$ m and $a \approx 0.12$ m for NCSX and HSX, respectively. Therefore, there is as much as a factor of 8 difference (at $k_y \rho_s = 0.2$) in linear growth rates when expressed in Hz between HSX and NCSX. This result is consistent with calculations made by Rewoldt et al. [5], where there is roughly a factor of 7 difference in growth rates between HSX and NCSX-BETA. Next, additional differences in the linear ITG drift-wave physics between NCSX and HSX will be elucidated, including

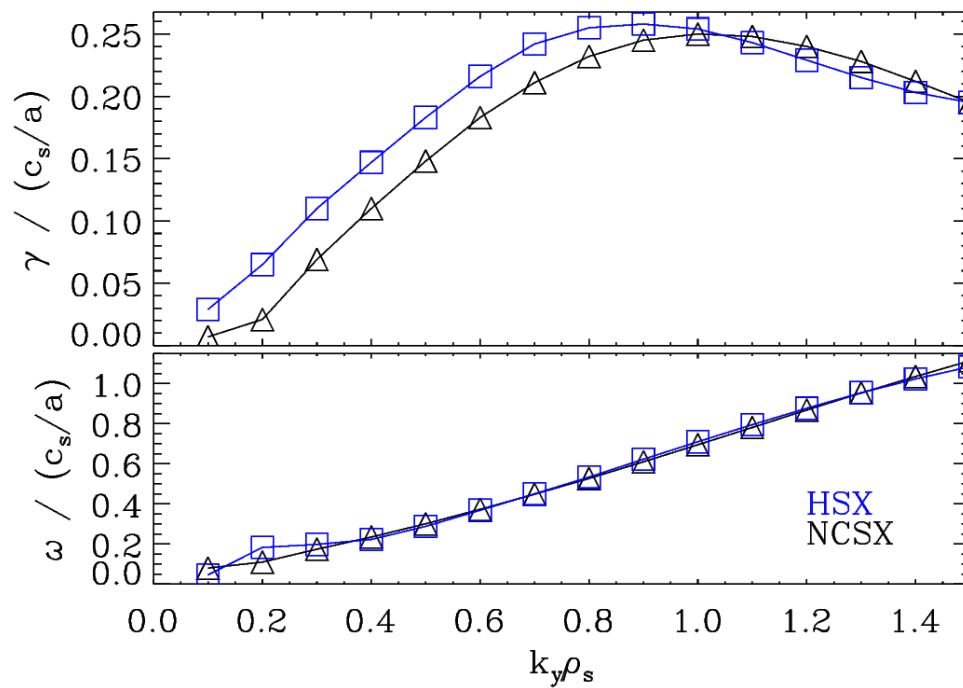


Figure 4.1: The dominant linear growth rate γ (top) and real frequency ω (bottom) as a function of normalized binormal wavenumber k_y for the NCSX (black triangles) and HSX (blue squares) configurations for the $\alpha = 0$ flux tubes.

results pertaining to subdominant mode behavior, eigenmode structure, and quasilinear estimates in HSX vs. NCSX.

4.1.2 Subdominant mode landscape

Figure 4.2 shows the frequencies and growth rates of 123 and 47 linear eigenmodes for HSX and NCSX, respectively, at $k_y \rho_s = 0.3$. At this wavenumber, there are at least 109 and 5 linearly unstable modes in HSX and NCSX, respectively. Subdominant modes are eigenmodes of the linear operator of the system that have smaller positive growth rates than the dominant instability. It is also important to note that the modes in Fig. 4.2 likely do not encompass all of the fastest-growing or slowest-decaying modes, as the eigenvalue solver algorithm can miss modes occasionally due to its iterative nature; but, the modes that the eigenvalue solver misses tend to be very close to marginality ($\gamma \approx 0$). However, the general picture that HSX has many more unstable modes than NCSX depicted in Fig. 4.2 is nevertheless accurate. The larger number of unstable modes in HSX relative to NCSX is characteristic of the subdominant-mode landscape at other values of k_y in the low- k_y range.

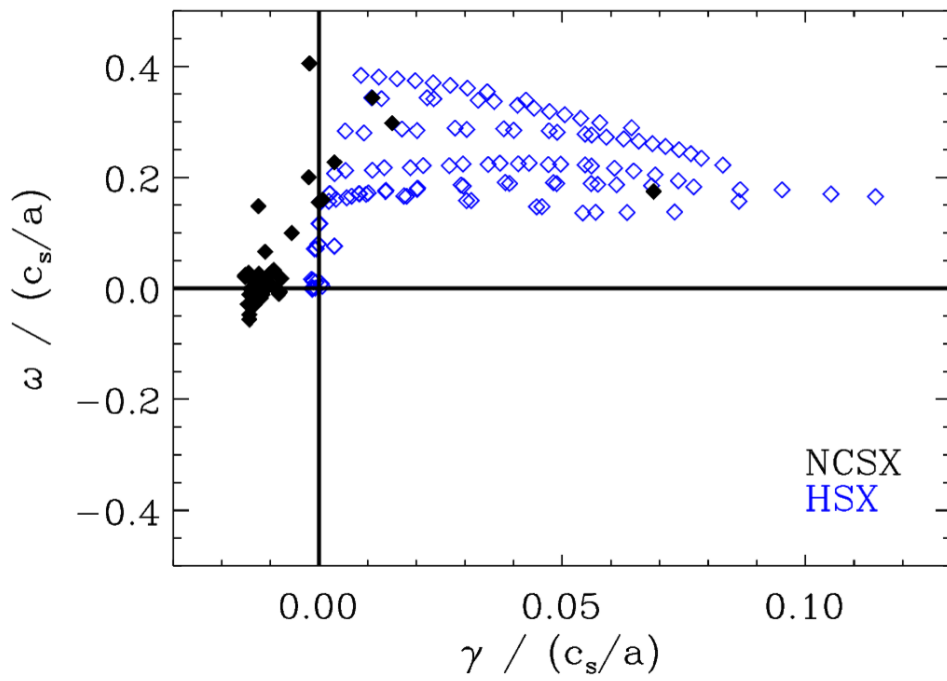


Figure 4.2: A set of 123 and 47 linear eigenmodes in HSX (blue hollow diamonds) and NCSX (black filled diamonds), respectively, at binormal wavenumber $k_y \rho_s = 0.3$ for computations with adiabatic electrons, as determined by GENE's iterative eigenvalue solver. Note the substantial number of subdominant modes in HSX relative to the few in NCSX.

The motivation for showing data at $k_y \rho_s = 0.3$ is that this value of k_y is near the peak of the ion heat flux spectrum in Fig. 4.5 for HSX. The large difference between the subdominant eigenmode landscapes of HSX and NCSX is due in large part to the dissimilar average magnetic shear \hat{s} in each configuration. Generally, larger \hat{s} more effectively localizes a given eigenmode to the bad-curvature region. Since \hat{s} is small in HSX, modes are more sensitive to portions of the magnetic geometry further away from the outboard midplane where the local magnetic shear has a small amplitude. With more regions along the magnetic field line available to these eigenmodes due to small \hat{s} , HSX exhibits substantially more subdominant modes than NCSX; see also Refs. [6,7]. For low magnetic shear, mode localization at different k_x is possible, resulting in many concurrently unstable mode branches. One might expect this to bode poorly for turbulent transport in HSX relative to NCSX, especially since there are a number of subdominant modes in HSX that are more unstable than the dominant instability present in NCSX. It is noteworthy that eigenvalue computations of HSX with an artificial, NCSX-like $\hat{s} \approx -0.5$ display only a handful of subdominant modes, indicating that \hat{s} , or more precisely the local magnetic shear, is indeed the primary factor determining subdominant-mode excitation. The existence of a larger number of unstable modes seems unfavorable with respect to turbulent transport properties; however, this may not necessarily be the case. In a tokamak, the most unstable mode at a given k_y can describe upwards of 70% of the turbulent state [8], while in a geometry

like HSX, all of the unstable modes combined may only constitute 60% of the nonlinear state [7]. This is consistent with the fact that quasilinear proxies can work to predict and optimize ITG turbulent transport over a range of quasi-axisymmetric stellarators, as they are tokamak-like [3], where the most unstable mode can be a better proxy for the turbulent state.

4.1.3 Eigenmode structure

In HSX, eigenmodes at long binormal wavelengths extend far along the magnetic field line. This differs from the ITG eigenmode structures present in NCSX, where eigenmodes are more strongly localized to the bad-curvature region of a given field line, generally at the outboard midplanes. Figure 4.3 highlights this difference between NCSX and HSX, showing the electrostatic potential Φ structure of the dominant eigenmode at wavenumber $k_y \rho_s = 0.2$.

HSX exhibits extended eigenmodes structures versus the more-localized modes in NCSX, and this can have important implications for the energetics of the turbulent state. The structure of eigenmodes plays an important role in determining the effectiveness of nonlinear energy transfer from unstable to damped eigenmodes in turbulence saturation physics [9,10]. In a configuration like HSX, where eigenmodes are more extended along the field line and thus retain substantial amplitudes across a wide range of radial wavenumbers k_x that may interact nonlinearly, the nonlinear coupling between eigenmodes and therefore the nonlinear transfer of energy to stable modes may be more efficient [2], allowing for lower saturated heat flux levels.

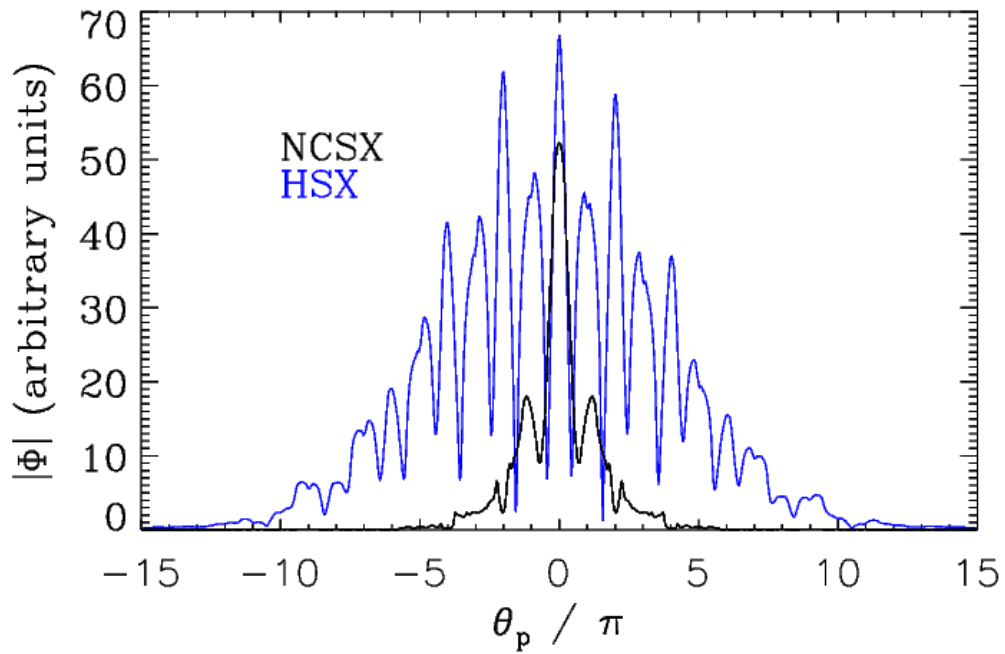


Figure 4.3: Eigenmode amplitude as a function of parallel coordinate along the field line for binormal wavenumber $k_y \rho_s = 0.2$ for the baseline NCSX configuration (black) and the HSX geometry (blue) for computations with adiabatic electrons. Note the extended nature of the HSX eigenmode relative to NCSX.

4.1.4 Quasilinear transport modeling

A quasilinear comparison of HSX and NCSX can provide insight into the extent to which the linear physics accurately captures the performance of HSX relative to NCSX with respect to ITG turbulence. The goal of this quasilinear analysis is to see if the conclusion of the comparison of dominant linear growth rates between configurations is changed by accounting for all of the subdominant modes at each k_y , the impact of individual mode widths, and quasilinear weight changes. Here a quasilinear transport model will be used to extend the comparison of dominant linear growth rates between HSX and NCSX to include additional linear physics and some data from nonlinear simulations to ensure proper spectral shapes. To achieve this, a mixing-length argument is employed to estimate the quasilinear turbulent thermal diffusivity as [7]

$$\chi_i^{\text{QL}} = \sum_{k,j} S_k \frac{w_{k,j} \gamma_{k,j}}{\langle k_{\perp}^2 \rangle}, \quad (4.1)$$

where

$$\langle k_{\perp}^2 \rangle = \langle g^{xx} k_x^2 + 2g^{xy} k_x k_y + g^{yy} k_y^2 \rangle, \quad (4.2)$$

with the field-line average defined as $\langle X \rangle = \int d\theta X |\Phi|^2 / \int d\theta |\Phi|^2$, where \mathbf{k}_{\perp} is the perpendicular wavevector of a given mode, Φ is the electrostatic potential, and θ labels points along a field line assuming a ballooning-like ansatz for the micro-instability [11,12]. The k and j sums are over wavenumbers k_y and the unstable eigenmodes, respectively, and $\gamma_{k,j}$ is the growth rate of a particular

mode. The shaping factor S_k is determined by the heat flux spectrum of a reference nonlinear simulation. More specifically, S_k is the fraction of the heat flux associated with a specific k_y from a reference nonlinear simulation. For both HSX and NCSX, the reference nonlinear simulations are the simulations from which the time traces in Fig. 4.4 are generated. The quasilinear weight $w_{k,j} = Q_i/n^2$, where Q_i and n are the volume-integrated ion heat flux and fluctuating ion density associated with a given linear eigenmode, respectively, is a weighting factor which accounts for the phase information of the eigenmode in question, quantifying the extent to which it can produce heat flux. The use of n^2 in the quasilinear weight is justified since these are adiabatic-electron simulations ($n \propto \Phi$); for kinetic-electron simulations, Φ^2 is the more appropriate normalization choice [13]. In performing this calculation, the subdominant instabilities at each k_y are accounted for, but stable modes are not. Both S_k and $w_{k,j}$ are comparable between the two configurations, with $w_{k,j}$ being approximately 40% larger on average in HSX. The most notable difference, besides the number of subdominant modes, between HSX and NCSX with respect to this quasilinear calculation is $\langle k_{\perp k,j}^2 \rangle$, with HSX exhibiting smaller $\langle k_{\perp k,j}^2 \rangle$, and therefore larger $\langle k_{\perp k,j}^2 \rangle^{-1}$, than NCSX by roughly an order of magnitude or more, depending on the value of k_y .

A comparison of the quasilinear turbulent thermal diffusivity of HSX and NCSX yields: $(\chi_i^{\text{QL}})^{\text{HSX}}/(\chi_i^{\text{QL}})^{\text{NCSX}} \approx 4.2$. This is consistent with an intuitive interpretation of the dominant linear growth rates, as, at low k_y , HSX

growth rates are larger than their NCSX counterparts by roughly a factor of 3. Thus, based on linear considerations alone, one would expect that HSX produces larger heat fluxes than NCSX even after accounting for all subdominant modes. As shown in the following section, the quasilinear estimate shown here is inconsistent with nonlinear simulation results.

4.1.5 Nonlinear dynamics

Nonlinear simulations for both HSX and NCSX were performed. Time traces of nonlinear heat flux in gyro-Bohm units for ITG turbulence are presented in Fig. 4.4. The average ion heat flux is lower in HSX compared to NCSX by nearly a factor of three, a result that is counter-intuitive given that NCSX has lower linear growth rates and associated quasilinear estimates for ITG transport. This indicates both that the ITG turbulence saturation physics is quantitatively different between HSX and NCSX and that standard quasilinear models can not always be expected to provide good proxies for comparing ITG turbulent transport between sufficiently different quasi-symmetric magnetic configurations.

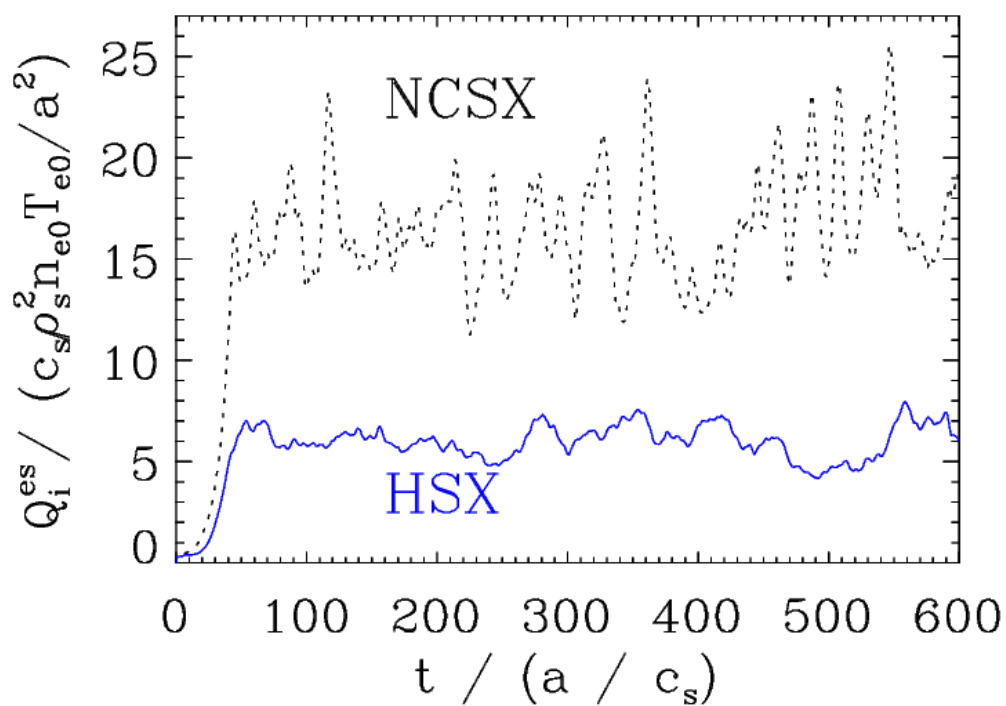


Figure 4.4: Normalized heat flux time traces for HSX (blue solid line) and NCSX (black dotted line) with adiabatic electrons. The heat flux is approximately 17 and 6 in gyro-Bohm units for NCSX and HSX, respectively, averaged over the quasi-stationary state.

With the goal of investigating differences in the nonlinear ITG turbulence dynamics between configurations, which could provide insight regarding the mismatch between quasilinear theory and nonlinear gyrokinetic calculations of Q_1^{es} , various aspects of the nonlinear state such as heat flux spectra, cross-phases, and nonlinear frequencies are examined in subsequent sections.

4.1.6 Heat flux spectra

Nonlinear heat flux spectra illustrate which values of k_y contribute to the heat transport in the quasi-stationary state. Figure 4.5 shows the heat flux spectra for both NCSX and HSX. The HSX heat flux spectrum peaks at smaller k_y than the NCSX heat flux spectrum, thus larger-wavelength fluctuations are responsible for a greater fraction of the turbulent heat transport in HSX relative to NCSX, where somewhat smaller structures dominate the transport. Both spectra exhibit peaks that are below the peak in linear growth rate γ observed in Fig. 4.1, a nonlinear downshift that is consistent with behavior seen in tokamak simulations [14]. Given that the two spectra are comparable in shape, it is difficult to draw a conclusion from these data to explain the difference in the nonlinear heat flux difference between HSX and NCSX.

4.1.7 Cross-phases

Here, an analysis of the nonlinear cross-phase α between the electrostatic potential Φ and the total perturbed ion temperature $T_i^{\text{tot}} = (2T_{i\perp} + T_{i\parallel})/3$ is presented. The relative phase of these two quantities affects the efficiency of

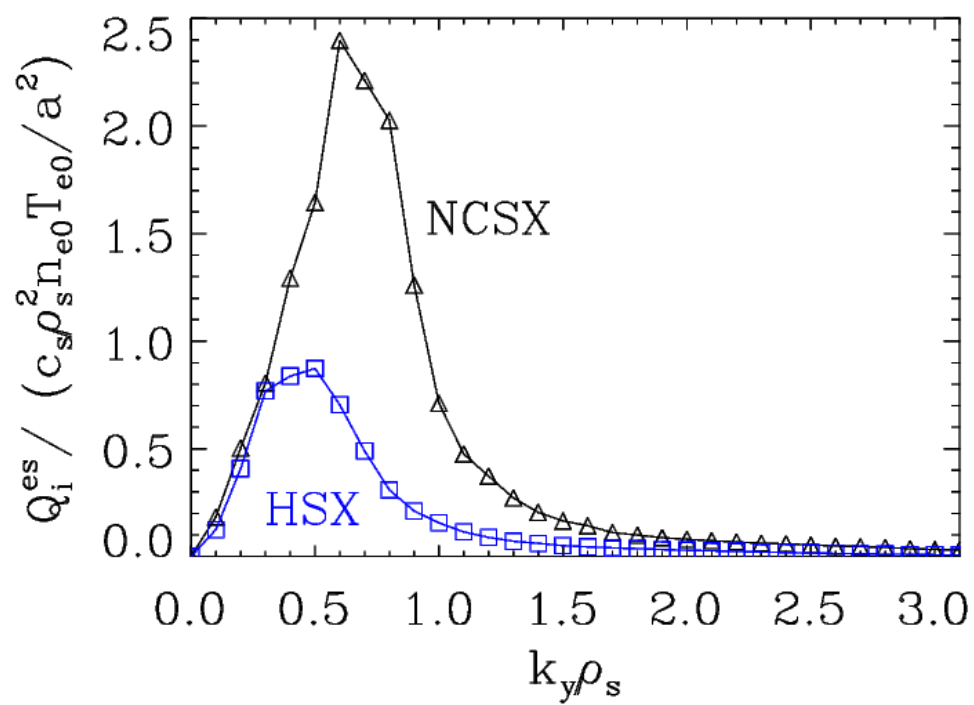


Figure 4.5: The heat flux spectra for HSX (blue squares) and NCSX (black triangles) from nonlinear simulations with adiabatic electrons.

the ITG drive as well as that of the $E \times B$ flux. What is meant by efficiency here is that the physical mechanism which drives outward ITG transport relies on the cross-phase of Φ and T_i^{tot} fluctuations being between 0 and π , and the degree to which the fluctuations are out of phase determines how efficiently the instability reinforces itself, with maximal efficiency occurring at $\pi/2$. Therefore, maximal outward energy transport typically occurs when the cross-phase between Φ and T_i^{tot} is close to $\pi/2$ and decreases as the phase difference approaches 0 or π . Negative cross-phases are associated with inward transport and the stable branch of the linear ITG mode. The linear color scale in Fig. 4.6 represents a probability distribution function integrating to 1 at each k_y separately, which provides information on what fraction of grid points and Fourier modes in the nonlinear system exhibits a cross-phase that lies in a small interval about a given α . Figure 4.6 shows the cross-phases for both HSX and NCSX. The color scale for the nonlinear cross-phases is linear. Red indicates regions where there is a higher likelihood that a given mode will exhibit a particular value of the cross-phase.

Clearly, both configurations exhibit very similar phase characteristics, both in terms of the dominant linear eigenmode and the turbulence. It is worth noting that the difference between the peak in the nonlinear data and the dominant linear eigenmode is larger in HSX relative to NCSX at $k_y \rho_s < 0.6$. It is important to highlight that this linear-nonlinear-cross-phase difference

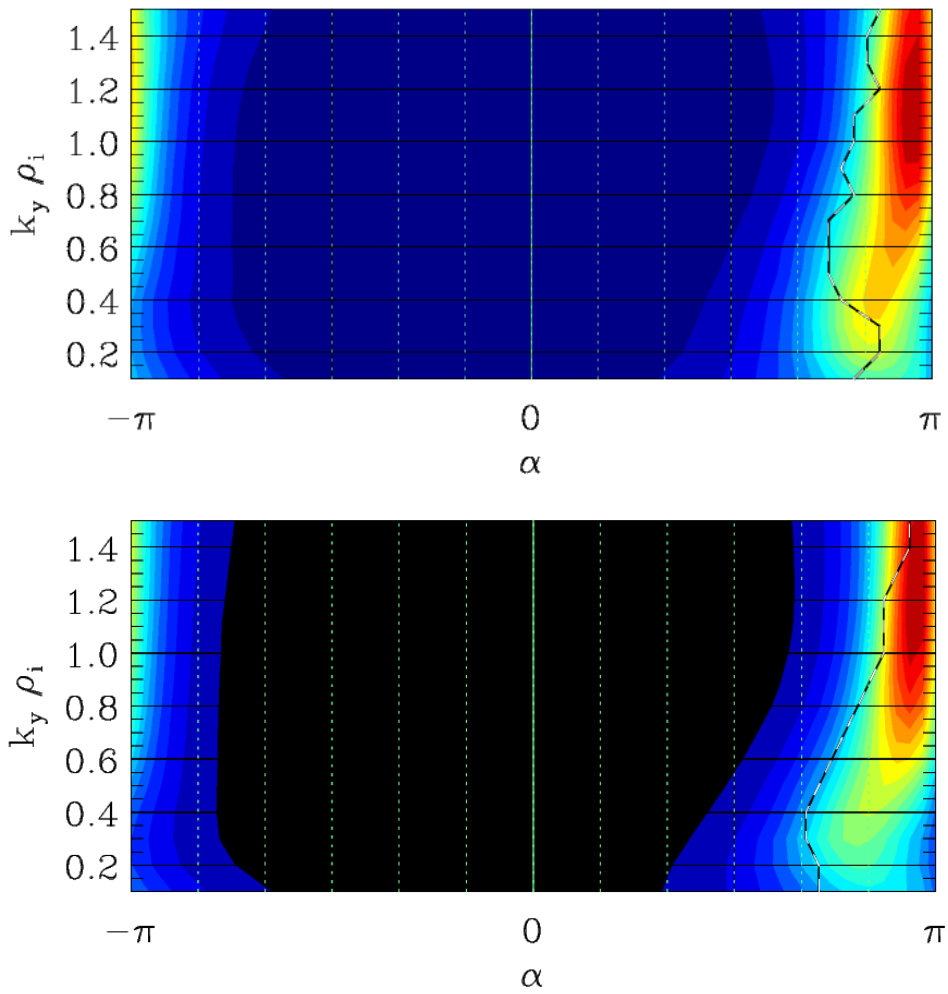


Figure 4.6: The probability distribution function for the nonlinear cross-phase α between Φ and T_i^{tot} for the NCSX (top) and HSX (bottom) configurations from simulations with adiabatic electrons. Cross-phases of the dominant linear eigenmode (black dashed curve) are included for comparison.

applies to the dominant mode in each configuration, and an analysis that includes more subdominant modes may lead to other conclusions being drawn.

A moderate difference is observed in the nonlinear data at $k_y \rho_s < 0.6$, where the phase is less peaked for the HSX configuration, which may be interpreted as a consequence of contributions from the more complex subdominant eigenmode landscape. This interpretation is consistent with the fact that at higher k_y , the number of subdominant modes decreases significantly in the HSX geometry. For example, at $k_y \rho_s = 1.5$, there are only 16 subdominant modes for HSX as opposed to the 108 subdominant modes at $k_y \rho_s = 0.3$. Overall, there is a moderate difference in cross-phases between HSX and NCSX, but the difference is not significant enough to merit a phase-based explanation for the mismatch between growth rates and heat fluxes.

4.1.8 Nonlinear frequency spectra

The nonlinear frequency spectrum describes the extent to which a fluctuation with a given frequency is present in the nonlinear state [6,7]. Figure 4.7 depicts the nonlinear frequencies as a function of k_y , highlighting the impact of the subdominant mode landscape on the nonlinear system.

One observes a stark difference between the two configurations. In NCSX, the frequency spectrum is very narrow, especially in the low- k_y range. In contrast, HSX exhibits a more broadband frequency structure at all values of k_y , suggesting that no single mode is dominating the system, and that the nonlinear state is comprised of a large number of modes. Note that while

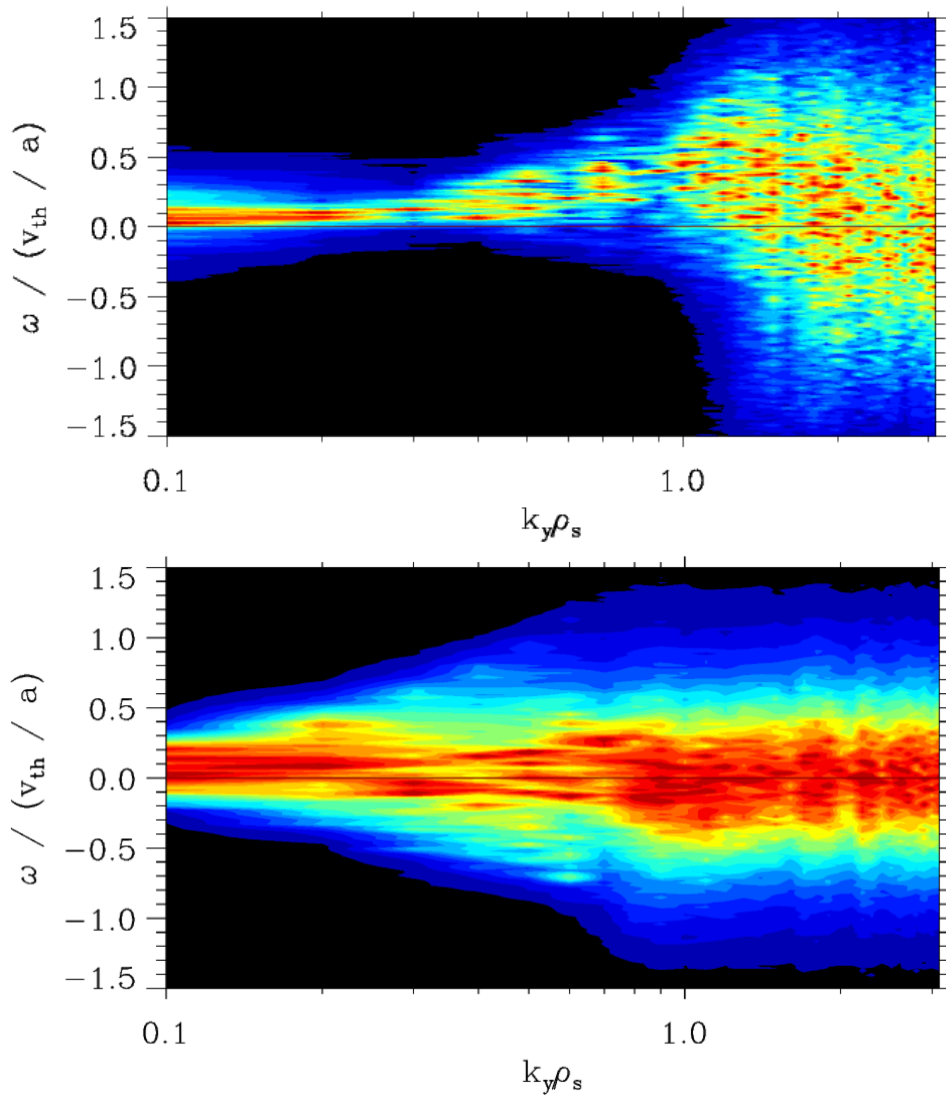


Figure 4.7: The nonlinear frequency spectra for the NCSX (top) and HSX (bottom) configurations from simulations with adiabatic electrons. The color scale, which denotes Fourier mode amplitude, has arbitrary units and is linear and normalized at each k_y separately. It is also important to note that there is an amplitude weighting at each separate k_y so that modes with larger amplitude contribute more significantly.

NCSX also has a broadband frequency spectrum at high k_y , this is less relevant to the transport dynamics, which are dominated by low k_y . Rather, broadband small-scale frequencies are a common feature of microturbulence, as a strong-turbulence regime is reached at sufficiently high wavenumber $k_y \rho_s > 1$.

The dissimilarity between the nonlinear frequency spectra of HSX and NCSX is consistent with the following explanation for the mismatch between quasilinear predictions and the nonlinear Q_i^{es} . It has been shown by Hegna et al., 2018, where a fluid model is used to identify efficient energy transfer channels to stable modes via three-wave interaction, that energy transfer to stable modes via nonlinear three-wave coupling is more efficient in HSX relative to NCSX. This is in large part due to the extended nature of linear eigenmodes as well as the shorter connection lengths in HSX, which allow for more enhanced resonance and interaction of modes in the nonlinear state, yielding a lower saturated heat flux level in HSX. Additionally, in HSX, where there are many more subdominantly unstable modes that contribute significantly to the turbulent state, there are many more possible triplet interactions which include an unstable mode, thereby increasing the activity of stable modes in such triplet wave interactions.

4.2 Kinetic-electron simulations

In this section, results of simulations with kinetic electrons are presented to determine whether adiabatic-electron-simulation results remain valid in more

physically-realistic simulations or not. Electron physics such as trapping and parallel streaming are included in kinetic-electron simulations. This can modify the adiabatic-electron results as additional modes such as TEM, micro-tearing (MTM), or electron temperature gradient (ETG) can impact the dynamics; however, we expect the contribution from these other modes to be small given the small electron temperature gradient used here. For the remainder of this chapter, reference to ‘kinetic electrons’ will also imply that the normalized plasma pressure β is equal to 0.05% in the GENE simulations, where a small but finite value of β is chosen for numerical efficiency and has no relevance to experiment or potential stellarator fusion reactors. Normalized gradient and temperature ratio values used throughout the kinetic-electron simulations presented here are as follows: $a/L_n = a/L_{Te} = T_e/T_i = 1$ and $a/L_{Ti} = 3$. Note that a/L_n is now finite relative to the adiabatic-electron results presented in the previous section. This means that TEM physics may play a role here, but ITG modes will still tend to be dominant.

4.2.1 Linear eigenmodes

In Fig. 4.8, the linear growth rate spectrum is plotted for HSX and NCSX for kinetic electrons. As observed in the adiabatic-electron simulations, NCSX exhibits lower growth rates in the transport-relevant low- k_y regime. The peak growth rate for each configuration occurs at smaller k_y than in the adiabatic-electron case. Also note that the real frequencies for the kinetic-electron case are almost identical to the adiabatic-electron results.

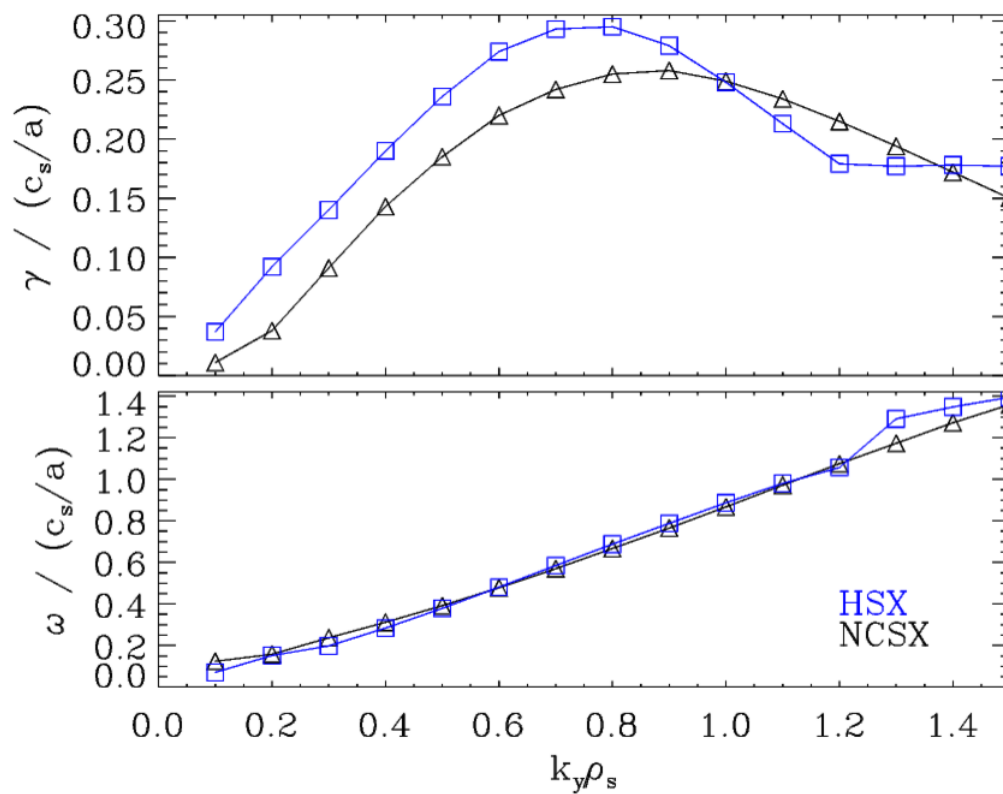


Figure 4.8: Linear growth rate γ (top) and real frequency ω (bottom) as functions of normalized binormal wavenumber k_y for HSX (blue squares) and NCSX (black triangles) from simulations with kinetic electrons. Note that, again, linear ITG growth rates for HSX in the transport-relevant k_y regime are higher than NCSX, by as much as a factor of two or three, depending on the k_y in question.

The large number of subdominant modes present and the characteristic extended eigenmode structures in HSX relative to NCSX discussed in Sec. 4.1 in the adiabatic-electron limit are qualitatively the same when kinetic electrons are included in the simulation. For example, at $s_0 \approx 0.5$ and $k_y \rho_s = 0.2$, NCSX exhibits only one subdominant mode in the kinetic-electron regime versus only one to five subdominant modes present in simulations with adiabatic electrons. Similarly, for NCSX, eigenmodes continue to be localized and centered at the outboard midplane in the bad-curvature region. For the HSX geometry, eigenmodes are significantly more extended along the field line, especially at low k_y , and the subdominant mode landscape of HSX with kinetic electrons is comprised of an order of magnitude or more subdominant modes compared to NCSX.

4.2.2 Nonlinear dynamics

Heat flux time traces for NCSX and HSX are shown in Fig. 4.9 for simulations with kinetic electrons. The average heat flux in each configuration is approximately 36 and 23 in gyroBohm units for NCSX and HSX, respectively, averaged over the quasi-stationary state. This result is consistent with the adiabatic-electron simulations, where $Q_{\text{HSX}} < Q_{\text{NCSX}}$. It is important to note that the heat flux for HSX (NCSX) increases by roughly a factor of 4 (2) comparing adiabatic- to kinetic-electron simulations. The difference in heat flux is now less than a factor of 1.6 here compared to the factor of approximately 3 observed in adiabatic-electron simulations. One possible explanation for this

is the following. Given that the flux values are higher for kinetic electrons, one could conclude that these simulations are further from marginality, which would lead to a smaller relative flux but a comparable difference in fluxes.

Next, heat flux spectra, the Φ and T_i^{tot} cross-phases, and the nonlinear frequency spectra from simulations with kinetic electrons will be discussed. The heat flux spectra from nonlinear simulations with kinetic electrons presented in Fig. 4.10 show that the general shape and peak of both the HSX and NCSX spectra are comparable to the analogous adiabatic-electron result shown in Fig. 4.5. The peak of the HSX heat flux spectra is still at lower k_y than the NCSX peak, indicating that larger-wavelength structures still dominate the heat flux in HSX relative to NCSX. It is worth noting that the peak in the Q_i^{es} flux spectra of each configuration shifts to larger scales relative to their adiabatic-electron analogs. This shift is consistent with the shift in the peak linear growth rate γ when going from adiabatic- to kinetic-electron simulations (Fig. 4.8).

Cross-phases between Φ and T_i^{tot} from simulations with kinetic electrons are presented in Fig. 4.11. Relative to the adiabatic-electron results (Fig. 4.6), the nonlinear cross-phases between Φ and T_i^{tot} for HSX and NCSX from kinetic electron-simulations (Fig. 4.11) exhibit an additional low- k_y feature that extends much closer to $\pi/2$, suggesting that the drive physics as well as transport are more efficient. This is consistent with the fact that the heat fluxes of both HSX and NCSX are higher in simulations with kinetic electrons.

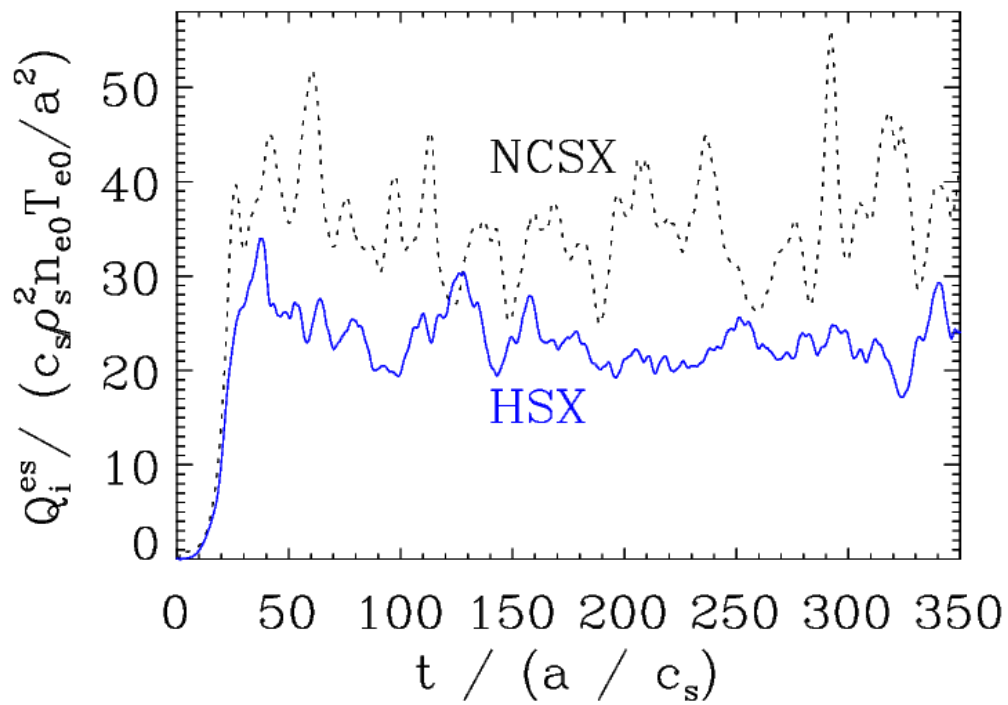


Figure 4.9: Heat flux time traces for the HSX (blue solid line) and NCSX (black dashed line) configurations from simulations with kinetic electrons. The electrostatic ion heat flux for HSX remains lower than NCSX even for kinetic electrons.

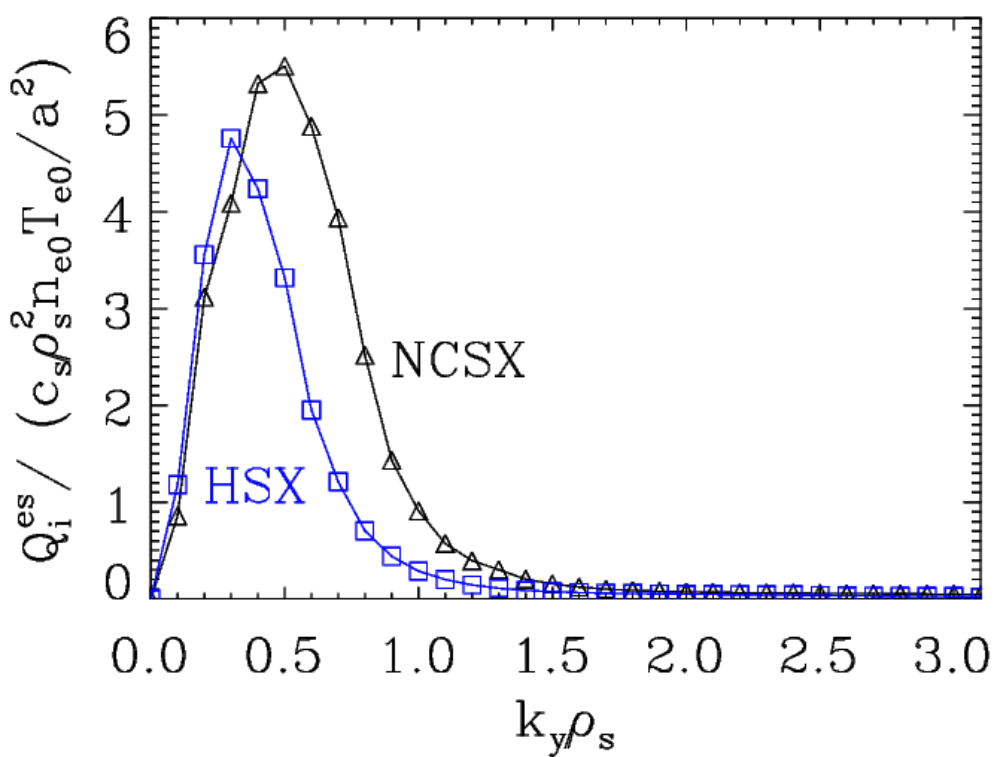


Figure 4.10: Heat flux spectra for HSX (blue squares) and NCSX (black triangles) with kinetic electrons. Two important things to note: the HSX spectrum peaks at lower k_y , a finding that is consistent with adiabatic-electron results and a downshift in peaks is observed relative to the linear growth rate spectra for HSX and NCSX, another finding that is consistent with the adiabatic-electron results.

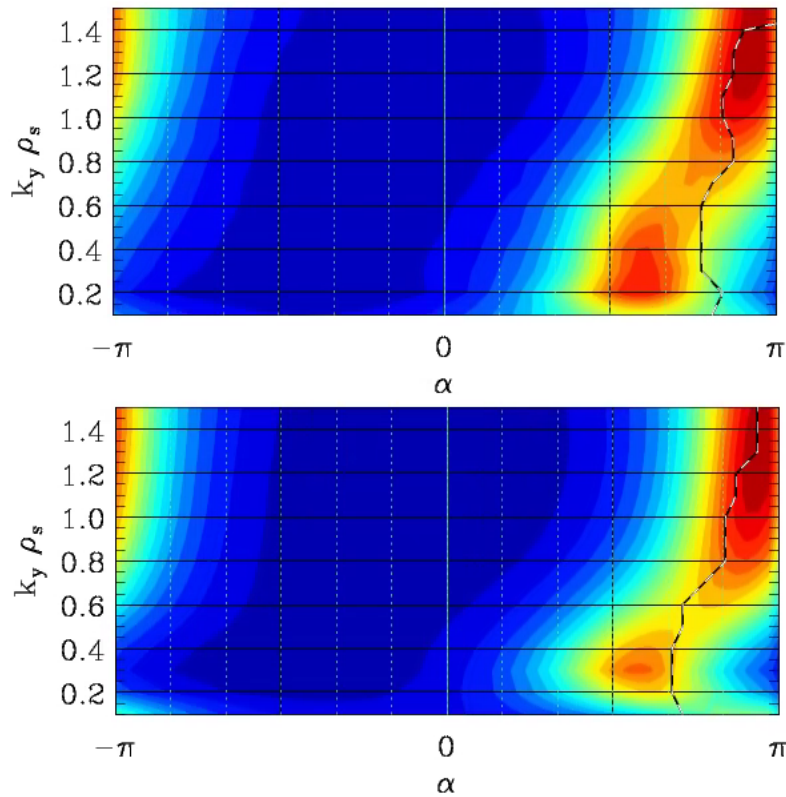


Figure 4.11: The probability distribution function for the nonlinear cross-phase between Φ and T_i^{tot} for simulations of NCSX (top) and HSX (bottom) with kinetic electrons. Linear cross-phases of the dominant eigenmode are overlaid (black dashed curve) for comparison. The nonlinear cross-phase color scale is linear. It is important to note the prominent low- k_y feature present in both configurations, a result which suggests that the transport mechanism is more efficient relative to the adiabatic-electron case. This is consistent with the increase in fluxes.

Similar to the adiabatic-electron case, the nonlinear cross-phases are very similar for both configurations. One observes a slight mismatch between the linear and nonlinear phases for each configuration at low k_y , a region with a slightly stronger linear phase signature for HSX and a slightly stronger nonlinear phase signature for NCSX, highlighted by the greater intensity of red near $\pi/2$.

Lastly, nonlinear frequency spectra in simulations with kinetic electrons are shown. As was the case in the adiabatic-electron simulations, the nonlinear frequency spectra in the kinetic-electron case suggests that the difference in linear subdominant-mode physics between configurations has an impact on the quasi-stationary state of the turbulence. While the difference between the nonlinear frequency spectra of each configuration is less stark in kinetic-electron simulations, there is still a distinct difference in the $0.2 < k_y \rho_s < 0.6$ range where the frequency spectrum of HSX is distinctly broadband relative to NCSX, where it is very much peaked over that same range. This is especially important since it is these length scales that dominate the transport. While the difference in nonlinear frequency spectra is especially clear for the adiabatic-electron ITG regime, one would expect it to be more complex for significantly stronger a/L_n or a/L_{Te} , as trapped-electron modes and potentially kinetic ballooning modes (see Ch. 5) will complicate the subdominant mode landscape. At low k_y , for HSX, Fig. 4.12 suggests that there are a large number of modes contributing to the nonlinear state compared to relatively few

modes for NCSX. It is also worth noting that there are qualitative differences at high k_y between the nonlinear frequency spectra from adiabatic-electron (Fig. 4.7) and kinetic-electron (Fig. 4.12) simulations for both configurations, where in the kinetic-electron case the turbulence is more broadband than in the adiabatic-electron case. However, given that the dynamics of ITG turbulence is dominated by low- k_y behavior, it is unlikely that these qualitative differences play a significant role in setting transport levels.

Arguably, comparing nonlinear heat fluxes in gyro-Bohm units may not be the most appropriate metric to use when comparing two magnetic geometries of differing aspect ratio. As noted by Helander et al. [15], the total power crossing a flux surface $P = \int \mathbf{Q} \cdot d\mathbf{S}$ is potentially a more appropriate quantity for such a comparison between HSX and NCSX. To lowest order, assuming that the plasma parameters are the same between configurations, this quantity P is equal to the gyro-Bohm-normalized heat flux multiplied by a geometric factor that is approximately the aspect ratio. Since the aspect ratio of HSX is roughly two times as large as the aspect ratio of NCSX, this would lead one to conclude that comparing $2Q_{\text{HSX}}$ and Q_{NCSX} would be necessary for a proper comparison of HSX and NCSX. While this conversion factor changes the quantitative measures of the turbulent transport, this does not change the fact that quasilinear estimates do not accurately predict nonlinear heat flux when comparing HSX and NCSX, as a performed quasilinear comparison leads one to expect that HSX should perform worse than NCSX with respect

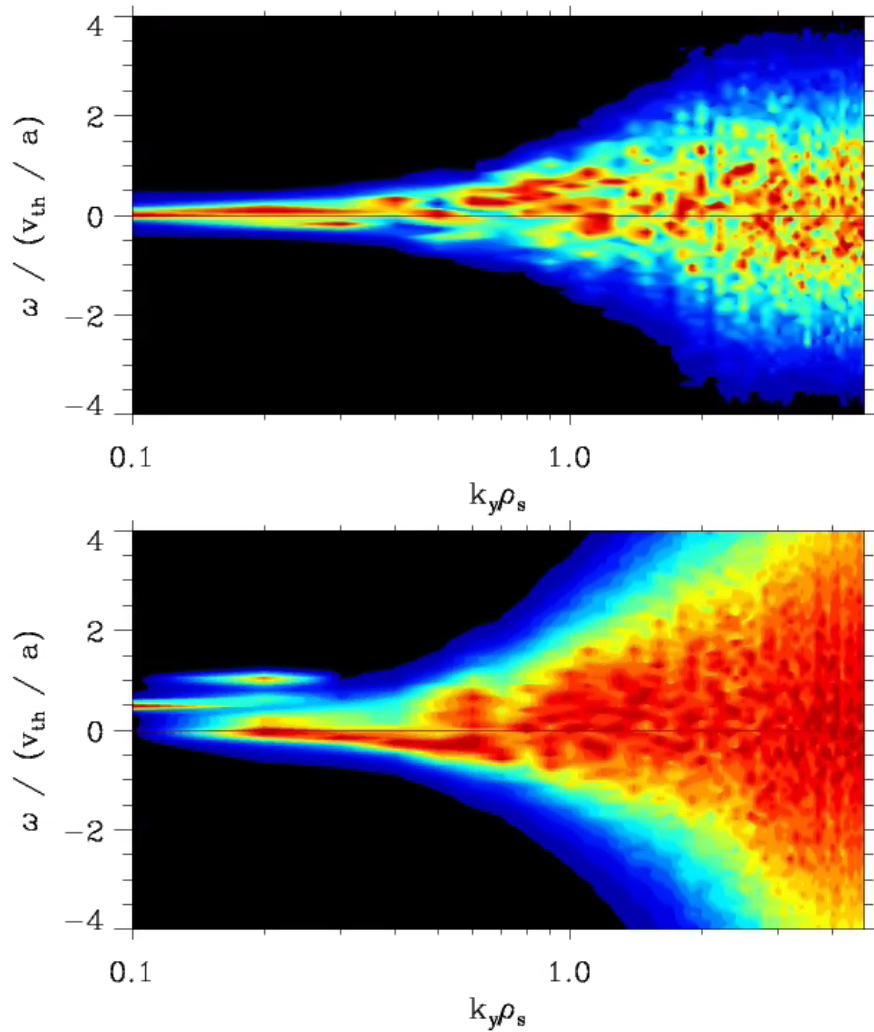


Figure 4.12: Nonlinear frequency spectra of NCSX (top) and HSX (bottom) from simulations with kinetic electrons. The color scale is linear and normalized at each k_y separately, and its units are arbitrary. Note the broadband nature of the turbulence in the HSX case relative to the narrow spectrum for NCSX.

to ITG turbulent transport by a factor of 4.2 in the adiabatic-electron case. Using peak linear growth rates as a measure for turbulent transport is not a reliable indicator for a range of quasi-symmetric stellarators.

4.3 Conclusions of this chapter

Results presented in this chapter include both linear and nonlinear gyrokinetic simulations of ITG turbulence for two specific quasi-symmetric stellarator configurations, HSX (quasi-helical symmetry) and NCSX (quasi-axial symmetry). Simulations with both adiabatic and kinetic electrons are discussed. Linear eigenvalue simulations show that HSX exhibits a large number of subdominant ITG modes, whereas only a few subdominant modes are present in NCSX. Eigenmodes are much more extended along the field line in HSX, due to the small average magnetic shear at $s_0 \approx 0.5$. In contrast, NCSX has localized eigenmodes centered in the bad curvature region at the outboard midplane. The most unstable ITG mode has a smaller normalized growth rate in NCSX compared to HSX, especially in the transport-relevant low- k_y regime. This is consistent with the results of previous work by Rewoldt et al. [5] comparing HSX and NCSX. However, nonlinear simulations reveal that, contrary to expectations based on either linear or quasilinear calculations, HSX has lower heat fluxes in gyro-Bohm units compared to NCSX, especially in the limit of adiabatic electrons. One sees, especially through nonlinear frequency spectra, that the ITG turbulence is qualitatively different between HSX and NCSX. In

HSX, the turbulent state is comprised of a large number of concurrently excited modes compared to NCSX where only a few modes dominate the system, especially at low k_y .

As outlined in this chapter, differences in the subdominant mode landscape and characteristic eigenmode structure, which are not captured by dominant linear growth rates alone, can impact the nonlinear ITG turbulence saturation dynamics. Thus, proxies based on nonlinear physics for quantities such as ITG turbulent transport must be developed and properly compared against nonlinear simulations before they can be used to predict Q_i^{es} across quasi-symmetric stellarator designs. As will be shown in Ch. 5, an important component for future work is to develop a fluid model for ITG-KBM turbulence saturation from which useful transport proxies can be derived and then implemented into optimization schemes.

A potential explanation for how this qualitative difference could lead to lower saturated heat flux is as follows. A theory for ITG turbulent saturation in stellarators has recently been developed that suggests that quasi-helically symmetric stellarators have an intrinsic advantage with regard to turbulent saturation physics relative to other configurations [2]. The theory relies on a paradigm of nonlinear energy transfer from unstable to damped eigenmodes at comparable wavelength as the dominant saturation process [2,16]. This process is enabled by a three-wave interaction where the third mode, either a zonal or marginally stable finite- k_y mode, depending upon the properties of the

magnetic geometry, primarily determines the nonlinear energy transfer rate. Quantification of the metrics emerging from the theory suggests that HSX has much larger nonlinear energy transfer rates relative to NCSX, suggesting lower turbulence levels and reduced turbulent transport. This difference is primarily due to the relatively short connection lengths and low magnetic shear present in HSX, which enable strong three-wave interaction between turbulent eigenmodes of the system. More extended eigenmodes in HSX facilitate better nonlinear coupling between modes, producing more efficient transfer of energy to stable modes. The calculations presented in this chapter are consistent with the above explanation for the evolution of the energetics of the ITG turbulence, providing a possible explanation for why HSX saturates at a lower heat flux level than NCSX in nonlinear simulations.

Citations

- [1] McKinney, I.J., Pueschel, M.J., Faber, B.J., Hegna, C.C., Talmadge, J.N., Anderson, D.T., Mynick, H.E., & Xanthopoulos, P. 2019 A comparison of turbulent transport in a quasi-helical and a quasi-axisymmetric stellarator. *J. Plasma Phys.* **85**, 905850503.
- [2] Hegna, C.C., Terry, P.W., & Faber, B.J. 2018 Theory of ITG turbulent saturation in stellarators: identifying mechanisms to reduce turbulent transport. *Phys. Fluids* **18** (5), 552-565.
- [3] Mynick, H.E., Pomphrey, N., & Xanthopoulos, P. 2010 Optimizing stellarators for turbulent transport. *Phys. Rev. Lett.* **105** (9), 095004.
- [4] Mynick, H.E., Pomphrey, N., & Xanthopoulos, P. 2011 Reducing turbulent transport in toroidal configurations via shaping. *Phys. Plasmas* **18**, 056101.
- [5] Rewoldt, G., Ku, L.-P., & Tang, W.M. 2005 Comparison of microinstability properties for stellarator magnetic geometries. *Phys. Plasmas* **12** (10), 102310.
- [6] Faber, B.J., Pueschel, M.J., Proll, J.H.E., Xanthopoulos, P., Terry, P.W., Hegna, C.C., Weir, G.M., Likin, K.M., & Talmadge, J.N. 2015 Gyrokinetic

studies of trapped electron mode turbulence in the Helically Symmetric eXperiment stellarator. *Phys. Plasmas* **22** (7), 072305.

[7] Pueschel, M.J., Faber, B.J., Citrin, J., Hegna, C.C., Terry, P.W., & Hatch, D.R. 2016 Stellarator turbulence: subdominant eigenmodes and quasilinear modeling. *Phys. Rev. Lett.* **116** (8), 085001.

[8] Pueschel, M.J., Görler, T., Jenko, F., Hatch, D.R., & Cianciara, A.J. 2013 On secondary and tertiary instability in electromagnetic plasma microturbulence. *Phys. Plasmas* **20** (10), 102308.

[9] Terry, P.W., Baver, D.A., & Gupta, S. 2006 Role of stable eigenmodes in saturated local plasma turbulence. *Phys. Plasmas* **13** (2), 022307.

[10] Hatch, D.R., Terry, P.W., Nevins, W.M., & Dorland, W. 2009 Role of stable eigenmodes in gyrokinetic models of ion temperature gradient turbulence. *Phys. Plasmas* **16** (2), 022311.

[11] Candy, J., Waltz, R.E., & Dorland, W. 2004 The local limit of global gyrokinetic simulations. *Phys. Plasmas* **11** (5), L25-L28.

- [12] Dewar, R.L. & Glasser, A.H. 1983 Ballooning mode spectrum in general toroidal systems. *Phys. Fluids* **26** (10), 3038-3052.
- [13] Whelan, G.G., Pueschel, M.J., Terry, P.W., Citrin, J., McKinney, I.J., Guttenfelder, W., & Doerk, H. 2019 Saturation and nonlinear electromagnetic stabilization of ITG turbulence. *Phys. Plasmas* **26** (8), 082302.
- [14] Citrin, J., Arnichand, H., Berndardo, J., Bourdelle, C., Garbet, X., Jenko, F., Hacquin, S., Pueschel, M.J., & Sabot, R. 2017 Comparison between measured and predicted turbulence frequency spectra in ITG and TEM regimes. *Phys. Plasmas* **59** (6), 064010.
- [15] Helander, P., Bird, T., Jenko, F., Kleiber, R., Plunk, G.G., Proll, J.H.E., Riemann, J., & Xanthopoulos, P. 2015 Advance in stellarator gyrokinetics. *Nucl. Fusion* **55** (5), 053030.
- [16] Terry, P.W., Faber, B.J., Hegna, C.C., Mirnov, V.V., Pueschel, M.J., & Whelan, G.G. 2018 Saturation scalings of toroidal ion temperature gradient turbulence. *Phys. Plasmas* **25** (1), 012308.

Chapter 5

Electromagnetic turbulence in stellarators

In this chapter, linear and nonlinear results pertaining to ITG and kinetic-ballooning-mode (KBM) turbulence in HSX and Heliotron-J will be presented. Aspects of linear KBM instability such as the normalized electron plasma pressure $\beta = 8\pi p_e/B^2$, where p_e is the electron pressure, at which KBM becomes the dominant instability, denoted $\beta_{\text{crit}}^{\text{KBM}}$, will be shown. Additional calculations elucidating how $\beta_{\text{crit}}^{\text{KBM}}$ scales with both average magnetic shear \hat{s} and normalized ion temperature gradient ω_{Ti} (while keeping the total pressure gradient constant) in HSX will also be presented. The final portion of the numerical results section of this chapter will focus on nonlinear electromagnetic simulations in the HSX geometry, which highlight a heuristic condition, the smallest finite k_y of the simulation must be stable to KBM, that must be satisfied to achieve nonlinear saturation. It is also worth noting that HSX exhibits significant nonlinear finite- β stabilization. The heat flux in electromagnetic simulations of HSX decreases by a factor of ≈ 4 when $\beta = 0.48\%$ relative to simulations with $\beta = 0.05\%$ when keeping the pressure gradient constant. Additionally,

a number of analyses presented in the nonlinear section will highlight the importance of KBMs in the nonlinear state, especially in terms of energy transfer dynamics.

In electromagnetic simulations of NCSX, a magnetic configuration with substantially higher \hat{s} , one observes dominant ITG modes at small normalized plasma pressure until some $\beta = \beta_{\text{crit}}^{\text{KBM}}$ which is consistent with the MHD ballooning threshold, above which KBMs become the dominant instability. As will be shown, this same transition from ITG to KBM in HSX occurs at a very small value of β ($\approx 0.1\%$), an order of magnitude below the MHD ballooning threshold $\beta_{\text{crit}}^{\text{MHD}} \approx 1.1\%$, for ITG-relevant gradient settings. This small $\beta_{\text{crit}}^{\text{KBM}}$ is also observed in GENE simulations in the Heliotron-J geometry, another low-magnetic-shear device, and in a circular tokamak geometry with small \hat{s} . This unexpected KBM behavior motivates the study of KBM turbulence and saturation in low-magnetic-shear, three-dimensional magnetic equilibria.

In addition to simulations, a derivation of an analytic fluid model, which extends the three-field fluid model from C.C. Hegna et al. [1] to include finite- β effects, will be presented and discussed. As was done for ITG turbulence with the three-field model, the motivation for the five-field model is to study the saturation of KBM-ITG turbulence in three-dimensional equilibria within the context of energy transfer from unstable to stable modes at comparable wavenumber.

5.1 Linear KBM physics

There exists a large body of research done which investigates kinetic ballooning modes [2-5]. Like ITG modes, KBMs are destabilized by regions of bad curvature, regions where the pressure gradient and the curvature $\vec{\kappa}$ are in the same direction. KBMs are primarily driven by pressure gradients, like its ideal MHD ballooning mode counterpart. Relative to the ideal MHD analog, kinetic effects such as trapped-particle, wave-particle-resonance, and finite-larmor-radius dynamics must be taken into account to properly capture KBM dynamics [6,7], meaning that gyrokinetics is an appropriate tool for studying KBMs in various magnetic equilibria. As was mentioned above, the trend in the change of ITG and KBM growth rates with respect to increasing β is as follows. The ITG is stabilized by increasing β [8-10], the KBM is destabilized by increasing β [11-13], and at $\beta_{\text{crit}}^{\text{KBM}}$, KBM becomes the dominant instability at a given wavenumber k_y . This behavior is present in both HSX and Heliotron-J at larger values of k_y . However, as will be shown, at lower k_y , there is little stabilization of the ITG prior to KBM becoming dominant. The simulation parameters used in the following subsections, unless otherwise stated, are the following: $a/L_n = a/L_{Te} = T_e/T_i = 1$ and $a/L_{Ti} = 3$.

5.1.1 KBMs in HSX

Relative to the linear electrostatic simulations in Ch. 4 (see the real frequencies from Figs. 4.1 and 4.8), where ITG was the dominant instability for

all simulated values of k_y , electromagnetic simulations of HSX present a richer physics picture. Depending on the value of β , it is possible for KBMs to be the dominant instability over some range of binormal wavenumbers k_y rather than ITG. Figure 5.1 highlights this exact situation: a case where KBM dominates between $k_y\rho_s = 0.1$ and 0.2 and ITG above and below this range. It is important to note that the KBM is first destabilized at finite k_y in HSX, an observation that will be important within the context of nonlinear simulations of HSX in Sec. 5.2. This means that a nonlinear simulation of HSX with $\beta \approx 0.48\%$ would result in a combination of ITG and KBM turbulence rather than purely electromagnetic ITG or KBM turbulence.

A quantity integral to the understanding of linear KBM dynamics is the threshold $\beta_{\text{crit}}^{\text{KBM}}$ at which KBM becomes the dominant instability. To extract this quantity $\beta_{\text{crit}}^{\text{KBM}}$ numerically, a β scan is performed at a single value of k_y , as is outlined in Fig. 5.2, and $\beta_{\text{crit}}^{\text{KBM}}$ can then be determined for that value of k_y . Figure 5.2 shows both linear growth rates and real frequencies for $k_y\rho_s = 0.6$ as a function of β . Note in Fig. 5.2 that ITG is stabilized as β increases until KBM becomes the dominant instability at $\beta \approx 2.2\%$. This is characteristic of plots of growth rate as a function of β at other values of k_y , with one qualitative difference: at lower values of k_y one observes little ITG stabilization prior to the onset of KBM, which can be seen in Fig. 5.3.

In HSX, for higher values of k_y , the $\beta_{\text{crit}}^{\text{KBM}}$ is 2% or higher. However, as one looks to lower k_y , the $\beta_{\text{crit}}^{\text{KBM}}$ becomes very small, as shown in Fig. 5.3, a plot of

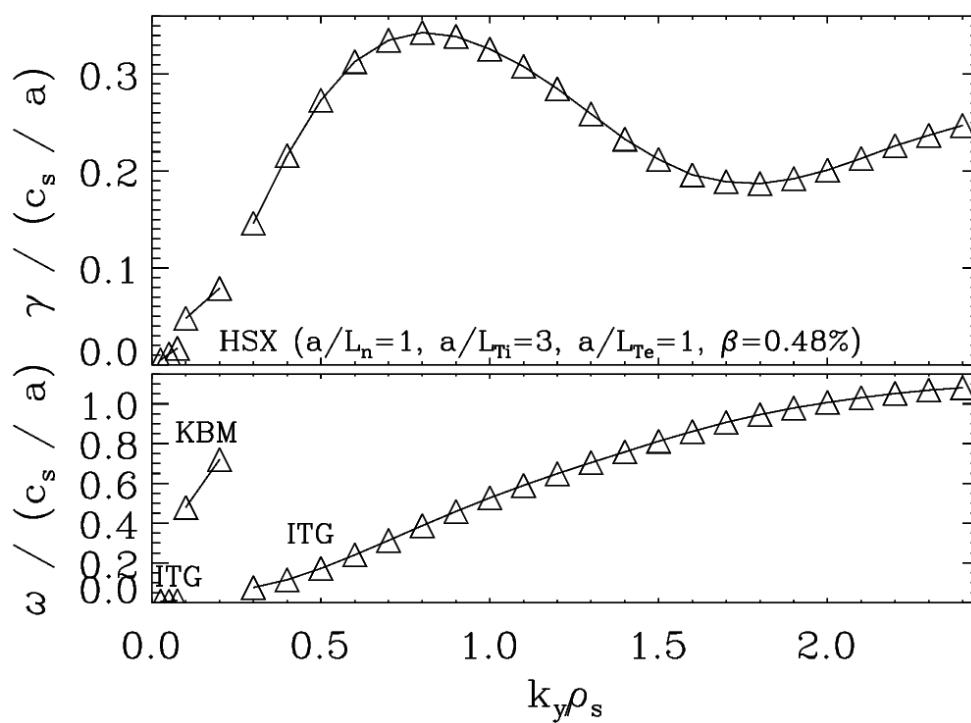


Figure 5.1: γ and ω as functions of k_y with $\beta = 0.48\%$, roughly half of the MHD ballooning threshold $\beta \approx 1.1\%$. Note the discontinuity in real frequency near $k_y \rho_s \approx 0.1$, an indication of a change in mode branch from ITG to KBM. Also note that at high $k_y \rho_s > 1.8$, the growth rate begins to increase again, but that there is no discontinuity in the real frequency.

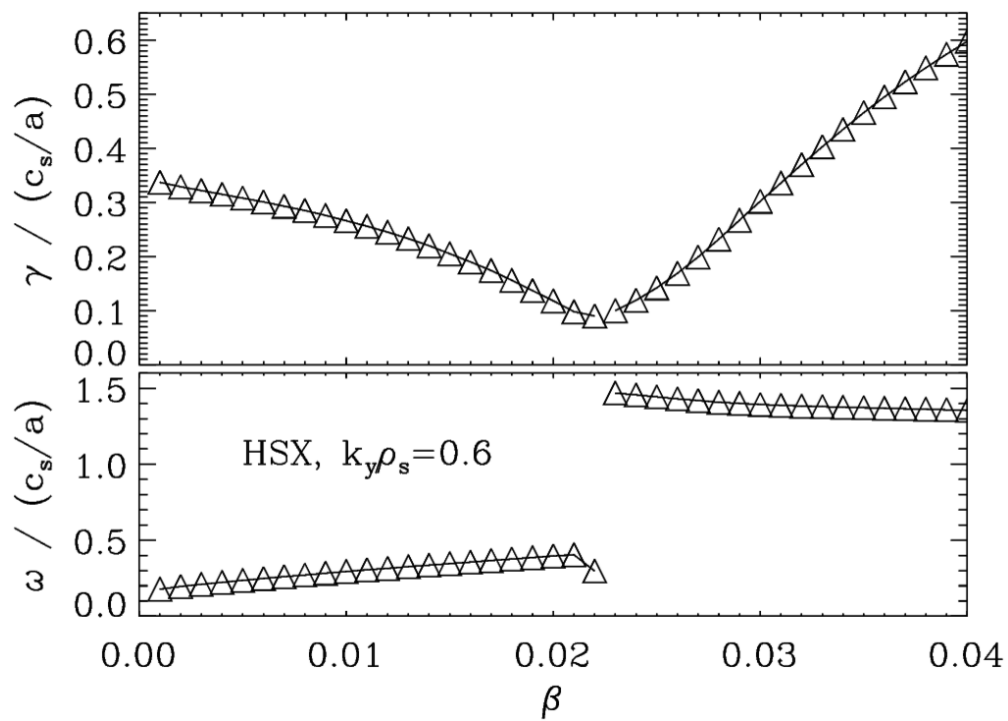


Figure 5.2: γ and ω as functions of β for $k_y \rho_s = 0.6$. Observe the discontinuity in real frequency near $\beta_{\text{crit}}^{\text{KBM}} \approx 2.3\%$, an indication of a change in mode branch from ITG to KBM.

growth rates and real frequencies as functions of β in HSX for the $k_y \rho_s = 0.1$ case, where $\beta_{\text{crit}}^{\text{KBM}} \approx 0.1\%$. Repeating these scans over a range of k_y values yields the result shown in Fig. 5.4, depicting $\beta_{\text{crit}}^{\text{KBM}}$ as a function of k_y for both the HSX and NCSX configurations. $\beta_{\text{crit}}^{\text{MHD}}$ is also included in the figure for reference, where one would expect $\beta_{\text{crit}}^{\text{KBM}}(k_y \rightarrow 0)$ to approach $\beta_{\text{crit}}^{\text{MHD}}$.

The KBM behavior observed in electromagnetic simulations of HSX, the low $\beta_{\text{crit}}^{\text{KBM}}$ between $k_y \rho_s \approx 0.1$ and 0.2 , is potentially not ideal for a reactor-relevant experiment, as a reactor will operate well above $\beta \approx 1\%$. Also note in Fig. 5.4 that for values of $k_y \rho_s < 0.1$, the $\beta_{\text{crit}}^{\text{KBM}}$ begins to increase toward $\beta_{\text{crit}}^{\text{MHD}}$. This feature of the KBM dynamics has important consequences for achieving nonlinear saturation of electromagnetic simulations of HSX, as will be shown below in Sec. 5.2. Next, there will be a discussion of an eigenvalue calculation in the KBM regime, highlighting the destabilization of multiple branches of KBMs rather than just a single mode.

5.1.2 Destabilization of multiple branches of KBMs

As was discussed in Sec. 4.1.2, GENE includes functionality for eigenvalue calculations of the linear operator of the system, allowing for the analysis of the subdominant mode landscape. The subdominant mode spectrum of HSX at $k_y = 0.2$ with $\beta = 0.5\%$, shown in Fig. 5.5, leads to the conclusion that there is not just a single KBM that is destabilized as β increases, but rather there are two families of KBMs, one of which is a set of modes that are centered at the outboard midplane (at ballooning angle $\theta_p = 0$) and another

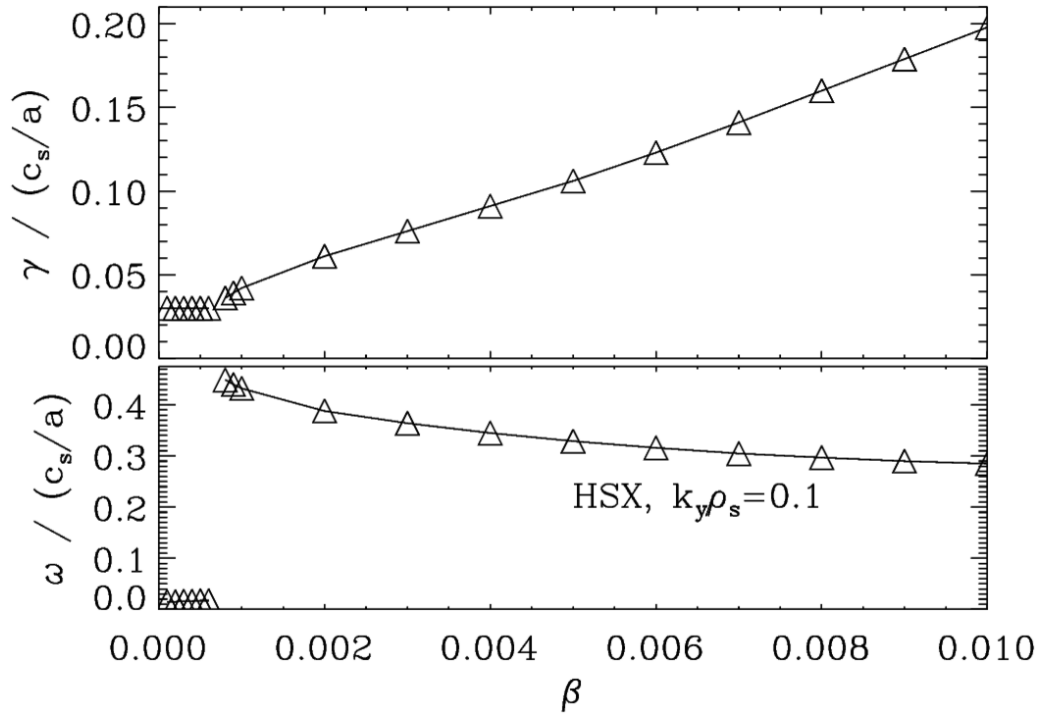


Figure 5.3: γ and ω as functions of β for $k_y = 0.1$. Observe the low value of $\beta_{\text{crit}}^{\text{KBM}}$ ($\approx 0.07\%$), compared with the ideal ballooning threshold of $\beta_{\text{crit}}^{\text{MHD}} \approx 1.1\%$ in HSX. This aspect of the KBM dynamics in HSX makes it difficult to achieve saturation in nonlinear simulations of HSX above $\beta_{\text{crit}}^{\text{KBM}}$.

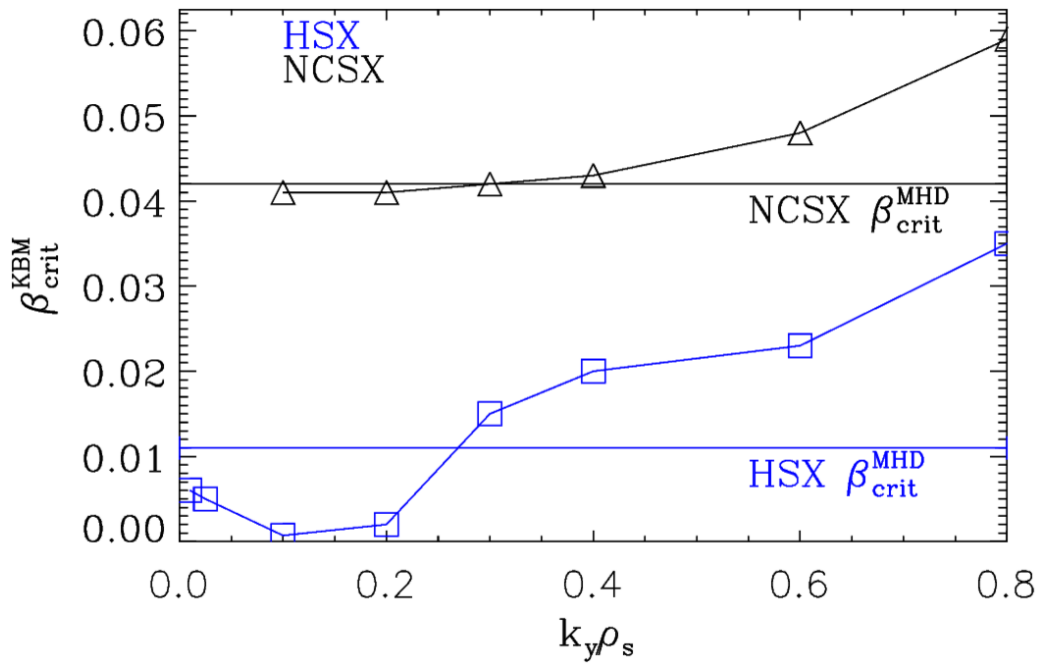


Figure 5.4: $\beta_{\text{crit}}^{\text{KBM}}$ as a function of k_y for both the HSX (blue squares) and NCSX (black triangles) configurations. $\beta_{\text{crit}}^{\text{MHD}}$ is included for comparison, as calculated by an MHD ballooning code [14]. For HSX, in the range of k_y between 0.1 and 0.2, KBMs are destabilized at very low values of β .

which consists of pairs of sibling modes that peak away from the outboard midplane ($\theta_p \neq 0$). It should be noted that some of the centered KBMs exhibit tearing parity (blue and green curves in the bottom panel of Fig. 5.5), i.e., the Φ eigenfunctions are odd in ballooning angle. The low background magnetic shear in the present scenario enables destabilization of these modes, termed tearing-parity KBMs or TKBMs, which had previously been conjectured not to exist based on a study involving high-shear equilibria [18]. It is worth noting that it is unlikely that the TKBMs discussed here are microtearing modes because of the ion-temperature-gradient-dependence of the modes, the fact that the modes propagate in the ion diamagnetic direction, and the relatively small nonlinear electron thermal transport, three qualities that are not characteristic of microtearing modes. For each mode that peaks away from the outboard midplane, a sibling mode exists with the same growth rate and frequency with an eigenmode structure that is near-perfectly mirrored with respect to $\theta_p = 0$. The physics implication of this is that HSX is qualitatively different than typical high- \hat{s} tokamak cases, where only a single KBM is destabilized. It should also be noted that a large number of subdominant ITG and TEM modes exist in this parameter regime as well. Eigenvalue calculations with different gradients, $a/L_{T_i} = 4$ and $a/L_{T_i} = 5$ for examples (with a/L_n and a/L_{T_e} kept fixed), also exhibit the two branches of KBMs. However, the exact location of minimal $\beta_{\text{crit}}^{\text{KBM}}$ shifts in k_y -space relative to the $a/L_{T_i} = 3$ case. The region of k_y -space in which the outboard-midplane-peaked KBMs

are dominant shifts to smaller k_y as ω_{Ti} increases. It should also be noted that the two branches of KBM are numerically converged. The presence of a number of unstable KBMs may complicate analysis of the nonlinear energy dynamics.

5.1.3 Dependence of KBM on magnetic shear \hat{s}

One parameter that plays an important role in determining $\beta_{\text{crit}}^{\text{KBM}}$ is the average normalized magnetic shear \hat{s} . The magnetic shear provides a stabilizing effect on drift waves, such as ITG and KBM, since it localizes modes (usually to the outboard midplane) and it reduces the overall spatial extent of the mode [15]. This is observed in simulations of HSX, as outlined in Fig. 5.6, a plot of $\beta_{\text{crit}}^{\text{KBM}}$ as a function of \hat{s} . Note that in these calculations, the magnetic geometry is locally self-consistent in the sense that $d\nu/dr_{\text{eff}}$ is changed such that the desired \hat{s} value is achieved and then the metric elements are self-consistently calculated. Also apparent from the figure is the fact that, regardless of sign, \hat{s} acts to increase $\beta_{\text{crit}}^{\text{KBM}}$ at $k_y\rho_s = 0.1$, an indication that small $|\hat{s}|$ is correlated with early onset of KBMs. One interesting fact is that $\beta_{\text{crit}}^{\text{KBM}}$ is larger for positive values of shear when $|\hat{s}| > 0.3$ and $\beta_{\text{crit}}^{\text{KBM}}$ is larger for negative shear when $|\hat{s}| \leq 0.3$. Again, this is an aspect of the linear KBM physics which could be used as a benchmark for the five-field model.

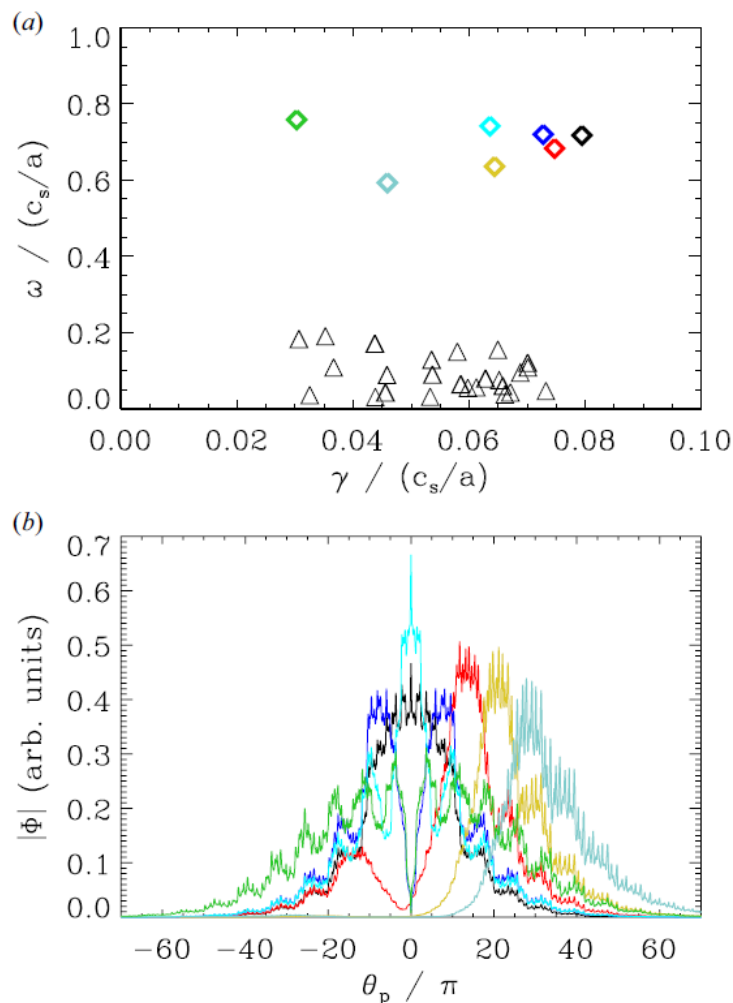


Figure 5.5: The subdominant spectrum (a) for HSX with $k_y = 0.2$ and $\beta = 0.5\%$ consisting of KBMs (diamonds) and ITG modes (triangles), and the associated electrostatic potential Φ eigenmode structures (denoted by the same color as the associated diamond) (b) for various KBMs. Note the two distinct families of KBMs: one with Φ symmetric about $\theta_p = 0$ and one with off-center peaking. For each mode of the latter family, there is a sibling mode that is mirrored across the $\theta_p = 0$ axis with identical γ and ω ; hence they are indistinguishable in (a). Also note that some of the centered KBMs (blue, green) have tearing parity, i.e. are odd functions of ballooning angle.

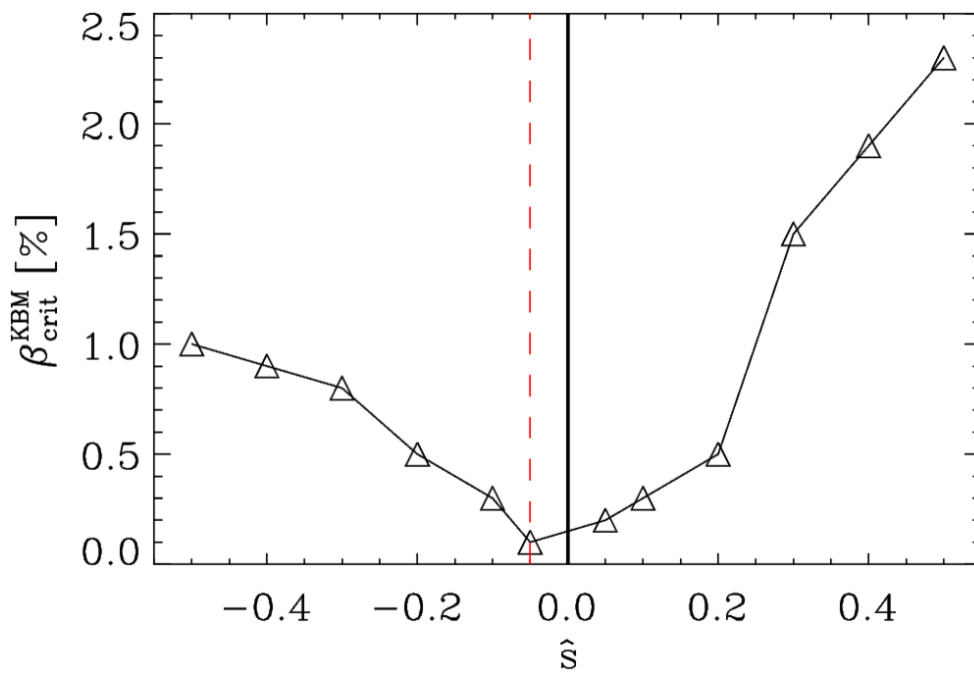


Figure 5.6: $\beta_{\text{crit}}^{\text{KBM}}$ at $k_y \rho_s = 0.1$ as a function of the average magnetic shear \hat{s} along the flux tube. The dashed vertical red line indicates the value of the nominal magnetic shear of HSX. Note the increase in $\beta_{\text{crit}}^{\text{KBM}}$ as $|\hat{s}|$ increases, regardless of sign.

5.1.4 Dependence of the KBM threshold on ω_{Ti}

The ion temperature gradient plays an integral role in determining how $\beta_{\text{crit}}^{\text{KBM}}$ changes as a function of k_y in HSX. As outlined in Fig. 5.7, a plot of $\beta_{\text{crit}}^{\text{KBM}}$ as a function of k_y for HSX, when the sum of gradients is kept constant (relative to the $a/L_n = a/L_{Te} = 1, a/L_{Ti} = 3$ case) and the ion temperature gradient is zeroed out, $\beta_{\text{crit}}^{\text{KBM}}$ is no longer particularly small at $k_y \rho_s = 0.1$. The insight that $\beta_{\text{crit}}^{\text{KBM}}$ is particularly sensitive to the ion temperature gradient may seem counterintuitive since based on ideal-MHD physics, one would expect $\beta_{\text{crit}}^{\text{KBM}} \propto 1/(\omega_{Ti} + \omega_{Te} + 2\omega_n)$. However, this expectation may not hold in low-magnetic-shear three-dimensional magnetic geometries. A preliminary, lowest-order analysis of the ion-magnetic-drift resonance condition, derived using a two-fluid model which accounts for kinetic effects, given in Ref. [19], and discussed in Ch. 2:

$$(\omega - 5/3\omega_{Di})^2 - 10/9\omega_{Di}^2 = 0, \quad (5.1)$$

where $\omega_{Di} = 2cT_i/(eB^3)(\nabla B \times \mathbf{B}) \cdot \mathbf{k}_\perp$, suggests that the KBM frequencies observed in the present work exhibit good agreement with that which is required for exact resonance. Note the different sign used in the parenthetical in Eq. 5.1 due to the difference in sign convention used for ω here relative to Ref. [19]. Taking $T_e/T_i = 1$, $2cT_i/(eB) \rightarrow c_s \rho_s$, and $\nabla B \rightarrow B/a$, the ion-magnetic-drift frequency can be written as $\omega_{Di}/(c_s/a) \approx k_\perp \rho_s$. After computing an eigenmode average for $k_\perp \rho_s$ which accounts for geometry, given by

$$\langle k_{\perp} \rho_s \rangle = \frac{\int |\Phi|^2 ((k_x \rho_s)^2 g^{xx} + 2k_x k_y \rho_s^2 g^{xy} + (k_y \rho_s)^2 g^{yy})^{1/2} d\theta_p}{\int |\Phi|^2 d\theta_p}, \quad (5.2)$$

where g^{xx} , g^{xy} , and g^{yy} are magnetic geometry elements, $\omega_{Di}/(c_s/a) \approx \langle k_{\perp} \rho_s \rangle$ yields a normalized ion-magnetic-drift frequency $\omega_{Di} = 0.266$ for ($k_x = 0$, $k_y = 0.2$). Using this value for ω_{Di} , one can evaluate Eq. 5.1 to determine the resonant mode frequency. The resonant frequency is $\omega \approx 0.724$ for ($k_x = 0$, $k_y = 0.2$). The resonant frequency calculated here is in agreement with the dominant KBM real frequency in Fig. 5.1 at $k_y = 0.2$, where $\omega_r \approx 0.72$. This constitutes quantitative evidence that the ion magnetic drift resonance is likely playing an important role in the dynamics.

5.1.5 KBMs in Heliotron-J and a small- \hat{s} tokamak

Like HSX, both Heliotron-J and a small- \hat{s} tokamak exhibit small values of $\beta_{\text{crit}}^{\text{KBM}}$ at low k_y . As evident in Fig. 5.8, a plot of linear growth rates vs. β , one observes that $\beta_{\text{crit}}^{\text{KBM}} \approx 0.14\%$ for $k_y \rho_s = 0.1$ in Heliotron-J. The gradient settings for this calculation are taken from work by A. Ishizawa et al. [16], where an analysis of turbulent transport in LHD and Heliotron-J is carried out.

A shifted-circle tokamak \hat{s} - α geometry with a low negative average magnetic shear $\hat{s} \approx -0.052$ also exhibits similar $\beta_{\text{crit}}^{\text{KBM}}$ spectra and eigenvalue characteristics to those for HSX, as shown in Fig. 5.9, where α refers to α_{MHD} , a quantity which both scales with β and indicates whether a self-consistent

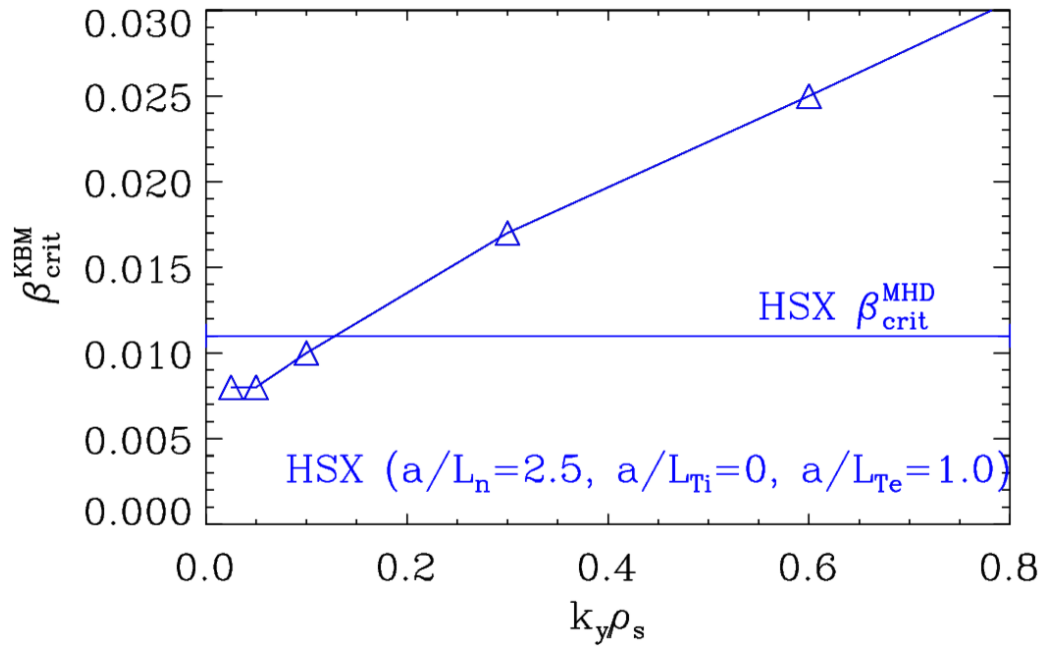


Figure 5.7: $\beta_{\text{crit}}^{\text{KBM}}$ as a function of k_y for the case where the ion temperature gradient is removed but the sum of the gradients $\omega_{Ti} + \omega_{Te} + 2\omega_n$ is kept constant. Unlike the data presented in Fig. 5.4, $\beta_{\text{crit}}^{\text{KBM}}$ does not dip to values much smaller than the MHD threshold at low k_y .

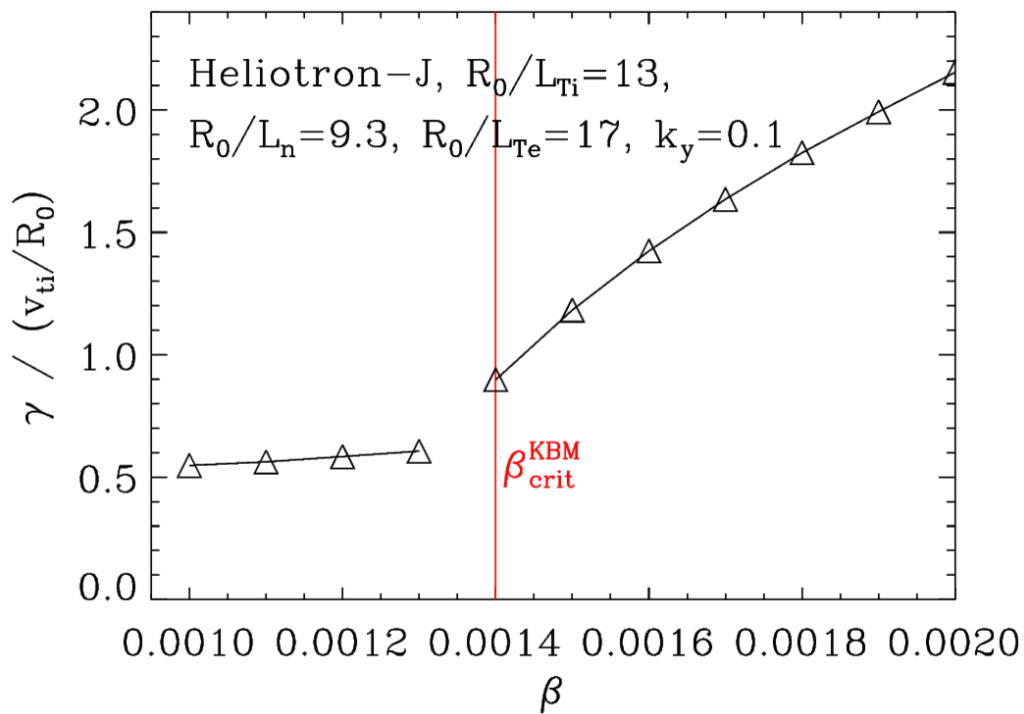


Figure 5.8: Heliotron-J, another low-magnetic-shear, three-dimensional magnetic equilibrium, also displays HSX-like KBM behavior at low k_y , as shown here in the plot of γ vs. β . Note that at this k_y , the $\beta_{\text{crit}}^{\text{KBM}}$ is roughly 0.14%.

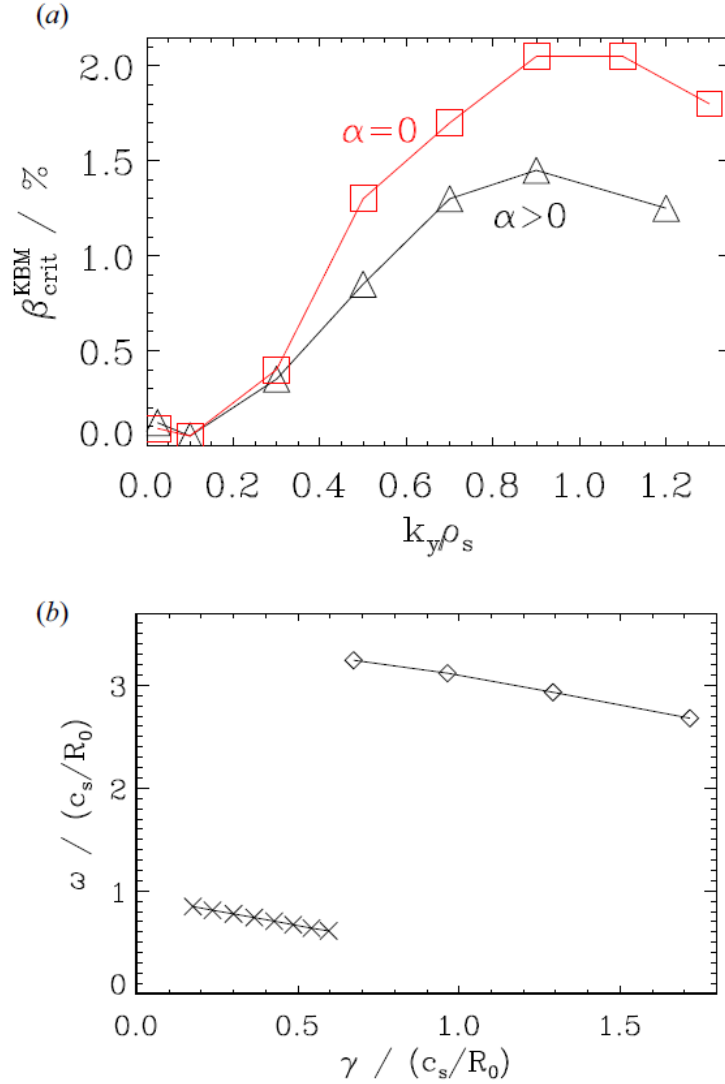


Figure 5.9: The $\beta_{\text{crit}}^{\text{KBM}}$ spectrum (a) and the subdominant-mode spectrum at $k_y = 0.2$ and $\beta = 0.8\%$ (b) for an $\hat{s} = -0.052$ circular tokamak s - α geometry in (a), there are two curves: one for the case when $\alpha_{\text{MHD}} = 0$ (red squares), where the equilibrium and dynamical β are not self-consistent; and a second for the case when α_{MHD} is such that both the equilibrium and GENE β are the same (black triangles). (b) The two distinct subdominant ITG (crosses) and KBM (diamonds) clouds are also present in the circular tokamak case. However, there is only a single KBM branch in this case versus the two that were present in HSX.

Shafranov shift is used. This is counter-intuitive since tokamaks that exhibit negative \hat{s} are ideal ballooning stable ($\beta_{\text{crit}}^{\text{MHD}} \rightarrow \infty$). Both curves are non-monotonic and have a minimum at $k_y = 0.1$ with a very small critical $\beta_{\text{crit}}^{\text{KBM}} \approx 0.1\%$, where the tokamak data is shown in the top panel of Fig. 5.9. It is also worth noting that the low- k_y behavior of $\beta_{\text{crit}}^{\text{KBM}}$ in s - α is insensitive to the inclusion of a self-consistent Shafranov shift relative to the high- k_y behavior, where there is a larger difference between $\alpha = 0$ and $\alpha > 0$. The subdominant-mode landscape for the circular tokamak is also qualitatively consistent with the HSX results, as two distinct clouds of modes are present, with both ITG and KBM branches, as shown in Fig. 5.9. However, one key difference between the subdominant-mode spectra for HSX and the circular tokamak is the presence of only a single ballooning-parity and tearing-parity KBM branch for the circular tokamak case. The single KBM branch in the axisymmetric case resembles the branch of KBMs centered at the outboard midplane for HSX.

5.2 KBM turbulence in HSX

To this point, only linear aspects of KBMs in HSX, Heliotron-J, and a small- \hat{s} circular tokamak have been shown. As mentioned previously, the small values of $\beta_{\text{crit}}^{\text{KBM}}$ at low k_y make nonlinear simulations difficult, as saturation is not always guaranteed. In GENE simulations that do not saturate, the heat flux increases without bound. Diagnosing the turbulence in a nonlinear

simulation which does not exhibit saturation, one sees strong streamer ($k_x = 0$) structures that self-reinforce through the periodic radial boundary condition. This happens regardless of how big one makes the radial extent of the flux tube domain. However, as outlined below in Figs. 5.10, 5.11, and 5.17, a time trace of electrostatic heat flux from a nonlinear simulation with $k_y^{\min} \rho_s = 0.025$ and $\beta = 0.48\%$, the associated heat flux spectrum, and a Q_{es}^i vs. β scan, respectively, it is possible to achieve nonlinear saturation so long as the smallest k_y of the system is stable to KBM.

The heat flux spectrum given in Fig. 5.11 shows that the ion electrostatic heat flux $Q_i^{\text{es}}(k_y)$ peaks in the k_y -range that is dominated by KBMs, consistent with the fact that β is roughly three times as large as $\beta_{\text{crit}}^{\text{KBM}}$ for $k_y = 0.1$. Figure 5.11 also shows that KBMs play an important role nonlinearly as long as KBMs are destabilized linearly, even if KBM growth rates are subdominant, where linear destabilization is shown in Fig. 5.1. As discussed above, k_y^{\min} is sufficiently small that no KBM instability occurs at that wavenumber; this is consistent with findings in high- \hat{s} scenarios where nonlinear saturation is possible for β values up to $\beta_{\text{crit}}^{\text{KBM}}$ as $k_y \rightarrow 0$ [17]. The nonlinear electrostatic potential Φ spectrum is shown in Fig. 5.12, showing that the simulation is not dominated by a zonal flow, as the $k_y = 0.1$ non-zonal component of Φ is nearly a factor of two larger than the zonal component and the sum of the non-zonal contributions is significantly larger than the zonal contribution. This is an indication that zonal flows may play at most a minor role in saturation. This

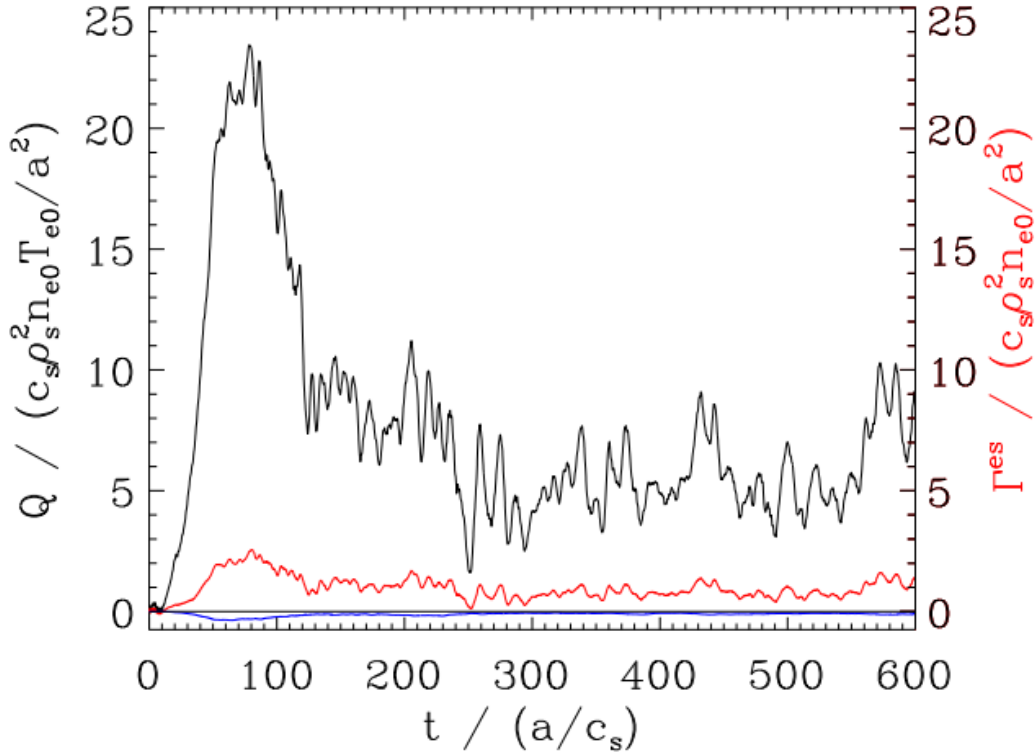


Figure 5.10: Time traces of electrostatic ion heat flux (black), electrostatic particle flux (red), and electromagnetic electron heat flux in gyro-Bohm units for HSX with $k_y^{\min} = 0.025$ and $\beta = 0.48\%$. Note that there is significant stabilization relative to the nearly-electrostatic case in Fig. 4.9, where $Q_i^{\text{es}} \approx 23$ for HSX. The small electromagnetic heat flux is due to the small electron temperature gradient, implying that electron flutter transport is small.

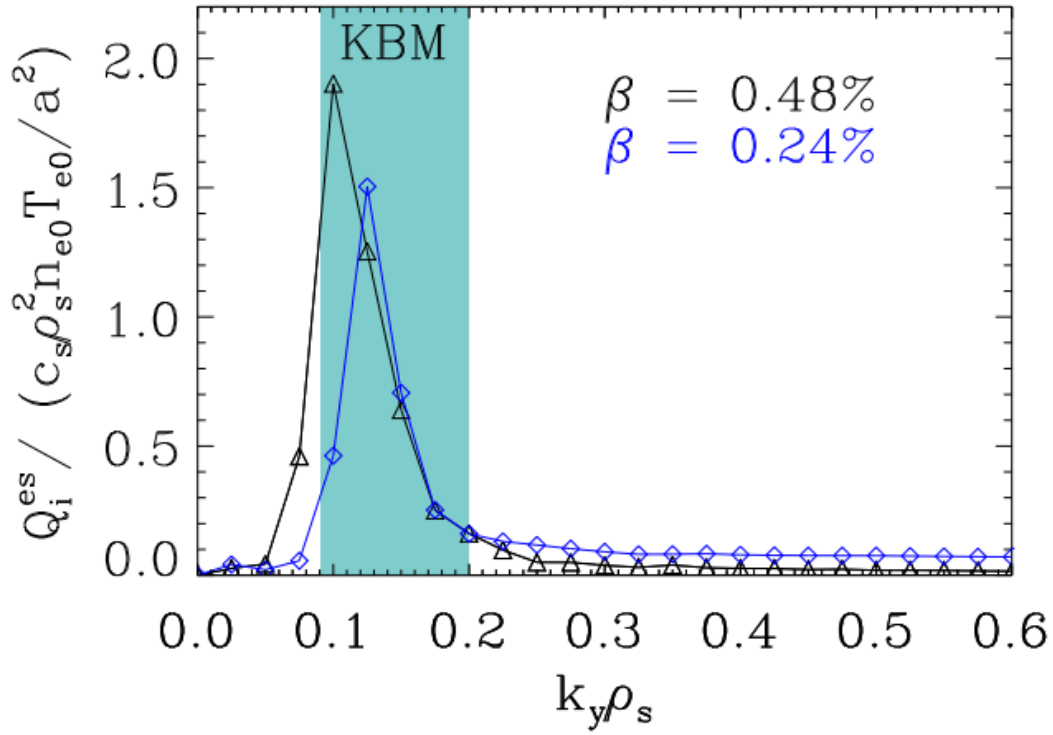


Figure 5.11: Heat flux spectra associated with the $\beta = 0.48\%$ nonlinear simulation (black) and an analogous $\beta = 0.24\%$ nonlinear simulation (blue). The shaded region corresponds to the k_y -range in which KBM is the dominant linear instability. Note that the overwhelming majority of the heat flux is due to fluctuations in the KBM-dominant k_y regime, even for $\beta = 0.24\% \approx \beta_{\text{crit}}^{\text{KBM}}(k_y = 0.1)$.

view is refined, however, based on nonlinear energy transfer analysis later in this section.

Nonlinear frequencies are shown in Fig. 5.13. Interestingly, there is no discontinuity in the nonlinear frequency spectrum of the HSX configuration, a feature that was present linearly at the ITG-KBM transition points in Fig. 5.1. Both dominant and subdominant linear KBM frequencies are overlaid in Fig. 5.13 to facilitate comparison with the nonlinear data. Clearly, throughout the range where linear data is shown, nonlinear frequency signatures match the values associated with the dominant outboard-centered KBMs, especially since ITG frequencies are much lower than KBM frequencies based on linear analysis. An exact frequency match is not expected to occur, as turbulence may result in a k_y -dependent nonlinear frequency shift and broadening. This constitutes evidence that KBMs do indeed play an important role in the nonlinear turbulent state.

Analysis of the nonlinear energy transfer to a given (k_x, k_y) point in Fourier space due to interaction with (k'_x, k'_y) and $(k_x - k'_x, k_y - k'_y)$ also suggests that modes in the KBM-dominated k_y range play an important role in the energy transfer dynamics of the turbulence and therefore in the dynamics that lead to saturation. Figure 5.14 shows nonlinear energy transfer at a given $(k_x = 0.06, k_y = 0.1)$, denoted by the tip of the black arrow, to and from various (k'_x, k'_y) . Regions of blue correspond to locations which cause energy input into $(k_x = 0.06, k_y = 0.1)$ while red regions correspond to locations which draw

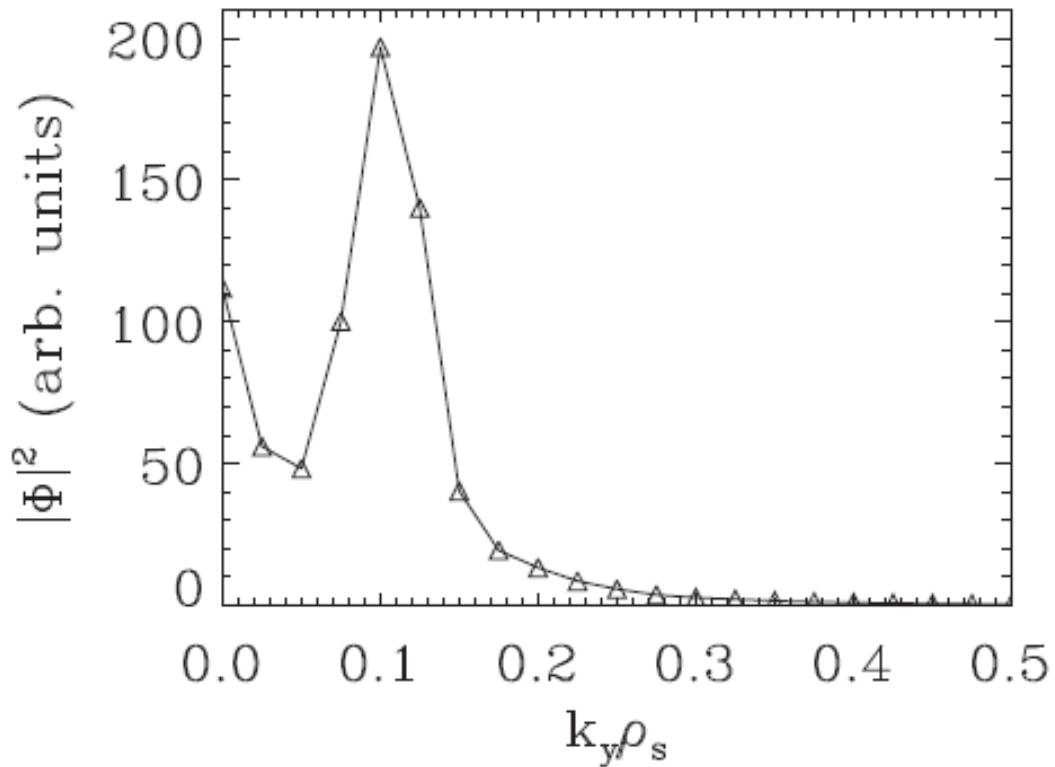


Figure 5.12: The nonlinear Φ spectrum for HSX with $k_y^{\min} = 0.025$ and $\beta = 0.48\%$. The spectrum is truncated at $k_y \rho_s = 0.5$ since $|\Phi|^2$ amplitudes are negligible above this threshold. Note that the zonal component is much weaker than the integrated non-zonal amplitudes, and also weaker than the peak amplitude.

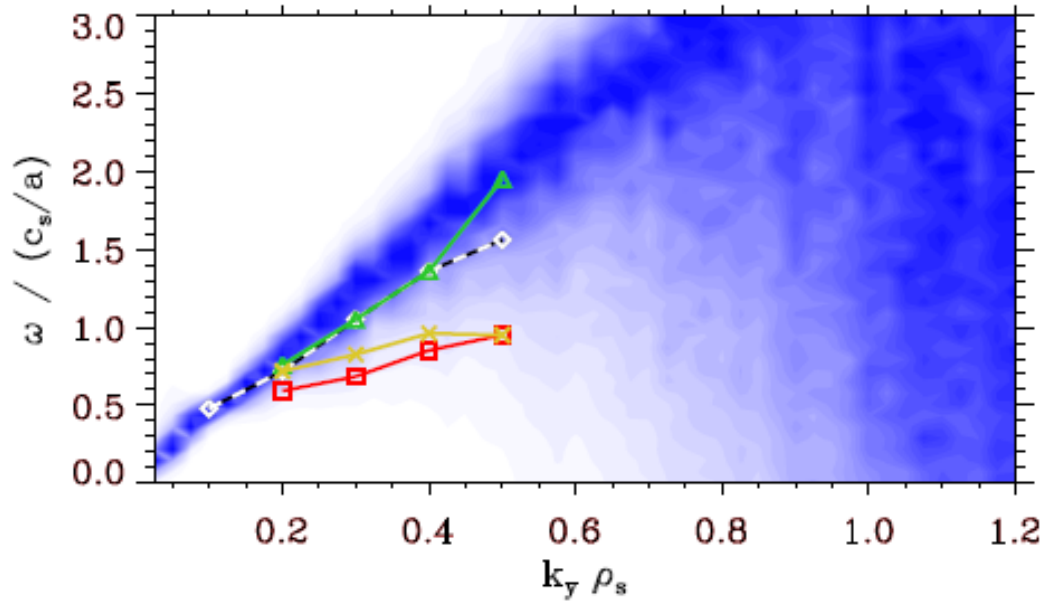


Figure 5.13: The nonlinear frequency spectrum for HSX with $k_y^{\min} = 0.025$ and $\beta = 0.48\%$. The color scale has arbitrary units and is linear and normalized at each k_y separately. Linear frequencies of the most unstable (gold crosses), maximal-frequency (green triangles), minimal-frequency (red squares), and most unstable outboard-centered (black-white dashed diamonds) KBMs are also included for comparison. The dominant linear outboard-centered KBM frequencies match the nonlinear signal very well.

energy from $(k_x = 0.06, k_y = 0.1)$. The dominant method by which $(k_x = 0.06, k_y = 0.1)$ receives energy is zonal energy transfer, indicated by the blue clouds at both $k'_y = 0$ and $k'_y = 0.1$. There is also significant non-zonal energy transfer via $(k'_x = 0.12, k'_y = -0.025)$. It is important to note both that the largest energy sinks are due to non-zonal transfer and that the largest energy sinks are even larger than the largest energy inputs from zonal transfer. This result appears to contradict the earlier finding in Fig. 5.12 that the zonal-flow amplitudes are low. However, when coupling is sufficiently resonant, zonal flows can very efficiently mediate energy transfer even if they are only excited to low amplitudes.

Further analysis of nonlinear energy transfer yields insight into the wavelength ranges which dominate energy transfer between the turbulence and the zonal ($k_y = 0$) modes. Fig. 5.15 shows normalized nonlinear energy transfer corresponding to $k_y = 0$ modes summed over both k_x and k'_x versus k'_y . The peak of the data occurs at $k'_y = 0.125$, well within the KBM-dominated k_y -range. A significant portion of the energy transfer to and from zonal modes is facilitated by modes in the KBM-dominated k_y -range, constituting additional evidence that KBMs are important nonlinearly. One can also construct a quantity to gauge the relative importance of a given k_y in the overall nonlinear energy transfer dynamics, as highlighted by Fig. 5.16, a plot of averaged nonlinear energy transfer functions versus k_y . This quantity is the sum (over $k_x \neq 0$) of the root-mean-squares (of each k'_x - k'_y plane) of the nonlinear energy

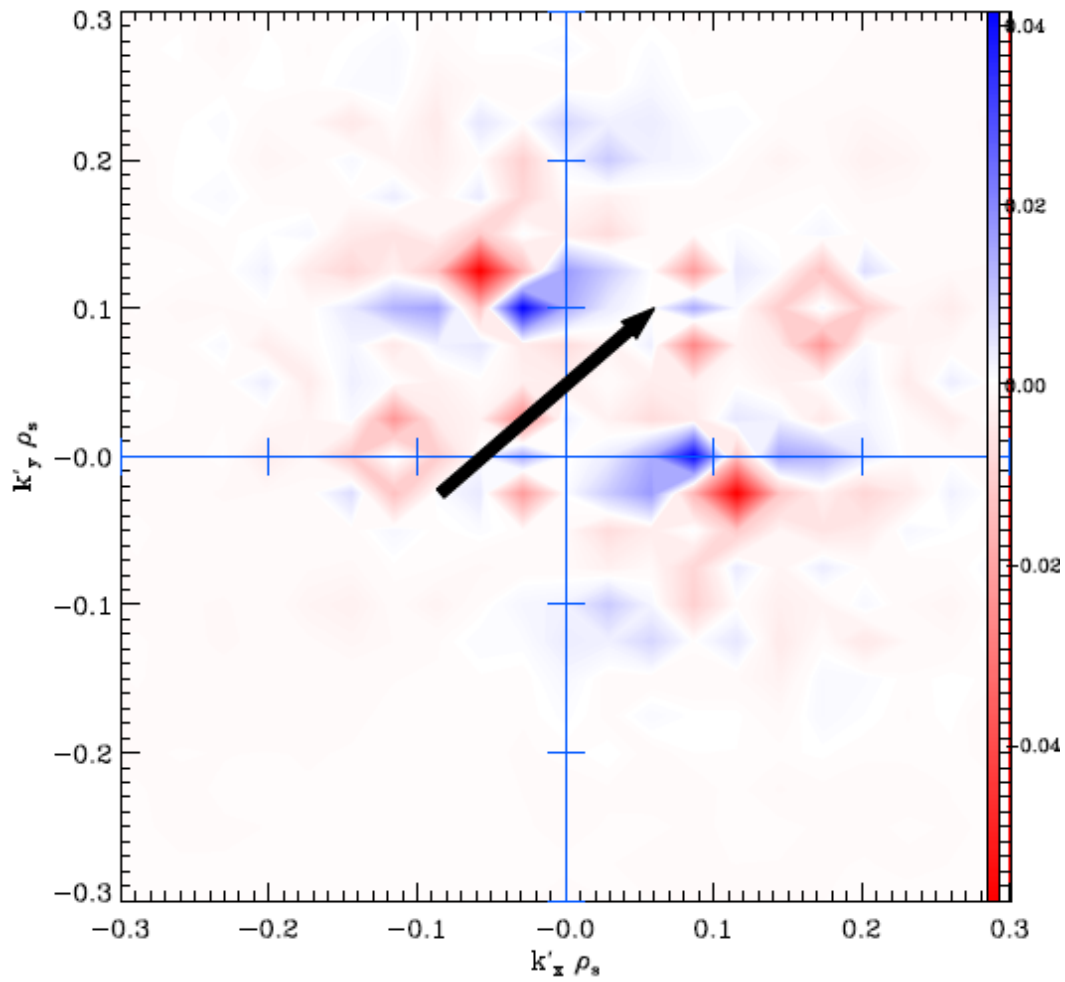


Figure 5.14: Nonlinear energy transfer functions indicate locations which give (blue) and receive (red) energy to and from $(k_x = 0.06, k_y = 0.1)$, denoted by the tip of the black arrow. There is significant zonal transfer from $(k_x = 0.06, k_y = 0.1)$ to the blue clouds near $k'_y = 0$ and $k'_y = 0.1$. Significant non-zonal energy transfer is also observed at $k'_y = -0.025$ and $k'_y = 0.125$.

transfer functions corresponding to a given (k_x, k_y) . Both the zonal modes and non-zonal KBMs contribute to the overall nonlinear energy transfer dynamics, with KBMs contributing at least as much as the zonal modes if one integrates over the entire KBM-dominated k_y -range and accounts for ITG contributions in the KBM-dominated k_y -range.

Lastly, Fig. 5.17 shows both the electrostatic ion heat and particle fluxes as β increases. Simulations with $k_y^{\min} = 0.025$ for $\beta = 0.75\%$ and 1% grow without bounds and therefore do not have associated data points. This is consistent with the requirement that k_y^{\min} be stable to KBMs for saturation to occur, as $\beta_{\text{crit}}^{\text{KBM}} \approx 0.6\%$ for $k_y = 0.025$, as shown in Fig. 5.4. Note the decrease in heat flux as β increases until β is sufficiently close to $\beta_{\text{crit}}^{\text{KBM}}(k_y^{\min})$, a result that is consistent with ITG nonlinear finite- β stabilization [10]. The uptick in Q_i^{es} as β increases from 0.48% to 0.55% is an expression of the KBMs, which, unlike the ITG modes, become more virulent as β is increased.

5.3 The five-field model

As previously alluded to, the five-field model will aid in the study of KBM turbulence saturation in magnetic equilibria that exhibit low magnetic shear. As demonstrated by gyrokinetic simulations above, HSX, a circular tokamak, and Heliotron-J, three low-magnetic-shear configurations, exhibit poor linear KBM properties which affect nonlinear saturation. Building a physical intuition regarding the relationship between magnetic geometry and small $\beta_{\text{crit}}^{\text{KBM}}$ is

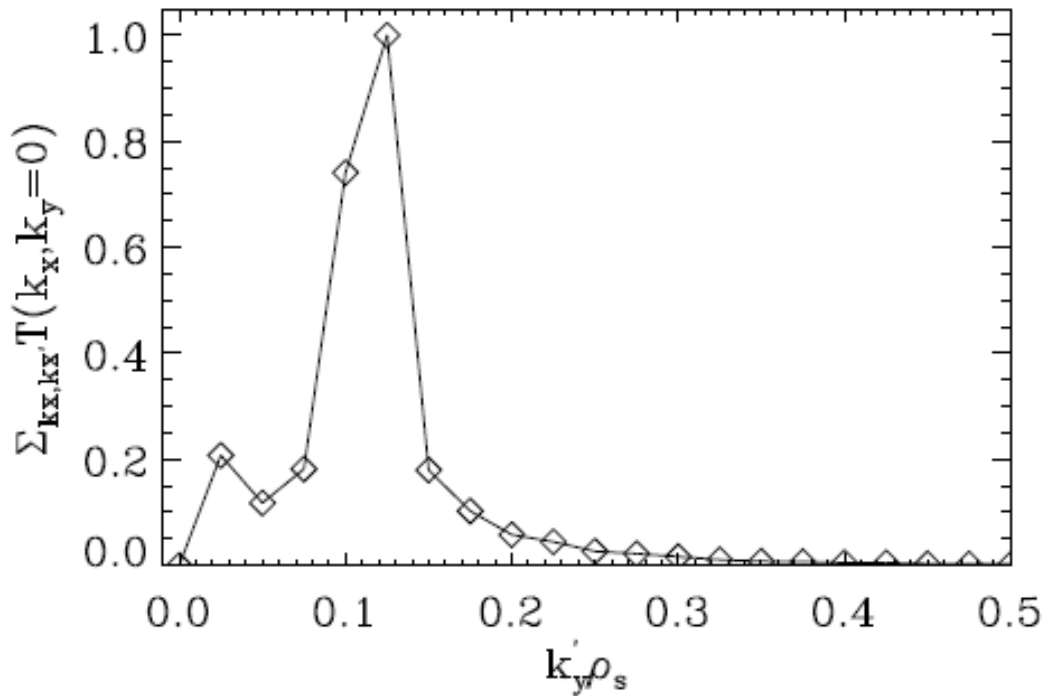


Figure 5.15: The sum (over $k_x \neq 0$) of the root-mean-squares (over coupled k'_x) of time-averaged nonlinear energy transfer functions for zonal ($k_y = 0$) modes as a function of k'_y . The data is normalized to the value of the point at $k'_y = 0.125$ so that the maximal value is one for ease of comparison. Note that the peak is in the KBM-dominated k'_y -range, evidence that KBMs play an important role in zonal dynamics.

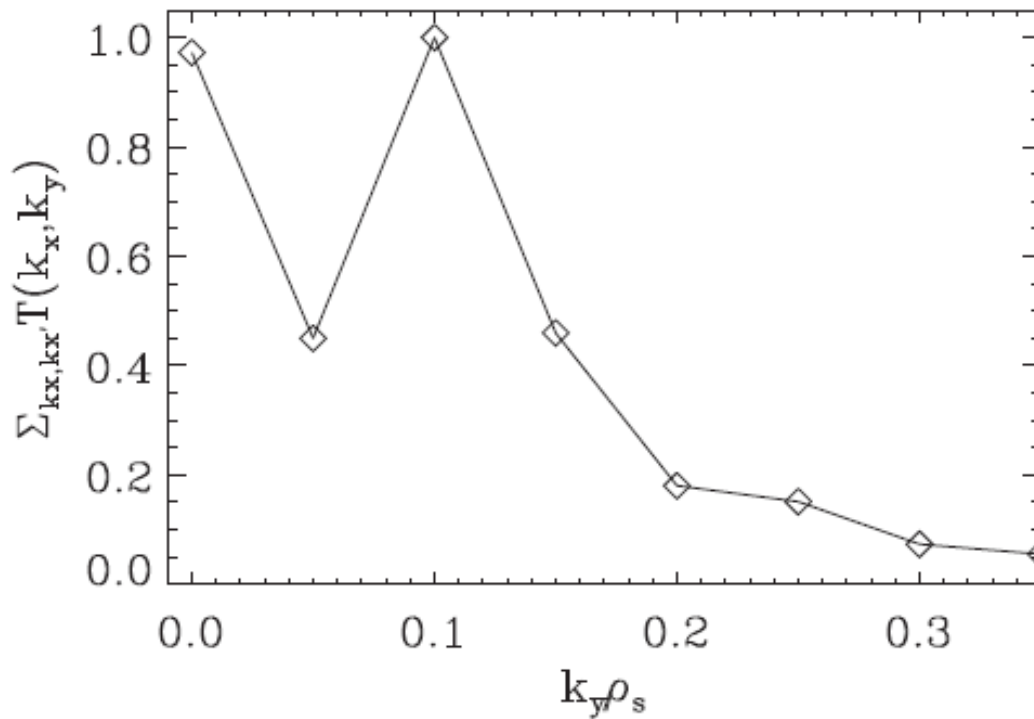


Figure 5.16: The sum (over $k_x \neq 0$) of the root-mean-squares (over coupled k'_x, k'_y) of time-averaged nonlinear energy transfer functions, which are normalized by the value of the same quantity at $k_y = 0.1$ for ease of comparison. The primary conclusion to be derived from this figure is that KBMs likely play an equal or greater role than the zonal modes in nonlinear energy transfer. Additional analysis of specific triplet interactions is necessary to tease out the precise ratio of the respective contributions of KBMs and zonal modes.

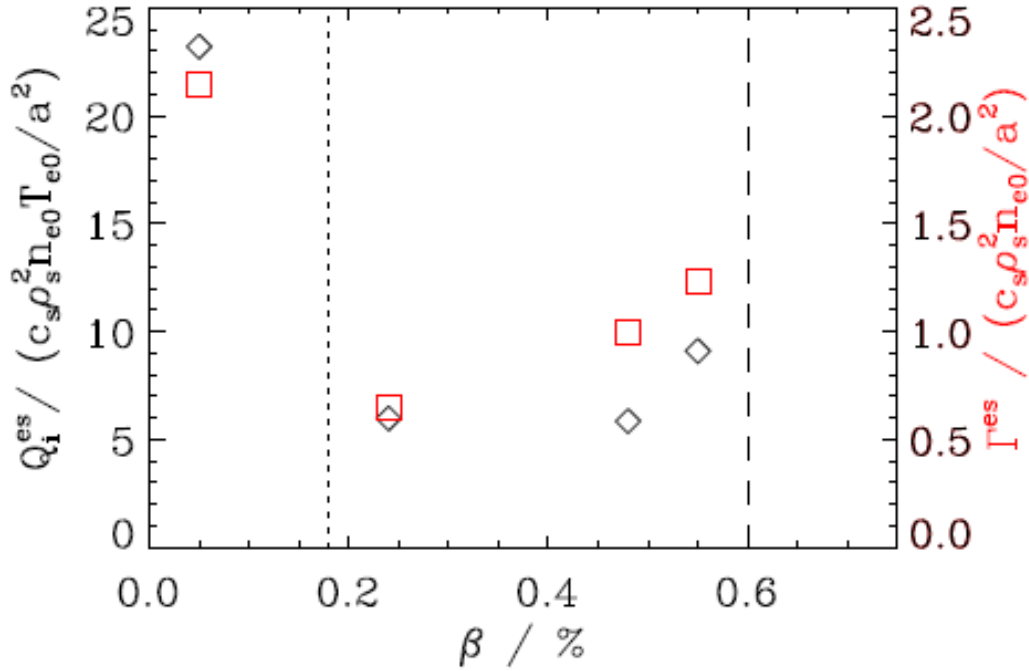


Figure 5.17: Normalized ion heat flux Q_i^{es} (black diamonds) and particle flux Γ^{es} (red squares) as a function of β . Observe the significant reduction of transport for $\beta \gtrsim 0.2\%$ relative to $\beta \approx 0.05\%$ until β approaches the $\beta_{\text{crit}}^{\text{KBM}} \approx 0.6\%$ threshold for $k_y = 0.025$. Above $\beta = 0.6\%$, simulations no longer achieve a saturated state. A vertical dashed black line indicates $\beta_{\text{crit}}^{\text{KBM}} = 0.6\%$ at $k_y = 0.025$ and a vertical dotted black line indicates the $\beta_{\text{crit}}^{\text{KBM}} = 0.18\%$ at $k_y = 0.1$. The electron electromagnetic heat flux is negligible (normalized $Q_e^{\text{em}} \approx -0.2$ for $\beta = 0.48\%$) and therefore not included.

a driving motivation for this model. The ion equations in the model are taken from Ref. [1] and augmented with the analogous electron equations, with the exception of an electron energy equation, for which the closure equation is substituted.

The model consists of seven equations, five of which are dynamical, in seven unknowns, \tilde{T}_e , \tilde{n}_i , \tilde{A}_{\parallel} , \tilde{T}_i , $\tilde{\phi}$, $\tilde{v}_{\parallel i}$, and $\tilde{v}_{\parallel e}$. Dissipative terms are omitted here for simplicity. The set of equations given below consists of the continuity and parallel momentum equations for both ions and electrons, an ion energy equation, an equation describing infinite parallel electron thermal conduction to close the system, and Ampère's Law:

$$\frac{\partial n_i}{\partial t} + \nabla \cdot (n_i \mathbf{v}_E + n_i \mathbf{v}_{i\star}) + \nabla \cdot (n_i \mathbf{v}_{pi} + n_i \mathbf{v}_{\pi i}) + (\mathbf{B} \cdot \nabla) \left(n_i \frac{v_{\parallel i}}{B} \right) = 0 \quad (5.3)$$

$$m_i n_i \frac{dv_{\parallel i} B}{dt} + B q n_i \frac{\partial A_{\parallel}}{\partial t} + (\mathbf{B} \cdot \nabla) (q n_i \phi + p_i) + \mathbf{B} \cdot (\nabla \cdot \pi)_{\text{gyro},i} = 0 \quad (5.4)$$

$$\frac{3}{2} n_i \frac{dT_i}{dt} + n_i T_i \nabla \cdot \mathbf{v}_i + \nabla \cdot \mathbf{q}_{Di} = 0 \quad (5.5)$$

$$\frac{\partial n_e}{\partial t} + \nabla \cdot (n_e \mathbf{v}_E + n_e \mathbf{v}_{e\star}) + \nabla \cdot (n_e \mathbf{v}_{pe} + n_e \mathbf{v}_{\pi e}) + (\mathbf{B} \cdot \nabla) \left(n_e \frac{v_{\parallel e}}{B} \right) = 0 \quad (5.6)$$

$$m_e n_e \frac{dv_{\parallel e} B}{dt} + B q n_e \frac{\partial A_{\parallel}}{\partial t} + (\mathbf{B} \cdot \nabla) (q n_e \phi + p_e) + \mathbf{B} \cdot (\nabla \cdot \pi)_{\text{gyro},e} = 0 \quad (5.7)$$

$$(\mathbf{B} \cdot \nabla) T_e = 0 \quad (5.8)$$

$$\mathbf{B} \cdot (\nabla \times \mathbf{B}) = \mu_0 (\mathbf{B} \cdot \mathbf{J}) = \mu_0 n_i B e (v_{\parallel i} - v_{\parallel e}). \quad (5.9)$$

where $\mathbf{v}_E = \mathbf{B} \times \nabla \phi / B^2$ is the $\mathbf{E} \times \mathbf{B}$ flow, $\mathbf{v}_{i\star} = \mathbf{B} \times \nabla p_i / (n_i e B^2)$ is the ion diamagnetic flow, the ion polarization drift and gyro-viscosity give $\nabla \cdot (n_i \mathbf{v}_{pi} +$

$n_i \mathbf{v}_{\pi i}) = -\nabla \cdot [n_i m_i / (eB^2) (\partial / \partial t + \mathbf{v}_E \cdot \nabla) (\nabla \phi + 1 / (n_e e) \nabla p_i)]$, and the ion diamagnetic heat flux is $\mathbf{q}_{Di} = 5p_i / (2eB^2) \mathbf{B} \times \nabla T_i$.

The goal of the following subsections is to simplify each equation of the model by substituting the appropriate expressions for the various drift terms and carrying out any cancellations. At the end of the simplification process, a set of normalized variables is introduced and then incorporated into the equations. The final result of this section will be a set of seven equations in seven unknowns which can then be solved numerically for the five eigenmodes (which come from the five dynamical equations) by solving an eigenvalue equation. Those five modes will consist of two stable, two unstable, and one marginally stable mode. Investigation of the coupling and energy transfer between those various modes in different magnetic geometries and determining how such quantities scale with magnetic shear, ion temperature gradient, etc. will be of particular interest for the future work of this research.

5.3.1 Ion continuity equation

Beginning with Eq. (5.1):

$$\frac{\partial n_i}{\partial t} + \nabla \cdot (n_i \mathbf{v}_E + n_i \mathbf{v}_{i*}) + \nabla \cdot (n_i \mathbf{v}_{pi} + n_i \mathbf{v}_{\pi i}) + (\mathbf{B} \cdot \nabla) \left(n_i \frac{v_{\parallel i}}{B} \right) = 0, \quad (5.10)$$

which, after substitutions for \mathbf{v}_{i*} , \mathbf{v}_{pi} , and $\mathbf{v}_{\pi i}$ are inserted, yields the following equation:

$$\begin{aligned}
\frac{\partial n_i}{\partial t} + \mathbf{v}_E \cdot \nabla n_i + n_i \left(\frac{e}{T_i} \mathbf{v}_{Di} \cdot \nabla \phi \right) + \frac{1}{T_i} \mathbf{v}_{Di} \cdot \nabla p_i - \nabla \cdot \left(\frac{n_i m_i}{e B^2} \left(\frac{\partial}{\partial t} \dots \right. \right. \\
\left. \left. + \mathbf{v}_E \cdot \nabla \right) \left(\nabla \phi + \frac{1}{n_i e} \nabla p_i \right) \right) + \mathbf{B} \cdot \nabla \left(n_i \frac{v_{\parallel i}}{B} \right) = 0,
\end{aligned} \tag{5.11}$$

where \mathbf{v}_{Di} is taken to be:

$$\mathbf{v}_{Di} = \frac{T_i}{e B^2} \left(\frac{\mathbf{B} \times \nabla B}{B} + \mathbf{B} \times \vec{\kappa} \right), \tag{5.12}$$

where $\vec{\kappa}$ is the curvature given by $\vec{\kappa} = (\hat{\mathbf{b}} \cdot \nabla) \hat{\mathbf{b}}$. Additionally, ∇B can be written as

$$\nabla B = B \vec{\kappa} - \frac{\mu_0}{B} \nabla p + \mathbf{B} \left(\frac{\mathbf{B} \cdot \nabla B}{B^2} \right) \tag{5.13}$$

via MHD force balance, where $p = p_i + p_e$ is the total pressure. Also note that the $\mathbf{B} \times \nabla p \cdot \nabla p_i$ simplifies to $\mathbf{B} \times \nabla p_e \cdot \nabla p_i$. For the purposes of evaluating low- β (on the order of a few percent) electromagnetic turbulence in toroidal confinement systems, the $\nabla p/B \sim \beta$ term in Eq. 5.11 can be neglected relative to the $\vec{\kappa}$ term. Plugging \mathbf{v}_{Di} and \mathbf{v}_E into Eq. (5.9) gives the following:

$$\begin{aligned}
\frac{\partial n_i}{\partial t} + \frac{\mathbf{B} \times \nabla \phi}{B^2} \cdot \nabla n_i + \frac{n_i}{B^2} \left(2\mathbf{B} \times \vec{\kappa} \right) \cdot \nabla \phi + \frac{1}{e B^2} \left(2\mathbf{B} \times \vec{\kappa} \right) \cdot \nabla p_i - \dots \\
\nabla \cdot \left(\frac{n_i m_i}{e B^2} \left(\frac{\partial}{\partial t} + \frac{\mathbf{B} \times \nabla \phi}{B^2} \cdot \nabla \right) \left(\nabla \phi + \frac{1}{n_i e} \nabla p_i \right) \right) + \mathbf{B} \cdot \nabla \left(n_i \frac{v_{\parallel i}}{B} \right) = 0.
\end{aligned} \tag{5.14}$$

Linearizing Eq. (5.12) gives:

$$\begin{aligned}
\frac{\partial \tilde{n}_i}{\partial t} + \frac{\mathbf{B}_0 \times \nabla \tilde{\phi}}{B_0^2} \cdot \nabla n_{i0} + \frac{n_{i0}}{B_0^2} \left(2\mathbf{B}_0 \times \vec{\kappa}_0 \right) \cdot \nabla \tilde{\phi} + \frac{1}{eB_0^2} \left(2\mathbf{B}_0 \times \vec{\kappa}_0 \right) \cdot \nabla \tilde{p}_i \cdots \\
- \nabla \cdot \left(\frac{n_{i0} m_i}{eB_0^2} \left(\frac{\partial}{\partial t} \left(\nabla \tilde{\phi} + \frac{1}{n_{i0} e} \nabla \tilde{p}_i \right) \right) \right) + \mathbf{B}_0 \cdot \nabla \left(n_{i0} \frac{\tilde{v}_{\parallel i}}{B_0} \right) = 0.
\end{aligned} \tag{5.15}$$

Making substitutions for $\nabla \rightarrow ik_{\perp}$, when ∇ is operating on a fluctuating quantity, in Eq. (5.13), we arrive at the following (leaving ∂_t terms in for now):

$$\begin{aligned}
\partial_t \tilde{n}_i + \frac{i\mathbf{B}_0 \times \mathbf{k}_{\perp} \tilde{\phi}}{B_0^2} \cdot \nabla n_{i0} + \frac{in_{i0}}{B_0^2} \left(2\mathbf{B}_0 \times \vec{\kappa}_0 \right) \cdot \mathbf{k}_{\perp} \tilde{\phi} - \cdots \\
+ \frac{i}{eB_0^2} \left(2\mathbf{B}_0 \times \vec{\kappa}_0 \right) \cdot \mathbf{k}_{\perp} \tilde{p}_i + \cdots \\
\partial_t \frac{k_{\perp}^2 n_{i0} m_i}{eB_0^2} \left(\tilde{\phi} + \frac{1}{n_{i0} e} \tilde{p}_i \right) + \nabla_{\parallel} \left(n_{i0} \frac{\tilde{v}_{\parallel i}}{B_0} \right) = 0.
\end{aligned} \tag{5.16}$$

Next, making use of the following simplifications:

$$(\mathbf{B}_0 \times \mathbf{k}_{\perp}) \cdot \nabla \rho = -k_{\alpha} \frac{B_0^2}{\psi'}, \tag{5.17}$$

$$\frac{(\mathbf{B}_0 \times \vec{\kappa}_0) \cdot \mathbf{k}_{\perp}}{B_0^2} = (\psi' |\nabla \rho|)^{-1} \left(k_{\alpha} (\kappa_n + \Lambda \kappa_g) - k_{\rho} \frac{g^{\rho\rho} \psi'}{B_0} \kappa_g \right), \tag{5.18}$$

$$\nabla \rho \cdot (\mathbf{B}_0 \times \vec{\kappa}) = - \left(\frac{\nabla_{\parallel} B_0}{B_0^2} i \tilde{A}_{\parallel} (k_{\rho} g^{\rho\rho} + k_{\alpha} g^{\rho\alpha}) \right), \tag{5.19}$$

yields the following equation:

$$\begin{aligned}
\partial_t \tilde{n}_i - i \frac{k_{\alpha}}{\psi'} \frac{\partial n_{i0}}{\partial \rho} \tilde{\phi} + i \left(\frac{2}{\psi' |\nabla \rho|} (k_{\alpha} (\kappa_n + \Lambda \kappa_g) - k_{\rho} \frac{g^{\rho\rho} \psi'}{B_0} \kappa_g) \right) \left(n_{i0} \tilde{\phi} + \frac{\tilde{p}_i}{e} \right) + \cdots \\
\partial_t \frac{k_{\perp}^2 n_{i0} m_i}{eB_0^2} \left(\tilde{\phi} + \frac{\tilde{p}_i}{n_{i0} e} \right) + \nabla_{\parallel} \left(n_{i0} \frac{\tilde{v}_{\parallel i}}{B_0} \right) = 0.
\end{aligned} \tag{5.20}$$

This is an equation involving four fluctuating quantities: $\tilde{\phi}$, \tilde{n}_i , $\tilde{v}_{\parallel i}$, and \tilde{T}_i .

5.3.2 Ion parallel momentum

First, taking the parallel ion momentum equation:

$$m_i n_i \frac{dv_{\parallel i} B}{dt} + B q n_i \frac{\partial A_{\parallel}}{\partial t} + (\mathbf{B} \cdot \nabla)(q n_i \phi + p_i) + \mathbf{B} \cdot (\nabla \cdot \pi)_{\text{gyro}} = 0, \quad (5.21)$$

which, after applying the gyroviscous cancellation, gives the following equation:

$$B m_i n_i \partial_t v_{\parallel i} + B e n_i \partial_t A_{\parallel} + m_i n_i (\mathbf{v}_E \cdot \nabla)(v_{\parallel i} B) + \nabla_{\parallel}(e n_i \phi + p_i) = 0. \quad (5.22)$$

Next, after linearizing and taking the equilibrium parallel ion flow to be zero:

$$m_i n_{i0} B_0 \partial_t \tilde{v}_{\parallel i} + B_0 e n_{i0} \partial_t \tilde{A}_{\parallel} + (\tilde{\mathbf{B}} \cdot \nabla) p_{i0} + \nabla_{\parallel}(e n_{i0} \tilde{\phi} + \tilde{p}_i) = 0. \quad (5.23)$$

This is the same as the three-field model analog with the exception of the \tilde{A}_{\parallel} terms. $(\tilde{\mathbf{B}} \cdot \nabla) p_{i0} = \tilde{\nabla}_{\parallel} p_{i0}$ can be further simplified:

$$m_i n_{i0} B_0 \partial_t \tilde{v}_{\parallel i} + B_0 e n_{i0} \partial_t \tilde{A}_{\parallel} + \frac{\partial p_{i0}}{\partial \rho} \frac{i k_{\alpha} \tilde{A}_{\parallel} B_0}{\psi'} + \nabla_{\parallel}(e n_{i0} \tilde{\phi} + \tilde{p}_i) = 0. \quad (5.24)$$

5.3.3 Ion energy equation

The ion energy equation, Eq. (5.3), with $\nabla \cdot \mathbf{q}_{Di} = -\frac{5}{2}n_i \mathbf{v}_{*i} \cdot \nabla T_i + \frac{5}{2}n_i \mathbf{v}_{Di} \cdot \nabla T_i$ and the continuity equation to simplify $\nabla \cdot \mathbf{v}_i$, becomes the following:

$$\frac{3}{2}n_i \frac{dT_i}{dt} - T_i \frac{dn_i}{dt} + \frac{5}{2}n_i \mathbf{v}_{Di} \cdot \nabla T_i - \frac{5}{2}n_i \mathbf{v}_{*i} \cdot \nabla T_i = 0, \quad (5.25)$$

where the \mathbf{v}_{*i} components of the total time derivatives cancel and the ion energy equation can then be written as:

$$\begin{aligned} n_i \frac{\partial T_i}{\partial t} + n_i (\mathbf{v}_E \cdot \nabla) T_i - \frac{2}{3} T_i \frac{\partial n_i}{\partial t} - \frac{2}{3} T_i (\mathbf{v}_E \cdot \nabla) n_i + \dots \\ \frac{10}{3} \frac{p_i}{eB^2} (\mathbf{B} \times \vec{\kappa}) \cdot \nabla T_i = 0. \end{aligned} \quad (5.26)$$

After linearizing and taking $\nabla \rightarrow i\mathbf{k}_\perp$, we arrive at the following:

$$\begin{aligned} n_{i0} \partial_t \tilde{T}_i + in_{i0} \frac{\mathbf{B}_0 \times \mathbf{k}_\perp}{B_0^2} \cdot \nabla \rho \frac{\partial T_{i0}}{\partial \rho} \tilde{\phi} - \frac{2T_{i0}}{3} \partial_t \tilde{n}_i - \dots \\ \frac{2iT_{i0}}{3} \frac{\mathbf{B}_0 \times \mathbf{k}_\perp}{B_0^2} \cdot \nabla \rho \frac{\partial n_{i0}}{\partial \rho} \tilde{\phi} + \frac{10ip_{i0}}{3eB_0^2} (\mathbf{B}_0 \times \vec{\kappa}_0) \cdot \mathbf{k}_\perp \tilde{T}_i = 0. \end{aligned} \quad (5.27)$$

Next, simplifying various terms leads to:

$$\begin{aligned} n_{i0} \partial_t \tilde{T}_i - in_{i0} \frac{k_\alpha}{\psi'} \frac{\partial T_{i0}}{\partial \rho} \tilde{\phi} - \frac{2}{3} T_{i0} \partial_t \tilde{n}_i + \frac{2}{3} iT_{i0} \frac{k_\alpha}{\psi'} \frac{\partial n_{i0}}{\partial \rho} \tilde{\phi} + \dots \\ \frac{5}{3} \frac{ip_{i0}}{e} \left(\frac{2}{\psi' |\nabla \rho|} \left(k_\alpha (\kappa_n + \Lambda \kappa_g) - k_\rho \frac{g^{\rho\rho} \psi'}{B_0} \kappa_g \right) \right) \tilde{T}_i = 0. \end{aligned} \quad (5.28)$$

5.3.4 Electron continuity equation

The electron continuity equation is simpler than the ion continuity equation since electron inertia terms can be neglected (e.g., $\nabla \cdot (n_e \mathbf{v}_{pe} + n_e \mathbf{v}_{\pi e}) \propto m_e \rightarrow 0$):

$$\partial_t n_e + \nabla \cdot (n_e \mathbf{v}_E + n_e \mathbf{v}_{e\star}) + (\mathbf{B} \cdot \nabla) \left(n_e \frac{v_{\parallel e}}{B} \right) = 0. \quad (5.29)$$

Using the same approach employed in Sec. 5.3.1, in addition to quasi-neutrality ($n_i \approx n_e$), the electron continuity equation simplifies to the following:

$$\partial_t n_i + \mathbf{v}_E \cdot \nabla n_i + \frac{1}{B^2} (2\mathbf{B} \times \vec{\kappa}) \cdot \left(n_i \nabla \phi - \frac{\nabla p_e}{e} \right) + (\mathbf{B} \cdot \nabla) \left(n_i \frac{v_{\parallel e}}{B} \right) = 0. \quad (5.30)$$

After linearizing and making substitutions similar to what was done for the ion continuity equation, one arrives at the following form of the electron continuity equation:

$$\begin{aligned} \partial_t \tilde{n}_i - \frac{ik_\alpha}{\psi'} \frac{\partial n_{i0}}{\partial \rho} \tilde{\phi} + \left(\frac{2i}{\psi' |\nabla \rho|} \left(k_\alpha (\kappa_n + \Lambda \kappa_g) - \dots \right. \right. \\ \left. \left. k_\rho \frac{g^{\rho\rho} \psi'}{B_0} \kappa_g \right) \right) \left(n_{i0} \tilde{\phi} - \frac{\tilde{p}_e}{e} \right) + \nabla_{\parallel} \left(n_{i0} \frac{\tilde{v}_{\parallel e}}{B_0} \right) = 0. \end{aligned} \quad (5.31)$$

5.3.5 Electron parallel momentum equation

$$-B_0 e n_{i0} \partial_t \tilde{A}_{\parallel} - \nabla_{\parallel} (e n_{i0} \tilde{\phi}) + T_{e0} \nabla_{\parallel} \tilde{n}_i + T_{e0} \frac{\partial n_{i0}}{\partial \rho} \frac{i k_{\alpha} \tilde{A}_{\parallel} B_0}{\psi'} = 0. \quad (5.32)$$

The main differences here relative to the ion parallel momentum equation are that the closure equation, $(\mathbf{B} \cdot \nabla) T_e = 0$, simplifies the $(\mathbf{B} \cdot \nabla) p_e$ term and the electron inertia terms are discarded.

5.3.6 Closing the system

An equation governing electron parallel thermal conduction:

$$\nabla_{\parallel} \tilde{T}_e + \frac{\partial T_{e0}}{\partial \rho} \frac{i k_{\alpha} \tilde{A}_{\parallel} B_0}{\psi'} = 0. \quad (5.33)$$

This equation, coupled with ion continuity, parallel momentum, energy, electron continuity, electron parallel momentum, and Ampère's law (to relate $\tilde{v}_{\parallel i}$ and $\tilde{v}_{\parallel e}$):

$$\tilde{v}_{\parallel i} - \tilde{v}_{\parallel e} = \frac{k_{\perp}^2}{\mu_0 n_{i0} e} \tilde{A}_{\parallel}, \quad (5.34)$$

comprise a system of seven equations in seven unknowns that can be solved to study finite- β linear KBM physics in low-magnetic-shear magnetic equilibria. One can retain the dominant nonlinear terms (the $\mathbf{E} \times \mathbf{B}$ and electron flutter nonlinearities) to extend linear studies to nonlinear dynamics.

Next, a continuation of the derivation will be shown where normalized quantities are introduced and equations are converted into a form such that they can be easily compared with the three-field model.

5.3.7 Normalized variables

The following will be used for normalized variables Φ , n_i , T_i , T_e , A_{\parallel} , U_i , and U_e :

$$\begin{aligned}
T_i &= \frac{\tilde{T}_i}{T_{e0}\rho^*} \\
\Phi &= \frac{e\tilde{\phi}}{T_{e0}\rho^*} \\
U_i &= \frac{\tilde{v}_{\parallel i}}{c_s\rho^*} \\
T_e &= \frac{\tilde{T}_e}{T_{e0}\rho^*} \\
n_i &= \frac{\tilde{n}_i}{n_{i0}\rho^*} \\
U_e &= \frac{\tilde{v}_{\parallel e}}{c_s\rho^*} \\
A_{\parallel} &= \frac{c_s e}{T_{e0}\rho^*} \tilde{A}_{\parallel}
\end{aligned} \tag{5.35}$$

Rewriting the ion continuity equation with the above normalizations, substituting for k_{α} and k_{ρ} , normalizing $\partial_t \rightarrow \tau^{-1}\partial_t$ and $\nabla_{\parallel} \rightarrow (L_{\text{eq}}/B_0)\mathbf{B} \cdot \nabla$, and writing gradients in terms of ω_n , ω_{Ti} , and ω_{Te} gives the following:

$$\begin{aligned}
& \frac{n_{i0}\rho^*}{\tau} \partial_t n_i + \frac{ik_y n_{i0} \omega_n}{\rho^* \psi' L_{eq}} \frac{\rho^* T_{e0} \Phi}{e} + \frac{B_0}{L_{eq}} \nabla_{\parallel} \left(n_{i0} \frac{c_s \rho^* U_i}{B_0} \right) + \dots \\
& \left(\frac{2in_{i0}}{\psi' |\nabla \rho|} \left(k_y (\kappa_n + \Lambda \kappa_g) - k_x \frac{g^{\rho\rho} \psi'}{B_0 \rho_s} \kappa_g \right) \right) \left(\frac{T_{e0} \Phi}{e} + \frac{T_{e0} T_i + T_{i0} n_i}{e} \right) + \dots \\
& \partial_t \frac{k_{\perp}^2 m_i}{\tau e B_0^2} \left(n_{i0} \frac{\rho^* T_{e0} \Phi}{e} + \frac{n_{i0} T_{e0} \rho^* T_i + T_{i0} n_{i0} \rho^* n_i}{e} \right) = 0,
\end{aligned} \tag{5.36}$$

where $\Lambda = -\nabla \alpha \cdot \nabla \psi / B$. Simplifying each term and multiplying through by τ/n_{i0} gives the following equation:

$$\begin{aligned}
& \partial_t n_i + i \frac{k_y}{\rho^* \psi'} \frac{\omega_n}{c_s} \frac{T_{e0} \Phi}{e} + \frac{B_0}{c_s} \nabla_{\parallel} \left(\frac{c_s U_i}{B_0} \right) + \dots \\
& \partial_t \frac{k_{\perp}^2 m_i}{e B_0^2} \left(\frac{T_{e0} \Phi}{e} + \frac{T_{e0} T_i + T_{i0} n_i}{e} \right) + \dots \\
& i\tau \left(\frac{2}{\psi' |\nabla \rho| \rho^*} (k_y (\kappa_n + \Lambda \kappa_g) - k_x g^{\rho\rho} \kappa_g) \right) \left(\frac{T_{e0} \Phi}{e} + \frac{T_{e0} T_i + T_{i0} n_i}{e} \right) = 0.
\end{aligned} \tag{5.37}$$

Simplifying further and incorporating $D_k = 2k_x L_{eq} \Lambda_0 \kappa_g / |\nabla \rho| - 2k_y L_{eq} (\kappa_n + \Lambda \kappa_g) / |\nabla \rho|$, where $\Lambda_0 = g^{\rho\rho}$ and $B_k = (k_y^2 + (k_y \Lambda - k_x \Lambda_0)^2) / g^{\rho\rho}$ from the three-field model notation, where τ is now the temperature ratio T_e/T_i rather than the normalization for time:

$$\partial_t n_i + ik_y \omega_n \Phi - iD_k (\Phi + T_i + \tau n_i) + \partial_t (B_k (\Phi + T_i + \tau n_i)) + \nabla_{\parallel} U_i = 0. \tag{5.38}$$

Eq. (5.36) is the ω_n - and τ -corrected ion continuity equation. Next, the parallel ion momentum equation, Eq. (5.22):

$$B_0 n_{i0} e \partial_t \tilde{A}_{\parallel} + \partial_t m_i n_{i0} B_0 \tilde{v}_{\parallel i} + \frac{\partial p_{i0}}{\partial \rho} \frac{i k_{\alpha} \tilde{A}_{\parallel} B_0}{\psi'} + \nabla_{\parallel} (n_{i0} e \tilde{\phi} + \tilde{p}_i) = 0. \quad (5.39)$$

After substitution of the normalized quantities, we arrive at the following:

$$\begin{aligned} \frac{T_{e0}}{c_s \tau} n_{i0} \frac{\partial A_{\parallel}}{\partial t} + \frac{1}{\tau} m_i n_{i0} c_s \frac{\partial}{\partial t} U_i - \frac{p_{i0} \omega_{pi}}{L_{eq}} \frac{i k_{\alpha} T_{e0} A_{\parallel}}{c_s e \psi'} + \dots \\ \frac{n_{i0}}{L_{eq}} \nabla_{\parallel} (T_{e0} \Phi + T_{e0} T_i + T_{i0} n_i) = 0, \end{aligned} \quad (5.40)$$

which simplifies further to the following:

$$\frac{\partial A_{\parallel}}{\partial t} + \frac{\partial U_i}{\partial t} - \tau (\omega_{T_i} + \omega_n) i k_y A_{\parallel} + \nabla_{\parallel} (\Phi + T_i + \tau n_i) = 0. \quad (5.41)$$

This is the A_{\parallel} -, τ -, and finite- ω_n -corrected parallel ion momentum equation.

Next, the ion energy equation:

$$\begin{aligned} n_{i0} \frac{\partial \tilde{T}_i}{\partial t} - i n_{i0} \frac{k_{\alpha}}{\psi'} \frac{\partial T_{i0}}{\partial \rho} \tilde{\phi} + \frac{2}{3} i \omega T_{i0} \tilde{n}_i + \frac{2}{3} i T_{i0} \frac{k_{\alpha}}{\psi'} \frac{\partial n_{i0}}{\partial \rho} \tilde{\phi} + \dots \\ \frac{5}{3} \frac{i p_{i0}}{e} \left(\frac{2}{\psi' |\nabla \rho|} \left(k_{\alpha} (\kappa_n + \Lambda \kappa_g) - k_{\rho} \frac{g^{\rho\rho} \psi'}{B_0} \kappa_g \right) \right) \tilde{T}_i = 0, \end{aligned} \quad (5.42)$$

becomes the following after substitution of the normalized variables and simplification:

$$\partial_t \left(T_i - \frac{2}{3} \tau n_i \right) + i k_y \tau \left(\omega_{T_i} - \frac{2}{3} \omega_n \right) \Phi - \frac{5}{3} i \tau D_k T_i = 0. \quad (5.43)$$

Next the analogous equations for the electron species will be presented.

The electron continuity equation given below:

$$\begin{aligned} & \frac{n_{i0}\rho^*}{\tau_n} \partial_t \tilde{n}_i - i \frac{k_\alpha}{\psi'} \frac{\partial n_{i0}}{\partial \rho} \frac{T_{e0}\rho^*}{e} \Phi + \nabla_{\parallel} \left(n_{i0} \frac{c_s \rho^* U_e}{B_0} \right) + \dots \\ & + \left(\frac{2in_{i0}}{\psi' |\nabla \rho|} \left(k_\alpha (\kappa_n + \Lambda \kappa_g) - k_\rho \frac{g^{\rho\rho} \psi'}{B_0} \kappa_g \right) \right) \left(\frac{T_{e0}}{e} \Phi - \frac{T_{e0} T_e + T_{e0} n_i}{e} \right) = 0, \end{aligned} \quad (5.44)$$

will simplify to the following

$$\partial_t n_i + ik_y \omega_n \Phi - iD_k (\Phi - (T_e + n_i)) + \nabla_{\parallel} U_e = 0, \quad (5.45)$$

which is similar to the ion continuity equation, with the exceptions that the polarization term is missing and some signs have changed.

Next, the electron momentum equation:

$$-en_{i0} B_0 \partial_t \tilde{A}_{\parallel} - \nabla_{\parallel} (en_{i0} \tilde{\phi}) + T_{e0} \nabla_{\parallel} \tilde{n}_i + T_{e0} \frac{\partial n_{i0}}{\partial \rho} \frac{ik_\alpha \tilde{A}_{\parallel} B_0}{\psi'} = 0, \quad (5.46)$$

becomes the following, after substitutions and simplifications,

$$\partial_t A_{\parallel} + \nabla_{\parallel} (\Phi - n_i) + i\omega_n k_y A_{\parallel} = 0. \quad (5.47)$$

The Closure equation:

$$\nabla_{\parallel} \tilde{T}_e + \frac{\partial T_{e0}}{\partial \rho} \frac{ik_\alpha \tilde{A}_{\parallel} B_0}{\psi'} = 0. \quad (5.48)$$

becomes

$$\nabla_{\parallel} T_e - i\omega_{Te} k_y A_{\parallel} = 0. \quad (5.49)$$

Lastly, Ampère's law is the final equation that can be used to equate U_e with U_i :

$$\frac{1}{2}\beta_e(U_i - U_e) = B_k A_{\parallel}, \quad (5.50)$$

5.3.8 Summary of the five-field model

A summary of the six equations that comprise the five-field model are below:

Ion continuity:

$$\partial_t(n_i + B_k(\Phi + T_i + \tau n_i)) + ik_y\omega_n\Phi - iD_k(\Phi + T_i + \tau n_i) + \nabla_{\parallel}U_i = 0 \quad (5.51)$$

Ion parallel momentum:

$$\partial_t A_{\parallel} + \partial_t U_i - \tau(\omega_{T_i} + \omega_n)ik_y A_{\parallel} + \nabla_{\parallel}(\Phi + T_i + \tau n_i) = 0 \quad (5.52)$$

Ion energy:

$$\partial_t \left(T_i - \frac{2}{3}\tau n_i \right) + ik_y\tau \left(\omega_{T_i} - \frac{2}{3}\omega_n \right) \Phi - \frac{5i\tau}{3}D_k T_i = 0 \quad (5.53)$$

Electron continuity:

$$\partial_t n_i + ik_y\omega_n\Phi - iD_k(\Phi - (T_e + n_i)) + \nabla_{\parallel}U_e = 0 \quad (5.54)$$

Electron parallel momentum:

$$\partial_t A_{\parallel} + \nabla_{\parallel}(\Phi - n_i) + i\omega_n k_y A_{\parallel} = 0 \quad (5.55)$$

Closure equation:

$$\nabla_{\parallel}T_e - i\omega_{T_e}k_y A_{\parallel} = 0 \quad (5.56)$$

and finally Ampère's law closes the system, relating U_e to U_i :

$$\frac{1}{2}\beta_e(U_i - U_e) = B_k A_{\parallel}, \quad (5.57)$$

5.4 Evaluating the five-field model

One can write the five-field model as a generalized eigenvalue problem of the form $\underline{\underline{A}}\underline{x} = \lambda\underline{\underline{B}}\underline{x}$, where \underline{x} , λ , $\underline{\underline{A}}$, and $\underline{\underline{B}}$ are the eigenvector, the eigenvalue, a matrix corresponding to non-time-derivative terms of the system, and a matrix corresponding to time-derivative terms of the system, respectively. For example, if one substitutes Ampère's law and the closure equation into the five dynamical equations such that the system is comprised of five equations in five unknowns, then the $\underline{\underline{B}}$ matrix would be nearly diagonal, with the only non-diagonal contributions arising from the polarization term in the ion continuity equation and the $\partial_t n_i$ term in the ion energy equation. The $\underline{\underline{A}}$ operator is in general more complicated, as it has non-diagonal terms as well as spatial derivative operatives which are handled with finite differences in this work.

The initial benchmark for the five-field model is evaluating its solutions in the $\beta \rightarrow 0$ limit and comparing with three-field model results. Since the three-field model is electrostatic by construction, the three- and five-field models should coincide as β approaches zero. Figure 5.18 shows a comparison between the three-field model using Cyclone Base Case (CBC) parameters and the five-field model, also using CBC parameters, with $\beta \approx 0$. Note the general agreement between the two models. This agreement constitutes evidence that the equations which comprise the five-field model and the numerical method for solving the system are behaving as one would expect at small β .

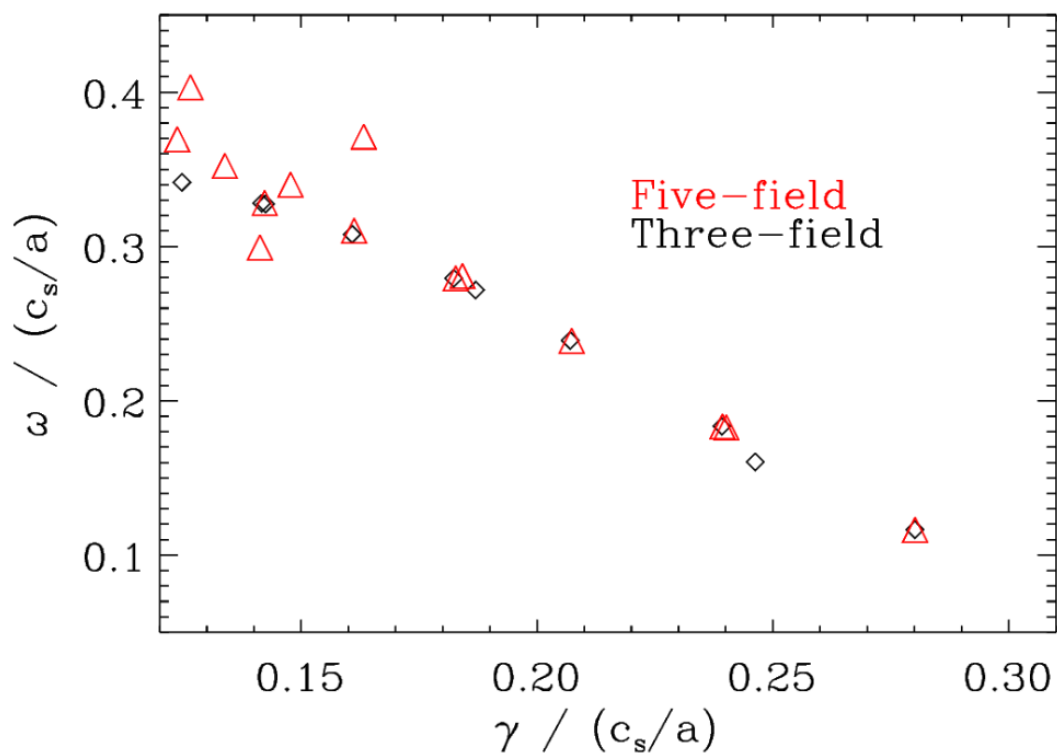


Figure 5.18: A comparison of subdominant modes corresponding to the ITG branch for CBC parameters. Three-field model modes are denoted by black diamonds while five-field model (with $\beta \rightarrow 0$) modes are denoted by red triangles. The two models coincide well, with some differences due to grid-scale modes, but, overall, this is evidence that the five-field model is behaving correctly when β is small.

5.5 Conclusions of this chapter

Gyrokinetic electromagnetic simulations of HSX, Heliotron-J, and a circular tokamak equilibrium have been presented, showing that kinetic ballooning modes can be excited at a critical $\beta_{\text{crit}}^{\text{KBM}}$ that is considerably smaller than the critical β for ideal MHD ballooning. This difference is associated with the relatively low average magnetic shear of these configurations. While one might expect this to bode poorly for the performance of low-average-shear magnetic equilibria, nonlinear simulations of HSX show that saturation is achievable with $\beta_{\text{crit}}^{\text{KBM}} < \beta < \beta_{\text{crit}}^{\text{MHD}}$ and that a significant reduction in transport is observed relative to the $\beta \approx 0$ case. However, saturation of simulations only occurs when the minimum binormal wavenumber k_y^{min} of the system is stable to KBMs. This is equivalent to saying that the largest binormal length scales of the flux tube domain must be stable to KBMs. One possible explanation of this result is that the nonlinear transfer of energy from the strongly driven KBMs in the binormal wavenumber range $0.1 < k_y \rho_s < 0.2$ to stable modes with $k_y \rho_s < 0.1$ is possible and allows for saturation when the condition that k_y^{min} is stable to KBMs is met.

The KBM subdominant mode spectrum of HSX exhibits two families of unstable KBMs. With low \hat{s} , KBMs are more extended along the field line, allowing KBMs to access free energy in the gradients via the bad curvature regions away from the outboard midplane of a given field line. As a consequence, KBMs can peak at finite ballooning angle, and even tearing-parity

KBMs (TKBMs in the nomenclature of Ref. [18]) are found. After conducting a scan over \hat{s} , for both positive and negative values, $\beta_{\text{crit}}^{\text{KBM}}$ increases monotonically, regardless of the sign of the average magnetic shear. This is consistent with the fact that stronger magnetic shear tends to stabilize drift waves.

A number of nonlinear analyses have also been conducted here which elucidate the importance of KBMs in the nonlinear dynamics. Heat flux spectra shown in Fig. 5.11 highlight that KBM transport dominates the dynamics when KBMs are destabilized linearly, even if KBM growth rates are subdominant to ITG growth rates. A comparison of dominant linear KBM and nonlinear frequencies shows good agreement in the KBM-dominated k_y -range. This constitutes evidence that KBMs are significantly contributing to the nonlinear state. Additionally, an analysis of nonlinear energy transfer shows that KBMs, or at the very least the KBM-dominated k_y -range, play an integral role in the energy transfer dynamics, even more so than zonal modes, further highlighting the fact that the nonlinear state indeed shows signs of both ITG and KBM drive. An investigation of how the electrostatic ion heat flux changes as a function of β shows a decrease in heat flux as β increases until β is sufficiently close to $\beta_{\text{crit}}^{\text{KBM}}(k_y^{\text{min}})$, showing both the improved nonlinear behavior relative to linear $\beta_{\text{crit}}^{\text{KBM}}$ predictions and the steep increase in fluxes at large values of $\beta > \beta_{\text{crit}}^{\text{KBM}}$.

The linear characteristics of the low-average-magnetic-shear equilibria presented in this work raise questions regarding the utility of such configurations

at the β values required for an efficient fusion reactor concept. However, as the nonlinear calculations presented here show, nonlinear dynamics can overcome poor linear KBM properties such as the increase in total heat flux generally associated with $\beta > \beta_{\text{crit}}^{\text{KBM}}$, and nonlinear fluxes in HSX even decrease as β increases above $\beta_{\text{crit}}^{\text{KBM}}(k_y = 0.1)$, as shown in Fig. 5.17, until $\beta \approx 0.6\%$ [20]. It is important to keep such KBM saturation physics in mind during efforts to optimize stellarator equilibria at reactor-relevant $\beta \geq 5\%$ values. Lastly, the fact that in the present simulations, achieving saturation depends critically on $\beta_{\text{crit}}^{\text{KBM}}(k_y^{\text{min}})$, it is possible that the value of $\rho^* = \rho_s/a$ – and thus the KBM threshold at $n = 1$ – of a low-magnetic-shear confinement device may affect the achievable plasma β . However, future investigation will need to determine whether this effect survives in more realistic simulation frameworks, in particular when retaining global profile effects.

Lastly, a derivation of the five-field model is shown in this chapter, highlighting both differences and similarities with the electrostatic three-field model. The five-field model consists of the ion continuity, ion parallel momentum, ion energy, electron continuity, electron parallel momentum, Ampère’s law, and a closure equation describing infinite electron thermal conduction parallel to the magnetic field line. After a number of pages of algebra, normalized forms of these equations are shown in Eqs. (5.51)–(5.57). A description of the numerical scheme used to solve the set of seven equations in seven unknowns is also given before a comparison between the three-field and five-field models in the

limit of $\beta \rightarrow 0$, where the two models should coincide. This comparison does show agreement between the two models, providing confidence in the five-field model and the numerical solution method.

Citations

- [1] Hegna, C.C., Terry, P.W., & Faber, B.J. 2018 Theory of ITG turbulent saturation in stellarators: identifying mechanisms to reduce turbulent transport. *Phys. Fluids* **18** (5), 552-565.

- [2] Kotschenreuther, M. 1986 Compressibility effects on ideal and kinetic ballooning modes and elimination of finite Larmor radius stabilization. *Phys. Fluids* **29** (9), 2898-2913.

- [3] Connor, J.W., Hastie, R.J., & Taylor, J.B. 1978 Shear, periodicity, and plasma ballooning modes. *Phys. Rev. Lett.* **40**, 396-399.

- [4] Tang, W.M. 1978 Microinstability theory in tokamaks. *Nucl. Fusion* **18** (8), 1089-1160.

- [5] Strauss, H.R. 1979 Finite beta trapped electron fluid mode. *Phys. Fluids* **22**, 1079-1081.

- [6] Antonsen, T.M. Jr, Drake, J.F., Guzdar, P.N., Hassam, A.B., Lau, Y.T., Liu, C.S., & Novakovskii, S.V. 1996 Physical mechanism of enhanced stability from negative shear in tokamaks: implications for edge transport and the L-H transition. *Phys. Plasmas* **3** (6), 2221-2223.
- [7] Tang, W.M., Connor, J.W., & Hastie, R.J. 1980 Kinetic-ballooning-mode theory in general geometry. *Nucl. Fusion* **20**, 1439.
- [8] Dominguez, R.R. & Waltz, R.E. Ion temperature gradient mode in the weak density gradient limit. *Phys. Fluids* **31** (10), 3147-3150.
- [9] Jhowry, B. & Anderson, J. 2003 On the stabilization of ion temperature gradient modes by finite beta in noncircular toroidal devices. *Phys. Plasmas* **10** (3), 782-789.
- [10] Whelan, G.G., Pueschel, M.J., Terry, P.W., Citrin, J., McKinney, I.J., Guttenfelder, W., & Doerk, H. 2019 Saturation and nonlinear electromagnetic stabilization of ITG turbulence. *Phys. Plasmas* **26** (8), 082302.
- [11] Pueschel, M.J., Kammerer, M., & Jenko, F. 2008 Gyrokinetic turbulence simulations at high plasma beta. *Phys. Plasmas* **15**, 102310.

- [12] Tang, W.M., Rewoldt, G., Cheng, C.Z., & Chance, M.S. 1985 Kinetic analysis of MHD ballooning modes in tokamaks. *Nucl. Fusion* **25** (2), 151.
- [13] Aleynikova, K. & Zocco, A. 2017 Qualitative study of kinetic ballooning mode theory in simple geometry. *Phys. Plasmas* **24**, 092106.
- [14] See <https://github.com/tylerbcote/pyballoon> for details.
- [15] Plunk, G.G., Helander, P., Xanthopoulos, P., & Connor, J.W. 2014 Collisionless microinstabilities in stellarators. III. The ion-temperature-gradient mode. *Phys. Plasmas* **21** (3), 032112.
- [16] Ishizawa, A., Kishimoto, Y., Watanabe, T.-H., Sugama, H., Tanaka, K., Satake, S., Kobayashi, S., Nagasaki, K., & Nakamura, Y. 2017 Multi-machine analysis of turbulent transport in helical systems via gyrokinetic simulation. *Nucl. Fusion* **57** (6), 066010.
- [17] Pueschel, M.J. & Jenko, F. 2010 Transport properties of finite- β microturbulence. *Phys. Plasmas* **17**, 062307.
- [18] Pueschel, M.J., Hatch, D.R., Ernst, D.R., Guttenfelder, W., Terry, P.W., Citrin, J., & Connor, J.W. 2019 On microinstabilities and turbulence in

steep-gradient regions of fusion devices. *Plasma Phys. Control. Fusion* **61** (3), 034002.

[19] Hirose, A. & Elia, M. 1996 Kinetic Ballooning Mode with Negative Shear. *Phys. Rev. Lett.* **76** (4), 628.

[20] McKinney, I.J., Pueschel, M.J., Faber, B.J., Hegna, C.C., Ishizawa, A., & Terry, P.W. 2021 Kinetic-ballooning-mode turbulence in low-average-magnetic-shear equilibria. *J. Plasma Phys.* **87**, 905870311.

Chapter 6

Conclusions, summary, and future research

The conclusions presented here constitute important advancements in the fields of electrostatic and electromagnetice turbulence in quasi-symmetric stellarators. First, the ITG results shown in Ch. 4 represent the first comparison of ITG growth rates and nonlinear heat fluxes between two quasi-symmetric configurations which definitively shows that linear physics alone is not always a sufficient predictor for turbulent transport, a result that has important implications for the field of quasi-symmetric stellarator optimization. Second, the KBM results presented in Ch. 5, specifically both the achievement of nonlinear saturation of ITG-KBM turbulence in simulations of HSX for $\beta > \beta_{\text{crit}}^{\text{KBM}}$ and the role of small (large) \hat{s} (ω_{Ti}) in setting a low $\beta_{\text{crit}}^{\text{KBM}}$ in HSX, are completely novel and have important implications for simulations of other small- \hat{s} 3D equilibria like W7-X and Heliotron-J where there have been obstacles to achieving nonlinear saturation of KBM turbulence numerically. Lastly, a novel electromagnetic fluid model is introduced and benchmarked. After developing the appropriate turbulence metrics from the five-field model, this model

will be used to both understand KBM turbulence saturation in low- \hat{s} configurations and optimize quasi-symmetric stellarators with respect to finite- β turbulent transport. The following subsections summarize the primary results from each chapter before giving a number of avenues for how this research could continue.

6.1 Summary

6.1.1 Novel comparison of ITG turbulence between two quasi-symmetric stellarators

A number of results related to both the linear and nonlinear ITG properties of the HSX and NCSX quasi-symmetric stellarator geometries are presented. Electrostatic GENE flux-tube simulations of ITG modes in NCSX and HSX form the basis of a comparison of linear and nonlinear behavior between the two configurations. The main novel conclusion of the comparison is that dominant growth rates are lower in NCSX while nonlinear heat fluxes are lower in HSX, a result with important ramifications for stellarator optimization. This finding suggests that there are quantitative differences in the ITG saturation mechanism between HSX and NCSX, a motivation for further study of the subject. Additional analyses elucidate differences in the ITG saturation physics between HSX and NCSX. The characteristic extended eigenmode structures in HSX are qualitatively different than the peaked, localized eigenmodes present in NCSX. This difference in eigenmode structure between HSX and NCSX,

slab-like in HSX and toroidal-like in NCSX, allows for the more efficient nonlinear transfer of energy to stable modes at comparable wavenumber in HSX relative to NCSX (Hegna et al., 2018), and this begins to explain the lower flux levels in simulations of HSX. The linear eigenmode landscape of HSX exhibits an order of magnitude more subdominant modes than NCSX, depending on the value of k_y . Since there are more unstable modes in HSX, the turbulence will be comprised of many more concurrently-excited modes relative to NCSX. Additionally, a quasilinear calculation, which accounts for the subdominant modes, definitively shows that the relationship between dominant growth rates and nonlinear heat flux between HSX and NCSX mentioned above is not changed when subdominant modes are included. This is an indication that the difference in heat flux between the two configurations is a result of some aspect of the nonlinear physics, and not merely an artifact of the subdominant linear eigenmodes, a conclusion that is consistent with the narrative of more efficient nonlinear energy transfer to stable modes in HSX. A nonlinear frequency analysis concludes that the turbulent state in HSX consists of many more concurrently-excited modes than that in NCSX. This fact could also be an indication that more stable modes are excited in HSX as well, but additional analyses must be done to address this hypothesis. An analysis of the cross-phase between electrostatic potential Φ and ion temperature fluctuations T_i highlights that both configurations exhibit similar nonlinear cross-phases, but there is a bigger difference between dominant linear and nonlinear phases

in HSX relative to NCSX. This is consistent with the fact that HSX performs worse linearly relative to NCSX, but can overcome that via more favorable nonlinear saturation physics. Overall, the disparate magnetic shear between HSX and NCSX plays an important role in determining whether slab-like or toroidal-like ITG is dominant, which has important consequences for nonlinear saturation within the context of coupling between eigenmodes and therefore also for saturated heat flux levels.

6.1.2 Novel ITG-KBM turbulence results in the quasi-helically symmetric stellarator HSX

A number of important results pertaining to KBM turbulence in HSX, Heliotron-J, and a small- \hat{s} tokamak, three low-magnetic-shear equilibria, are discussed in this dissertation. Results pertaining to the critical β at which KBM becomes dominant and the implications therein are presented. In HSX, Heliotron-J, and the small- \hat{s} tokamak, the critical β at which KBM becomes the dominant instability is very small ($\beta_{\text{crit}}^{\text{KBM}} \approx 0.2\%$ at $k_y \rho_s \approx 0.1$). This aspect of the linear KBM dynamics is a strong function of the average magnetic shear in HSX, as $\beta_{\text{crit}}^{\text{KBM}}$ increases greatly as $|\hat{s}|$ increases, regardless of sign. The small magnetic shear in HSX permits the KBM eigenmode to be more extended along the field line, rather than be localized to the outboard mid-plane. This very small $\beta_{\text{crit}}^{\text{KBM}}$ in HSX, Heliotron-J, and the small- \hat{s} tokamak is also particularly sensitive to the ion temperature gradient, as $\beta_{\text{crit}}^{\text{KBM}} \approx 0.8\%$ at $k_y \rho_s \approx 0.1$, much closer to the MHD ideal ballooning limit for HSX at

$\beta \approx 1.1\%$, when the sum of the gradients is held constant and there is no ion temperature gradient. An eigenvalue calculation is also carried out for HSX which points to the destabilization of two branches of KBMs rather than a single mode like would be the case in a high- \hat{s} tokamak. In addition to linear analyses, electromagnetic nonlinear simulations are also presented, where it is shown that HSX exhibits sizable (factor of 4) reduction in heat flux going from $\beta = 0.05\%$ to 0.48% . Importantly, even with the less-than-favorable linear KBM properties in HSX, it is still possible to achieve nonlinear saturation at reasonable values of normalized plasma pressure ($\beta \approx 0.5\% > \beta_{\text{crit}}^{\text{KBM}}$), so long as the minimum k_y of the simulation is linearly stable to KBMs. This is an indication that some aspect of the ITG mode saturation at low k_y aids in KBM saturation at slightly smaller scales, and without this ITG mechanism, the KBM turbulence does not saturate. The second half of Ch. 5 focuses on the derivation and benchmarking of a five-field fluid model which extends a three-field ITG model to include finite- β effects. The model consists of a continuity and parallel momentum equation for both ion and electrons, an ion energy equation, Ampère's Law, and a closure equation representing infinite parallel electron thermal conduction. This model will be used to develop both a physical understanding of KBM saturation and turbulence proxies that can be used in stellarator optimization schemes.

6.2 Future work

Here is a list of items that constitute potential future research paths for this work:

6.2.1 Research items

1. Continued five-field model development

In its current state, the five-field model has been numerically implemented and benchmarked against the three-field model, giving confidence that it is correct in formulation. Once additional benchmarking endeavors such as extensive quantitative comparison with gyrokinetics have been completed, development of the nonlinear aspects of the five-field model can begin. The five-field model will retain two nonlinearities: $\mathbf{E} \times \mathbf{B}$ advection and magnetic flutter (\tilde{v}_i and \tilde{A}_{\parallel}), as these are expected to be the dominant nonlinearities. Once the linear and nonlinear aspects of the model are complete, the next step will be to derive quantities analogous to the triplet correlation time and coupling coefficients between eigenmodes (Hegna et al., 2018).

2. GENE simulations of KBM turbulence

Both linear and nonlinear simulations of KBMs in low-magnetic-shear equilibria will be necessary for comparison against predictions of the fluid model. Additional investigation of KBMs even outside of the context of

the five-field model will be vital for the research project too. GENE simulations where certain terms, e.g. the electromagnetic nonlinearity, are omitted might yield insight into the saturation mechanism of ITG-KBM turbulence. Lastly, simulations of other low-magnetic-shear equilibria generated from optimization routines will be necessary.

3. Optimized stellarator equilibria

Once the fluid model development is finished and quantities such as triplet correlation time and coupling coefficients both have been numerically implemented and successfully interface with STELLOPT or ROSE (or any other optimization code), the next step will be to generate low-magnetic-shear quasi-symmetric stellarator equilibria that exhibit improved KBM behavior and reduced heat flux, as verified by nonlinear GENE simulations.

ProQuest Number: 28868526

INFORMATION TO ALL USERS

The quality and completeness of this reproduction is dependent on the quality and completeness of the copy made available to ProQuest.



Distributed by ProQuest LLC (2021).

Copyright of the Dissertation is held by the Author unless otherwise noted.

This work may be used in accordance with the terms of the Creative Commons license or other rights statement, as indicated in the copyright statement or in the metadata associated with this work. Unless otherwise specified in the copyright statement or the metadata, all rights are reserved by the copyright holder.

This work is protected against unauthorized copying under Title 17, United States Code and other applicable copyright laws.

Microform Edition where available © ProQuest LLC. No reproduction or digitization of the Microform Edition is authorized without permission of ProQuest LLC.

ProQuest LLC
789 East Eisenhower Parkway
P.O. Box 1346
Ann Arbor, MI 48106 - 1346 USA